Tectonics of the Greater Caucasus and the Arabia-Eurasia orogen

by

Boris Avdeev

A dissertation submitted in partial fulfillment
of the requirements for the degree of
Doctor of Philosophy
(Geological Scienses)
in The University of Michigan
2011

Doctoral Committee:

Assistant Professor Nathan A. Niemi, Chair
Professor Rob Van Der Voo
Associate Professor Aline J. Cotel
Associate Professor Jeroen Ritsema
Assistant Professor Eric A. Hetland

ACKNOWLEDGEMENTS

I would like to thank fellow graduate students for making my time at the University of Michigan enjoyable. The SCALE lab and its members, including Alison Duvall, Alex Lechler, and Marin Clark, provided a great collaborative environment. I acknowledge Todd Ehlers, once a part of my dissertation committee, for his feedback on my dissertation research. Rob Van Der Voo, Aline Cotel, Jeroen Ritsema and Eric Hetland are thanked for serving on my dissertation committee to the very end. Finally, I would like to thank Nathan Niemi for his invaluable advise, valuable support, and his great attitude.

TABLE OF CONTENTS

LIST OF FIGURES

Figure

LIST OF TABLES

Table

LIST OF APPENDICES

Appendix

CHAPTER I

Introduction

The Periarabian orogen is the central part of the Alpine-Himalayan belt—an impressive suture left after the closure of the Mesozoic Tethys ocean. Stretching from western Turkey to eastern Iran, it is formed by the convergence of the Arabian and Eurasian plates. Presently, most of the orogen, with the exception of the Black Sea and South Caspian basins, is above sea level and is bounded by continental plates. As such, it is a continental orogen. According to various estimates, Periarabia became a continental orogen sometime between 5 and 50 Ma and thus, it is likely the youngest continental orogen on Earth.

Because it is at an early stage of development, the Periarabian orogen is undergoing, or perhaps still preserves, processes that could be common to all nascent orogens, of which understanding is critical for a complete understanding of continental collision. For example, hypothesized processes such as oceanic slab break-off (van Hunen and Allen, 2010) and drop of an overthickened and eclogitized lithospheric root (Ershov et al., 2003) have been postulated for Periarabia, making it yet another locality for capturing such events and studying their effects on magmatism, deformation, and topographic evolution.

The topographic evolution of the Periarabian orogen alone has important impli-

cations for a number of other studies. The timing and patterns of emergence of mountain ranges between Arabia and Eurasia defined pathways of Cenozoic mammalian evolution (Briggs, 1974), as well as possibly affected patterns of atmospheric circulation. Closure of the passage between the Indian and Atlantic oceans have changed global ocean circulation and has been speculated to significantly affect climate, possibly leading to recent global cooling (Allen and Armstrong, 2008).

Despite its uniqueness and importance, and probably as a result of its modesty in scale and difficulty of access, Periarabia is relatively understudied compared to other parts of the Alpine-Himalayan belt. As of April, 2011, Google Scholar search for geology (Caucasus OR Zagros OR Alborz) returns 19,000 articles, while geology Himalaya returns 37,700, and geology Alps returns 87,800 items. This dissertation contributes to the growing pool of research on the geology of Periarabia.

There are a number of outstanding questions about Periarabia. Foremost is the timing of collision between Arabia and Eurasia. To the date, there is no agreed upon age of the collision, with estimates spanning most of the Cenozoic era. And there is no indication that these estimates are converging with time to a value other than the arithmetic mean of 32.75 Ma. Chapters 2 and 3 present new thermochronometric and sedimentologic data from the Greater Caucasus that suggest that the last deep marine basin separating Arabia from Eurasia could have disappeared as late as the end of the Miocene. The concluding chapter discusses why late Miocene is not the new estimate of the collision age, and why the collision age is unlikely to be resolved, or is a useful number for the Periarabian orogen.

The uncertainty of the collision age holds back (or adds freedom to) measuring amounts of crustal shortening, thickening, and underplating, as well as complicates (or simplifies) interpretation of driving forces of various tectonic events, among which

stands out the orogen-wide temporal cluster of rapid exhumation and fault initiation events centered about 5 Ma. This reorganization requires a driver, and a common presumption that the collision occurred prior to 5 Ma lead many to search for explanations in the realm of post-collisional tectonics, such as overthickening-driven propagation of deformation (Allen et al., 2004), mantle supported uplift (Copley and Jackson, 2006), mantle upwelling following the Tethyan slab break-off (van Hunen and Allen, 2010), or delamination of a lithospheric root (Ershov et al., 2003). Results of the chapters 2 and 3 imply that the closure of the Greater Caucasus basin coincided with the reorganization and is a plausible driving force for it.

Although the following work impacts the geology of the whole Periarabian orogen, it is focused on the Greater Caucasus, a mountain range located on the northern fringe of the orogen along the edge of Eurasia, and on the opposite side from the Neotethyan suture that is located along Arabia. Neotethyan subduction presumably fueled Arabia-Eurasia convergence (McQuarrie et al., 2003), yet, the Greater Caucasus are the highest mountains within the orogen and, in the eastern part, currently accommodate about half of the total plate convergence. Once again, resolution of this anomaly is precluded by lack of basic knowledge about this range. Similar to the uncertainty of the timing of Arabian collision, the age of the Greater Caucasus mountains is debated. The new thermochronometric data presented in chapters 2 and 3 constrains the timing of uplift of the western and eastern Greater Caucasus. Finding that their uplift significantly post-dates the closure of Neotethys and is instead related to the closure of the Greater Caucasus back-arc basin provided the necessary near-field driving force that could produce the high mountains.

Thermochronometric results suggest that the initiation of the rapid exhumation occurred simultaneously along the length of the Greater Caucasus. Unlike the timing

of uplift, tectonics of the eastern and western Greater Caucasus are quite different. GPS and seismic observations suggest that the western Greater Caucasus are nearly inactive, while around 10 mm/y of geodetic shortening, accompanied by frequent earthquakes, is accommodated across the eastern Greater Caucasus. Geologic observations, however, provide evidence for a greater amount of total exhumation in the western Greater Caucasus. Chapter 4 presents a thermochronometrically constrained kinematic model for the western Greater Caucasus. Model estimates imply that the current low convergence rate is sufficient to produce the observed high amount of exhumation. This is possible because deformation in the western Greater Caucasus occurs mainly on a single fault. In contrast, deformation in the eastern Greater Caucasus is distributed through the width of the whole orogen, resulting in smaller uplift, but greater total shortening.

Tectonics strongly influences topography and, as a result, erosion. This permits the use of thermochronometry to study recent tectonic events. In fact, this dissertation is predominantly based on thermochronometric data. Chapter 5 provides a development in detrital thermochronometric methodology with a new approach to estimating erosion models characterizing short-term spatial patterns and long-term histories of denudation. This approach allows thermochronometric studies of terrains inaccessible for bedrock sampling and becomes useful in the Greater Caucasus, where the axis of the range coincides with three different international borders.

Bibliography

Allen, M., Jackson, J. and Walker, R. Late Cenozoic reorganization of the Arabia-Eurasia collision and the comparison of short-term and long-term deformation rates. *Tectonics*, 23(2):TC2008, 2004. doi:10.1029/2003TC001530.

Allen, M. B. and Armstrong, H. A. Arabia-Eurasia collision and the forcing of mid-Cenozoic global cooling. *Palaeogeogr. Palaeoclimatol. Palaeoecol.*, 265(1–2):52–58, 2008. doi:10.1016/j.palaeo.2008.04.021.

Briggs, J. C. Operation of zoogeographic barriers. *Systematic Zoology*, 23(2):248–256, 1974.

Copley, A. and Jackson, J. Active tectonics of the Turkish-Iranian plateau. *Tectonics*, 25(6):1–19, 2006.

Ershov, A. V., Brunet, M.-F., Nikishin, A. M., Bolotov, S. N., Nazarevich, B. P. and Korotaev, M. V. Northern Caucasus basin: thermal history and synthesis of subsidence models. *Sediment. Geol.*, 156(1-4):95–118, 2003.

McQuarrie, N., Stock, J. M., Verdel, C. and Wernicke, B. P. Cenozoic evolution of Neotethys and implications for the causes of plate motions. *Geophys. Res. Lett.*, 30(20):2036, 2003. doi:10.1029/2003GL017992.

van Hunen, J. and Allen, M. B. Continental collision and slab break-off: A comparison of 3-D numerical models with observations. *Earth Planet. Sci. Lett.*, 302:27–37, 2010.

CHAPTER II

Rapid Pliocene exhumation of the central Greater Caucasus constrained by low-temperature thermochronometry

2.1 Abstract

Constraining the timing of onset and rates of deformation within the Greater Caucasus mountains is key to understanding their role in accommodating deformation across the Arabia-Eurasia orogen. We present new low-temperature thermochronometric constraints on the Cenozoic thermal evolution of the central Greater Caucasus that elucidate a three phase cooling history. Between 50 and 30 Ma, cooling within the range was negligible. In Oligocene time, cooling rates throughout the range increased to ~ 4°C/My. These rates remained constant until the early Pliocene time, when they increased again, reaching ~ 25°C/My along the axial part of the range. Rates and timing of Oligocene exhumation are consistent with previous results from the western Greater Caucasus, and are proposed to result from onset of subduction of the Greater Caucasus back arc basin. Rapid exhumation of the Greater Caucasus, beginning in Pliocene time, contrasts with previously reported thermal histories for other portions of the range. Pliocene exhumation of the central Greater Caucasus appears to be tectonically driven, and coincides with widespread evidence for a major

Citation:
Avdeev, B., and N. A. Niemi (2011), Rapid Pliocene exhumation of the central Greater Caucasus constrained by low-temperature thermochronometry, *Tectonics, 30*, TC2009, doi:10.1029/2010TC002808

reorganization of the Arabia-Eurasia plate boundary. We hypothesize that this exhumation, and regionally observed plate reorganization, results from the collision of the Lesser Caucasus with Eurasia, completing the subduction of oceanic lithosphere across this segment of the Arabia-Eurasia plate boundary.

2.2 Introduction

Deformation associated with the Arabia-Eurasia collision zone covers much of southwestern Eurasia (Fig. 4.1), and spans nearly all of Cenozoic time (e.g. Nikishin et al., 2001). Despite a wealth of stratigraphic, erosional, and structural constraints on the timing of local deformation throughout the orogen, there is no clear consensus on how this localized deformation relates to the onset of Arabia-Eurasia continental collision, with estimates as diverse as Late Cretaceous (Stocklin, 1974; Alavi, 1994), Eocene (Hempton, 1987; Jassim and Goff, 2006; Allen and Armstrong, 2008), Oligocene–early Miocene (Yilmaz, 1993; Vincent et al., 2007; Robertson, 2000; Fakhari et al., 2008), middle Miocene (Dewey et al., 1986; Şengör and Kidd, 1979; McQuarrie et al., 2003), and late Miocene–early Pliocene (Zonenshain and Le Pichon, 1986; Philip et al., 1989; Khain, 1994) having been proposed. In part, this uncertainty results from the spatial and temporal complexities in the evolution of the collision zone. The Arabia-Eurasia collision is not comprised of a single suture, but is a mosaic of island arcs and microcontinents whose assembly along the complex paleogeographic margin of Neotethys (e.g. Golonka, 2004) is marked by numerous collisional events. Furthermore, final continent-continent collision is still incomplete along the Caspian segment of the collision zone, where oceanic, or thinned continental, crust of the south Caspian Basin continues to subduct northward under the northern Caspian Sea (Jackson et al., 2002).

Reorganization of the Arabia-Eurasia plate boundary at ∼5 Ma is both more widely accepted and more accurately temporally constrained than estimates of the onset of Arabia-Eurasia collision (Wells, 1969; Westaway, 1994; Axen et al., 2001; Allen et al., 2004; Copley and Jackson, 2006). Evidence for plate boundary reorganization includes rapid exhumation of the Alborz (Axen et al., 2001), comparison of fault slip rates with total offsets, which suggests Pliocene initiation of many active faults (Allen et al., 2004; Copley and Jackson, 2006), initiation of the North and East Anatolian faults (Şengör and Kidd, 1979; Arpat and Şaroğlu, 1972), and rapid subsidence in the South Caspian basin (e.g. Allen et al., 2002). The driving forces of this plate reorganization, however, remain controversial. Based on the assumption of a late Eocene Arabia-Eurasia collision, Wells (1969) proposed that the opening of the Red Sea could be such a driving force. Alternatively, Allen et al. (2004) argued for the gravitationally-driven shifting of deformation away from overthickened Turkish-Iranian plateau and Greater Caucasus crust into topographically lower foreland areas. Copley and Jackson (2006), based on new data on the crustal thickness of the Turkish-Iranian plateau, argued for mantle driven dynamic uplift of the plateau, rather than crustal thickening, and a resulting shift in deformation loci. On the other hand, if the onset of continent-continent collision is late Miocene (e.g. Zonenshain and Le Pichon, 1986), no other forcing beyond the collision itself is needed to drive this plate reorganization.

The complex nature of continental assembly and collision along the Arabia-Eurasia margin, the evidence for recent plate boundary reorganization, and the presence of ongoing subduction within the collision zone makes the Arabia-Eurasia orogenic system a natural laboratory for study of the early stages of continental collision that could provide insight into the evolution of more mature orogens and a better under-

standing of the spatial and temporal patterns of lithospheric deformation during the process of continental collision. Within this natural laboratory, the Greater Caucasus are particularly well situated to address these problems. The Greater Caucasus are the northern-most tectonic element of the Arabia-Eurasia collision zone (Fig. 4.1) and the highest mountain range in Europe. The Greater Caucasus are a locus of ongoing continental shortening (Reilinger et al., 2006), but lie adjacent to the Caspian zone of intra-orogenic subduction (Jackson et al., 2002). Despite their topographic prominence in the Arabia-Eurasia orogenic system, the role of the Greater Caucasus in accommodating strain throughout the evolution of the orogen is poorly understood. This stems from controversies surrounding both the timing of closure of Neotethys and the beginning of continental collision along the Arabian-Eurasian margin, as well as uncertainty regarding the onset of uplift and exhumation of the Greater Caucasus themselves.

Eocene to Oligocene deformation in the Greater Caucasus is documented by olistostromes and a regional angular unconformity at the base of the Oligocene–early Miocene Maikop formation (Milanovsky and Khain, 1963; Robinson et al., 1996; Banks et al., 1997; Kopp, 2007; Leonov, 2007; Vincent et al., 2007) that has been interpreted as a far-field response to the initiation of continental collision (Vincent et al., 2007; Allen and Armstrong, 2008). Whether or not this deformation led to significant crustal thickening and exhumation in the Paleogene, however, remains unclear (e.g. Cloetingh et al., 2007). Other authors (e.g. Zonenshain and Le Pichon, 1986; Philip et al., 1989; Khain, 1994; Ershov et al., 2003; Morton et al., 2003) have suggested late Miocene onset of deformation and uplift. Their conclusions are supported by the wide-spread occurrence of late Miocene conglomerates, the influx of Greater Caucasus derived clastics into surrounding sedimentary basins and the rapid

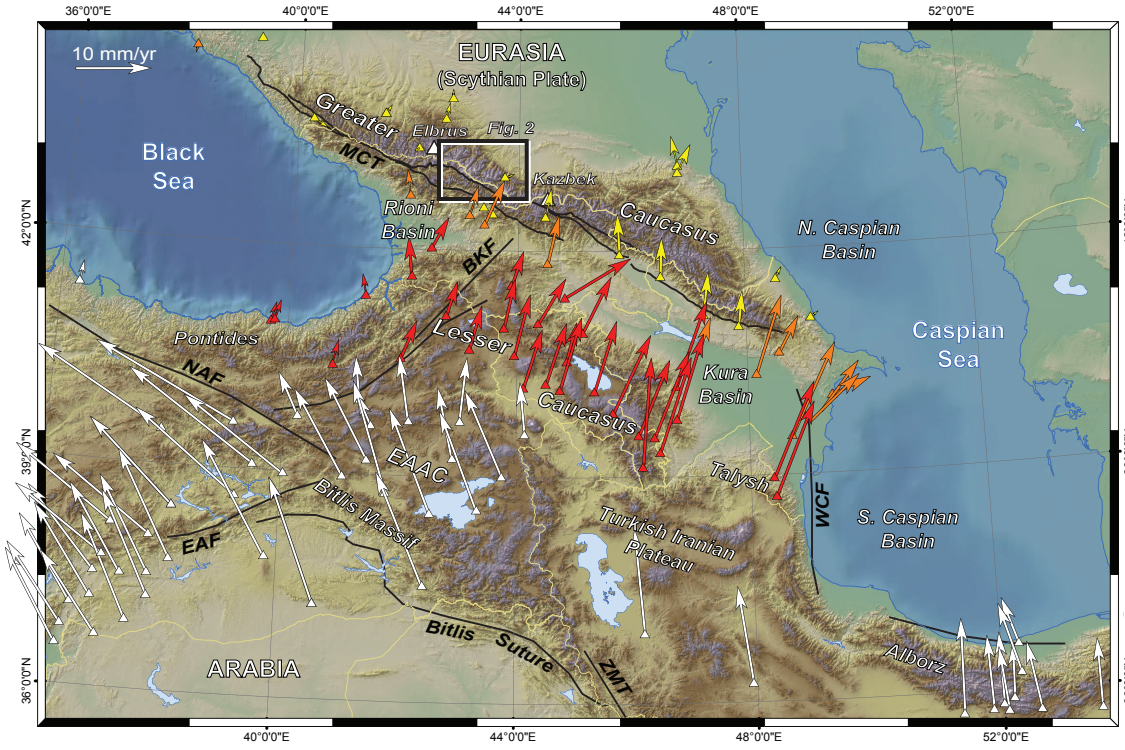

Figure 2.1: Shaded relief DEM of the Arabia-Eurasia orogen with the major tectonic elements labeled. **NAF**–North Anatolian Fault; **EAF**—East Anatolian Fault; **EAAC**—East Anatolian Accretionary Complex; **BKF**—Borjomi-Kazbek Fault; **MCT**—Main Caucasus Thrust; **ZMT**—Zagros Main Thrust; **WCF**—West Caspian Fault. Vectors show GPS velocities relative to Eurasia (Reilinger et al. (2006); Kadirov et al. (2008)) color-coded by region (yellow–Greater Caucasus; orange–Rioni and Kura basins; red–Lesser Caucasus; white–other regions). Box between Mt. Elbrus and Mt. Kazbek shows the area depicted in Fig. 2.2.

subsidence of the northern Caucasus basin.

Links between deformation within the Greater Caucasus and Pliocene plate reorganization are equally poorly constrained. Based on evidence of late Eocene deformation in the Greater Caucasus, Allen et al. (2004) suggested that increased gravitational potential across the range, resulting from shortening and crustal thickening, was a driving force of plate boundary reorganization in Miocene–Pliocene time. On the other hand, estimates of late Miocene or Pliocene exhumation and uplift of the Greater Caucasus (Zonenshain and Le Pichon, 1986; Khain, 1994) would suggest that the evolution of the Greater Caucasus is a response to plate boundary reorganization and not a driving force of the reorganization. Improved constraints on the timing of crustal deformation within the range are one approach to distinguish between these scenarios, and to better understand the role of the Greater Caucasus in accommodating strain throughout the evolution of the Arabia-Eurasia plate boundary.

Low-temperature thermochronometry provides a tool to constrain the timing and rates of exhumation in compressional orogens (e.g. Reiners et al., 2003; Blythe et al., 2007; Clark and Bilham, 2008). To the extent that the surface processes responsible for exhumation in compressional orogens are coupled to tectonic forcing (e.g. Whipple and Tucker, 1999), low-temperature thermochronometers provide a constraint on the timing and rate at which surface topography develops (e.g. Braun, 2005). Such data have elucidated the timing of crustal exhumation and its relationship to the regional tectonic evolution of northern Iran (e.g. Axen et al., 2001; Guest et al., 2006), but have seen little application to the remainder of the Arabia-Eurasia collision zone (e.g. Boztŭg and Jonckheere, 2007; Okay et al., 2010). To our knowledge, only two regional low-temperature thermochronometry studies of the Greater Caucasus

have been completed. One, using apatite fission-track methods (Kral and Gurbanov, 1996), yielded a variety of cooling ages from the central portion of the Greater Caucasus, ranging from Paleogene to Pliocene, from which the most robust conclusion that can be drawn is that at least some portions of the Greater Caucasus have undergone significant post-Miocene exhumation. Another study, concentrated on the western end of the Greater Caucasus (Vincent et al., 2011), reveals slow post-Eocene exhumation of modest magnitude (less than 5 km).

Here we present the results of a new low-temperature thermochronometric study of the central Greater Caucasus, between Mt. Elbrus and Kazbek (Fig. 4.1). This region is ideal for applying low-temperature thermochronometric techniques to studying strain accommodation within the Greater Caucasus. First, there are large exposures of silicic igneous and metamorphic rocks that yield the mineral phases necessary for low-temperature thermochronometry (Fig. 2.2). Second, high relief valleys, eroded by both fluvial and glacial processes, afford the opportunity to collect vertical transects in excess of 1 km. Finally, modern geodetic observations suggest that at this longitude strain north of the Turkish-Iranian plateau is accommodated almost exclusively within the Greater Caucasus, along a single thrust zone bounding the southern margin of the range. This differs from regions further to the east where strain accommodation is distributed across both the Lesser and the Greater Caucasus, and on both south and north verging thrust systems bounding both sides of the Greater Caucasus range (Fig. 4.1 and 4.10).

2.3 Low-temperature Thermochronometry

We present new apatite (U-Th)/He, apatite fission-track, zircon (U-Th)/He, zircon fission-track, and K-feldspar $^{40}Ar/^{39}Ar$ ages for the central Greater Caucasus,

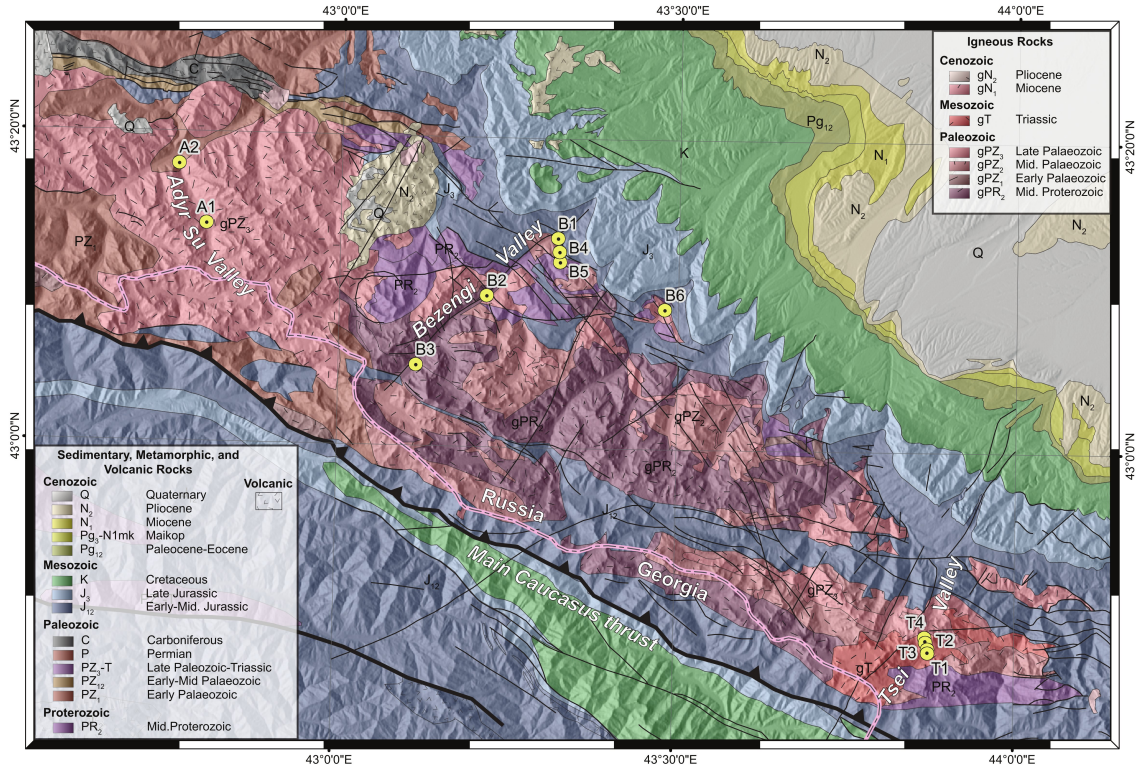

Figure 2.2: Map of the central Greater Caucasus with locations of low-temperature thermochronometry samples shown as yellow dots. Geology modified after Pismennyj (2002), Gamkrelidze and Kakhadze (1959) and Nalivkin (1976).

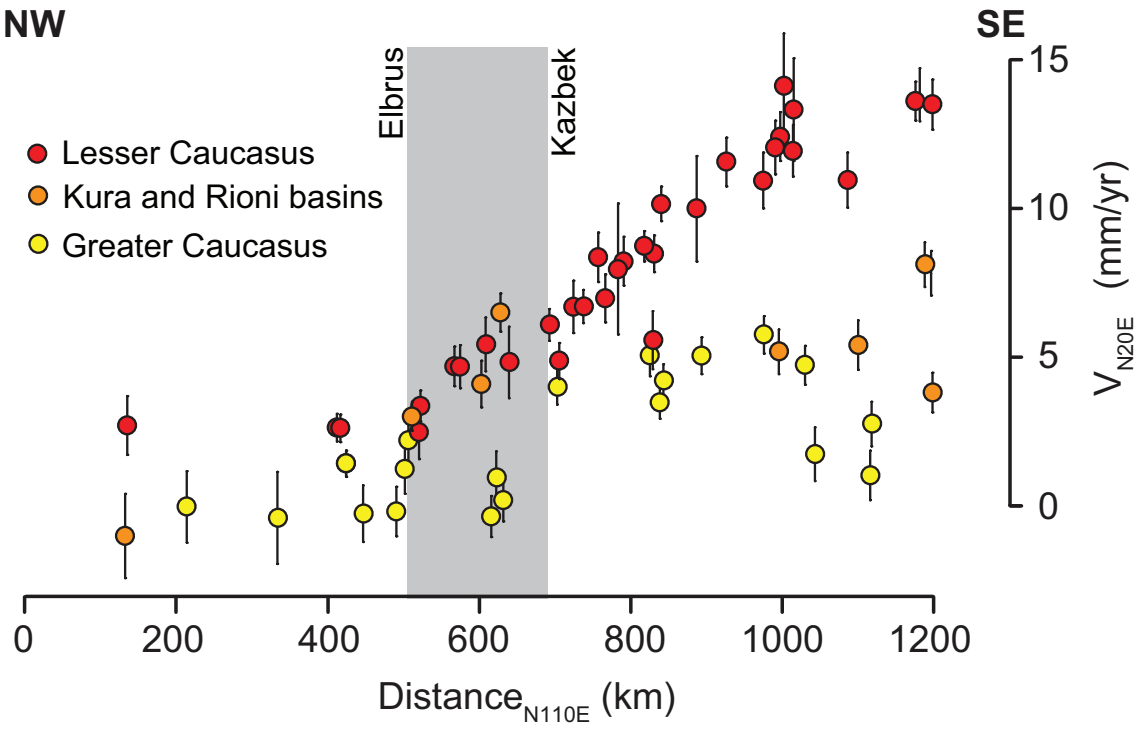

Figure 2.3: Caucasus region GPS velocities (Reilinger et al. (2006); Kadirov et al. (2008)). Velocities in the N20E (plate-convergence parallel) direction are shown plotted against orogen-strike-parallel distance (N110E). Color-coding of GPS velocities as in Fig. 4.1. Present-day strain distribution varies along strike of the Caucasus. West of Mt. Elbrus, little or no strain is accommodated across the Caucasus (GPS velocities are within error of stable Eurasia). Between Mt. Elbrus and Mt. Kazbek, strain is localized on the Main Caucasus thrust (Greater Caucasus velocities are within error of stable Eurasia; Lesser Caucasus and Kura/Rioni basin velocities are indistinguishable at 3–5 mm/yr with respect to Eurasia). East of Mt. Kazbek, strain is broadly distributed, with Greater Caucasus sites moving several mm/yr with respect to stable Eurasia, likely due to shortening in the north-verging fold-and-thrust belt in Dagestan, and considerable shortening between the Lesser Caucasus and both the Kura Basin and the Greater Caucasus.

alongside existing apatite fission-track ages (Kral and Gurbanov, 1996), to derive the long-term spatial and temporal patterns of exhumation of the range. These low-temperature thermochronometers have closure temperatures of $\sim 70°C$ (apatite (U-Th)/He, Wolf et al. (1996)), $\sim 110°C$ (AFT, Gleadow et al. (1983)), $\sim 180°C$ (zircon (U-Th)/He, Reiners et al. (2003)), $\sim 240°C$ ($^{40}Ar/^{39}Ar$, Foland (1994)), and ~ 232–$342°C$ (ZFT, Tagami et al. (1998)), although these estimates vary with grain size, cooling rate and radiation damage (e.g. Farley and Stockli, 2002; Dodson, 1973; Shuster et al., 2006; Flowers et al., 2009). This suite of thermochronometers samples cooling related to exhumation through the upper $\sim$10 km of the crust, depending upon the geothermal gradient, and is most relevant to understanding the recent thermal evolution of the range.

Samples were collected from igneous and metamorphic rocks, primarily granitoids and granite gneisses, likely to yield sufficient quantities of apatite and zircon for analysis. Elevation transects (e.g. Wagner and Reimer, 1972; Gallagher et al., 2005) were collected where significant topographic relief was present within a single igneous or metamorphic unit. Structural complexities within the Greater Caucasus basement rocks and poor constraints on sample paleodepth limited the application of this sampling strategy elsewhere within the range. Instead, multiple low-temperature thermochronometers were analyzed for individual samples to derive a continuous cooling path (e.g. McAleer et al., 2009). As discussed below, not all samples yielded a complete suite of reset cooling ages, and some higher-temperature thermochronometric results are consistent with the presumed age of igneous crystallization or peak metamorphism. These results are obviously not reflective of the Cenozoic evolution of the Greater Caucasus, but do provide constraints on the maximum amount of exhumation that these rocks could have experienced during the Cenozoic.

2.3.1 Analytical Methods

All samples were collected after removal of the outer few centimeters of rock to prevent inclusion of material affected by forest fires or lightning (Mitchell and Reiners, 2003). Rocks were crushed and pulverized, and mineral concentrates were made using standard magnetic and density techniques. Individual mineral grains of apatite and zircon were handpicked from the concentrates, with care taken to avoid comminuted grains or grains with inclusions visible under 200× magnification.

Apatite (U-Th)/He analyzes were conducted on single apatite grains at the Caltech Noble Gas Laboratory using standard procedures (Farley and Stockli, 2002). Sample aliquots were outgassed using a Nd-YAG laser (House et al., 2000) and ^{4}He was measured by ^{3}He spike using a quadrupole mass spectrometer. ^{238}U, ^{235}U, ^{232}Th and ^{147}Sm were measured using isotope dilution ICP mass spectrometry (Farley and Stockli, 2002). Reproducibility of analytical results was constrained by 4–6 replicate analyses. Analytical uncertainty of apatite (U-Th)/He ages is $\sim$5% (1σ) based on instrument precision and error in the alpha ejection correction (Farley et al., 1996). The Durango fluorapatite standard ((U-Th)/He age of 31.4 Ma (McDowell et al., 2005)) was analyzed in all sample runs to check age accuracy. The reported error for each sample is the standard deviation of the replicate analyses, which typically exceeded the analytical uncertainty, as has previously been observed for geologic samples (e.g. Farley and Stockli, 2002). Two outliers were excluded from the data set after failing the Q-test (Dean and Dixon, 1951) at the 95% level of confidence (Tables 2.1 and A.1). Undetected microinclusions of U- and Th-bearing phases within the apatite are the most likely explanation for the outlier ages.

Apatite and zircon fission-track ages were determined by Apatite to Zircon, Inc. (Donelick et al., 2005). Polished apatite grain mounts were immersed in 5.5N HNO_3

for 20 seconds at 21°C to reveal natural fission tracks. Zircon grain mounts were immersed in an eutectic melt of NaOH + KOH at $\sim$ 210°C ($\pm$10°C) for $\sim$34 hours. Track densities were counted and recorded. Concentrations of radiogenic elements were determined for the localities of counted natural fission tracks by measuring ^{238}U, ^{232}Th and ^{147}Sm via LA-ICP-MS (Hasebe et al., 2004). Apatite grain mounts were then irradiated with $\sim 10^7$ tracks/cm^2 from a ^{252}Cf source. Irradiated grain mounts were again immersed in 5.5N HNO_3 for 20 seconds at 21°C to reveal horizontal, confined fission tracks, and track lengths were then measured. Fission-track ages were determined using a modified decay equation that includes calibration for the LA-ICP-MS using the Durango fluorapatite standard (fission-track age of 30.6 Ma) and Fish Canyon zircon (28.5 Ma).

Zircon (U-Th)/He ages were measured on single grain aliquots at the Arizona Radiogenic Helium Dating Laboratory following standard protocols (Reiners et al., 2002, 2004). Euhedral zircons were wrapped in Nb foil and degassed by laser heating. He abundances were measured on a quadrupole mass spectrometer using ^{3}He isotope dilution. Degassed zircons were then dissolved and U and Th concentrations were measured on an ELEMENT 2 ICP-MS. (U-Th)/He ages were corrected for alpha ejection (Farley, 2002).

^{40}Ar/^{39}Ar analysis of potassium feldspars was performed at the University of Michigan Noble Gas Laboratory, following the methods described in Ownby et al. (2007). Samples were wrapped in pure Al foil and irradiated for 20 hr at location 5C at the McMaster Nuclear Reactor at McMaster University in Hamilton, Ontario in irradiation package mc19. Standard hornblende MMhb-1 was used as a neutron-fluence monitor with an assumed K-Ar age of 520.4 Ma (Samson and Alexander, 1987). Samples were incrementally heated with a Coherent Innova 5W continuous

argon-ion laser until complete fusion was achieved. Ar isotopes were measured using a VG1200S mass spectrometer with a source operating at 150 μA total emission and equipped with a Daly detector operating in analog mode. Fusion system blanks were run every five fusion steps and blank levels from argon masses 36 through 40 ($\sim 2 \times 10^{-14}, \sim 4 \times 10^{-14}, \sim 1 \times 10^{-14}, \sim 2 \times 10^{-14}$, and 2×10^{-12} ccSTP) were subtracted from sample gas fractions. Corrections were also made for the decay of ^{37}Ar and ^{39}Ar, for the production of ^{36}Ar from the decay of ^{36}Cl, as well as interfering nucleogenic reactions from K, Ca and Cl.

2.3.2 Modeling Methods

Thermal-history modeling was undertaken using HeFTy v. 1.6.7 software (Ketcham, 2005). This program implements a variety of forward models for fission-track density and annealing in apatite, as well as models of He diffusion in apatite and zircon. Observed apatite fission-track densities and c-axis projected track length distributions were modeled using a modification of the fanning Arrhenius model (Ketcham et al., 2007, 2009). Diffusion properties for He in apatite were modeled considering the effects of radiation damage on He diffusion (the RDAAM model, Flowers et al. (2009)). He diffusion in zircon was modeled following Reiners et al. (2004). Thermal models were constrained by modern surface temperatures and, where available, high-temperature constraints from ^{40}Ar/^{39}Ar of feldspars or zircon fission-track thermochronometry. No other constraints beyond the annealing or diffusion algorithms described above were imposed. Subsegment spacing of cooling paths were allowed to vary randomly, and monotonic cooling was not assumed. Viable thermal histories were found by simple Monte Carlo inversion. Forward models for randomly generated thermal histories were run until 100 acceptable (Ketcham, 2005) models were found.

For $^{40}Ar/^{39}Ar$, zircon fission-track, and samples on which only apatite (U-Th)/He were analyzed, blocking temperatures (Dodson, 1973) were determined assuming a constant cooling rate. We estimated blocking temperatures for a range of cooling rates between 1 and 25°C/My with the Closure program (Ehlers et al., 2005). Blocking temperatures for (U-Th)/He data were calculated following Farley (2000). Zircon fission-track fanning models (Tagami et al., 1998) and feldspar diffusion models (Foland, 1994) were used to estimate the blocking temperatures of zircon FT and $^{40}Ar/^{39}Ar$ systems. The blocking temperatures of the ZFT and $^{40}Ar/^{39}Ar$ systems were included, where appropriate, as box constraints in the HeFTy thermal modeling described above.

In cases where a change in cooling rate is observed, a finite-element exhumation model (Pecube, SVN version, Rev. 9, Braun (2003)) was used to calculate the time lag of the thermal signal following the exhumation rate change. The model was computed for a two-step exhumation history with a change of exhumation rate from 0.1 km/My to 1 km/My. Parameters of the model were set as follows: flat topography, 40 km^2/My diffusivity, 0.25°C/My heat production at surface, 60 km model thickness and 800°C temperature at the base of the model.

2.4 Results

Samples were collected from the northern side of the central Greater Caucasus, Russia, between Mt. Elbrus and Kazbek along three transects (Fig. 2.2). Two samples analyzed were collected in Adyr Su valley, a tributary of the Baksan river, east of Mt. Elbrus. Nine samples were collected near the village of Bezengi, along the Cherek-Balkarskii and Cherek-Bezengskii valleys, located within the Kabardino-Balkaria Nature Preserve (Fig. 2.2). The third transect was collected in Tsei valley,

located to the northwest of Kazbek. At Tsei, a complete vertical transect was sampled, while along-valley transects were sampled at Adyr Su and Bezengi.

2.4.1 Adyr Su

The Adyr Su river drains northward from the Main Caucasus Ridge, which is the border between Russia and Georgia (Fig. 2.2). This river is situated completely within the crystalline core of the range. The higher of the two samples (A1) was collected from a granite of presumed mid- to late Paleozoic age (Gamkrelidze and Kakhadze, 1959). A lower sample (A2), was collected down valley, away from the axis of the range. This sample was collected from a K-feldspar-rich granitoid, which is a part of a Precambrian–early Paleozoic metamorphic gneiss complex (Gamkrelidze and Kakhadze, 1959).

$^{40}Ar/^{39}Ar$ ages from sample A1 are Early Permian (∼291 Ma), consistent with published crystallization ages of nearby granites (Gamkrelidze and Kakhadze, 1959). Zircon fission-track ages from this sample yield a slightly younger Middle Triassic age (∼230 Ma), possibly representative of modest exhumation at this time. Sample A2 yields an Early Silurian (∼433 Ma) zircon fission-track age, consistent with zircon U-Pb ages from orthogneiss in the adjacent Kyrtyk valley (Somin, 2007b), and possibly dating gneiss formation.

Lower temperature thermochronometers from Adyr Su reveal a significantly younger portion of the thermal history. Zircon (U-Th)/He and apatite fission-track ages from sample A1 are 24.06 ± 0.49 and 5.2 ± 0.6 Ma, respectively (Table 2.1). These ages are interpreted as resulting from Cenozoic exhumation associated with uplift and erosion of the Greater Caucasus. Thermal modeling of these data reveals rapid cooling at $\sim 25°C$/My since $\sim$ 5 Ma. The rate of cooling prior to 5 Ma is less well resolved, but appears to be negligible cooling, with reheating permissible. Sample A2 yielded

Table 2.1: Summary of the central Greater Caucasus low-temperature thermochronometry results

Sample	Longitude °N	Latitude °E	Altitude m	AHe Ma[a] (52–73°C)[c]	AFT Ma[b] (98–124°C)[c]	ZHe Ma[b] (162–192°C)[c]	ZFT Ma[b] (210–350°C)[d]	$^{40}Ar/^{39}Ar$ Ma[b] (221–258°C)[c]
A1	42.801008	43.235924	2370		5.2 ± 0.6	24.06 ± 0.49	230.4 ± 13.1	291.2 ± 1.3
A2	42.758738	43.298983	1690		5.1 ± 0.6	88.93 ± 1.81	433.0 ± 19	
B1	43.320785	43.226316	1357	16.81 ± 3.36	21.8 ± 1.1	188.5 ± 3.87	293.4 ± 12.4	250.0 ± 1.2
B2	43.217135	43.163385	1687	4.06 ± 0.4	3.64 ± 0.35			
B3	43.114502	43.087557	2470	12.16 ± 1.11	7.64 ± 0.52			
B4	43.323375	43.211909	1846	11.64 ± 1.75				
B5	43.324428	43.200743	2359	19.03 ± 2.08				
B6	43.480113	43.151325	1052	13.55 ± 2.39				
T1	43.873633	42.785572	2200	2.55 ± 0.45	6.23 ± 0.98	20.4 ± 0.39		
T2	43.873080	42.789768	2421	2.05 ± 0.52				
T3	43.870518	42.797055	2994	1.88 ± 0.63		32.04 ± 0.72		
T4	43.869105	42.802727	3456	1.67 ± 0.21				

[a] Standard error is calculated from replicate analyses.
[b] Standard error is estimated analytical error.
[c] Range of closure temperatures for cooling rates between 1 and 25°C/My.
[d] Range of closure temperatures predicted by various models (see text) for cooling rates between 1 and 25°C/My.

zircon (U-Th)/He and apatite fission-track ages of 88.93 ± 1.81 and 5.1 ± 0.6 Ma. Differences in zircon (U-Th)/He ages between samples A1 and A2 may reflect differences in paleodepth resulting from structural complexity in the crystalline basement. The Coniacian zircon (U-Th)/He age is consistent with a regional unconformity that developed across the northern Greater Caucasus in Albian–Santonian time (e.g. Pismennyj, 2002). Thermal modeling of the zircon (U-Th)/He and apatite fission-track data for sample A2 (Fig. 2.4) indicates cooling at a rate of 0.7 °C/My prior to ∼5 Ma, followed by cooling at a rate of 20°C/My to the present.

2.4.2 Bezengi

The Cherek-Bezengi valley lies east of Adyr Su, and crosses almost the whole width of the crystalline core of the Greater Caucasus in a northeast-southwest direction (Fig. 2.2). The Cherek-Bezengi River drains the Bezengi Massif, which overlies the Main Caucasus thrust, and in which is exposed Proterozoic and Paleozoic metamorphic and igneous rocks. At its northernmost end, the river exposes Early Jurassic and younger Paratethys-related strata, unconformably overlying the older metamorphic infrastructure.

The southernmost sample from Bezengi, B3, was collected from Mesoproterozoic granitoids and yielded a 12.16 ± 1.11 Ma apatite (U-Th)/He age and a 7.64 ± 0.52 Ma apatite fission-track age (Table 2.1). An explanation for the inverse relationship observed between the thermochronometric ages and commonly cited closure temperatures for this sample is not readily apparent. Recent radiation damage models that predict an increase in apatite (U-Th)/He closure temperature for apatites with high uranium concentrations and slow cooling rates (<0.1°C/My; Shuster et al., 2006; Shuster and Farley, 2009; Flowers et al., 2009) offer one possible solution, but U concentrations in sample B3 are not significantly higher than those of other samples

in the region (Table A.1). Another possible explanation could be eU concentration zoning (Farley and Stockli, 2002). No forward thermal model could be found that adequately fit both the apatite fission-track and (U-Th)/He data, however, a rough estimate for cooling rate, averaged over the last 10 My is 5 to 15°C/My.

Sample B2, from a schist near the central portion of the crystalline core, yielded Pliocene apatite fission-track and (U-Th)/He ages (3.64 ± 0.35 and 4.06 ± 0.4 Ma; Table 2.1). Thermal modeling indicates rapid cooling at rates of ∼25°C/My since at least 4 Ma. No high temperature thermochronometers, or older fission tracks, constrain the pre-Pliocene thermal evolution of this sample (Fig. 2.4).

The northernmost sample, B1, was collected from Early Carboniferous granite, immediately beneath unconformably overlying Jurassic shallow-marine sedimentary rocks (Pismennyj, 2002). As at Adyr Su, higher temperature thermochronometers, zircon fission-track and potassium feldspar $^{40}Ar/^{39}Ar$, yield Permian to earliest Triassic ages (293.4 ± 12.4 Ma and 250.0 ± 1.2 Ma, respectively; Table 2.1), consistent with published crystallization ages (Pismennyj, 2002). The zircon (U-Th)/He age (188.5 ± 3.87 Ma; Table 2.1) of sample B1 records a relatively old thermal event, potentially related to exhumation during Jurassic orogeny, or perhaps simply reflective of long-term slow erosion and cooling.

Low temperature data from apatite fission-track and apatite (U-Th)/He yield ages of 21.8 ± 1.1 and 16.81 ± 3.36 Ma, respectively (Table 2.1). Thermal modeling of sample B1 indicates slow cooling at a rate of 4°C/My during the last ∼20 My (Fig. 2.4). It should be noted that this sample does not record any changes in cooling rate younger ∼16 Ma, the time at which it cooled below the closure temperature for apatite (U-Th)/He. Potential thermal paths for sample B1 between 50 and 20 Ma are poorly constrained, but could not have exceeded 150°C, and are inconsistent

with a constant cooling rate from 50 Ma to the present (Fig. 2.6). Three additional apatite (U-Th)/He ages from nearby samples (B4, B5 and B6) yield results similar to those from sample B1 (Table 2.1), and were not further modeled.

2.4.3 Tsei

Four samples were collected from a Late Triassic granodiorite (Pismennyj, 2002) along the north wall of the Tsei valley, on a 45° transect over a vertical distance of ∼1300 m. All thermochronometers from this sample reflect Cenozoic cooling. Zircon (U-Th)/He ages from samples T1 (2200 m) and T3 (2994 m) are 20.4 ± 0.39 Ma and 32.04 ± 0.72 Ma, respectively (Table 2.1). Given the elevation and age difference between these two samples, the average rate of exhumation from 30 to 20 Ma was ∼ 80 m/My. If we assume a geothermal gradient of 20°C/km, this is equivalent to a cooling rate of 1.6°C/My during this time period. Apatite (U-Th)/He ages are essentially invariant with elevation across the transect and are ∼2 Ma (Table 2.1), suggesting rapid passage through the closure isotherm (∼70°C) at this time. An apatite fission-track age of 6.23 ± 0.98 Ma was determined on the lowest sample (T1). Modeling of the thermochronometric data for sample T1 indicates a change in cooling rate from less than 3°C/My to 20°C/My at ∼5 Ma (Fig. 2.4).

2.5 Discussion

2.5.1 Amount, Rate and Timing of Exhumation of the Greater Caucasus

The thermochronometric data presented above yield new insights into the amount, timing, and rate of late Cenozoic exhumation of the Greater Caucasus. Higher temperature thermochronometers, specifically zircon fission-track and potassium feldspar $^{40}Ar/^{39}Ar$, throughout the central Greater Caucasus yield late Paleozoic to earliest Mesozoic cooling ages. These ages are consistent with published K-Ar and $^{40}Ar/^{39}Ar$

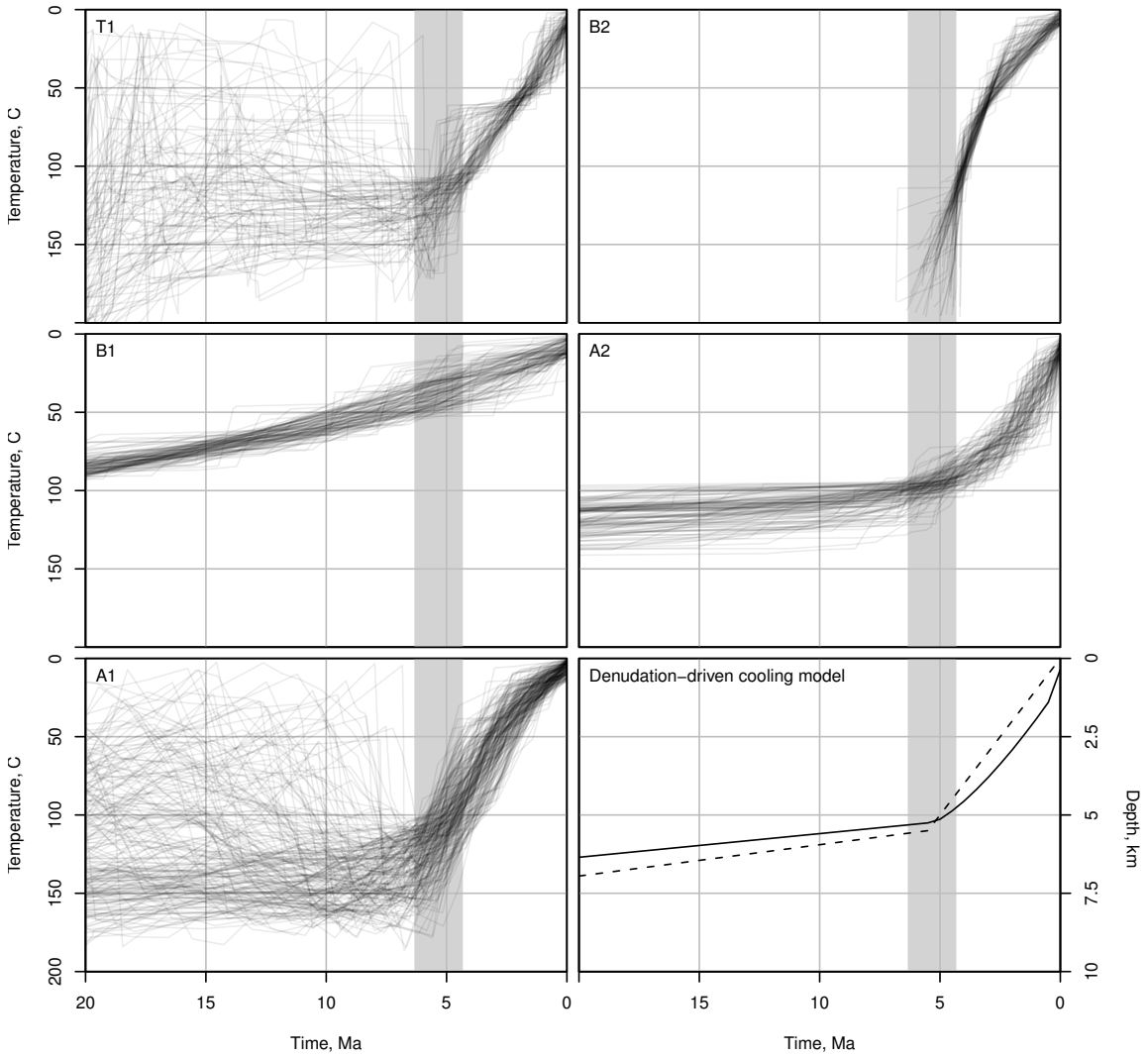

Figure 2.4: Randomly generated thermal histories satisfying low-temperature thermochronometry data (Tables A.1, A.2 and A.3) for samples that have at least apatite fission-track lengths measured. The gray band is centered on Miocene-Pliocene boundary (5.3 Ma). Samples A1, A2 and T1 clearly record the onset of rapid cooling at this time. Sample B1 has cooled past the sensitivity range of the analyzed thermochronometers ($< 50°$C) by 5 Ma, and so it does not record any change in cooling rate at this time. Sample B2, on the other hand, appears to have been hotter than the partial annealing zone of apatite at 5 Ma, and thus only records rapid cooling since $\sim$5 Ma. The lower right panel displays a cooling path (solid line) resulting from an increase in exhumation rate at the Miocene-Pliocene boundary from 0.1 to 1 km/My (dashed line shows depth below the surface), predicted from Pecube model (Braun, 2003).

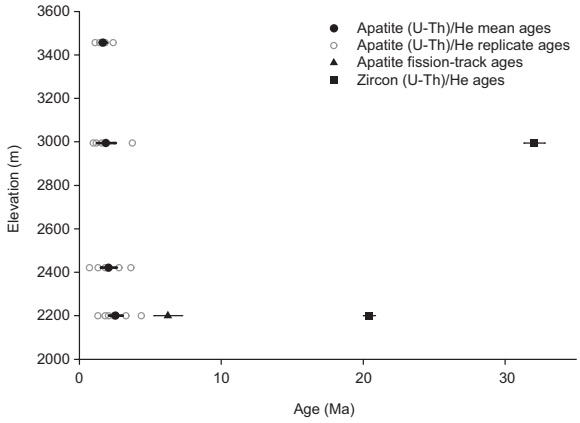

Figure 2.5: Low-temperature thermochronometric age data from the Tsei valley plotted as a function of sample elevation (samples T1–T4, T1 being the lowermost). Zircon (U-Th)/He reveal slow (∼4°C/My) cooling between 20 and 30 Ma. Elevation invariant apatite (U-Th)/He ages indicate rapid, but unquantifiable, cooling in the past ∼2 Ma. Results of thermal modeling of the lowest elevation samples are shown in Fig. 2.4

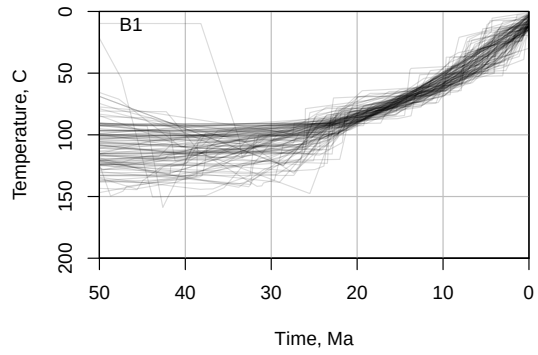

Figure 2.6: A selection of 100 randomly generated thermal histories satisfying apatite and zircon (U-Th)/He and apatite fission-track data (Tables A.1,A.2, and A.3) from the B1 sample in the Bezengi valley, indicating Oligocene change in cooling rate. See text for discussion.

dates from Paleozoic igneous and metamorphic rocks in the range (Somin, 2007a; Philippot et al., 2001), and thus provide an upper bound on the total amount of exhumation of the Greater Caucasus crystalline core. Given the wide range of zircon fission-track closure temperature estimates (e.g. Reiners and Brandon, 2006), we here use the closure temperature of potassium feldspar ($\sim 221-258$°C for cooling rates of 1–25°C) to determine the maximum amount of exhumation. Assuming a geothermal gradient of 20°C/km, no more than ∼12 km of exhumation of the Greater Caucasus has occurred since late Paleozoic time ($<$ 8 km for a geothermal gradient of 30°C/km). Several samples, however, yielded Cenozoic zircon (U-Th)/He ages, for which the closure temperature range is 162–192°C for cooling rates of 1–25°C. Given a 20°C/km (30°C/km) geothermal gradient, these results require ∼9 km (∼6 km), or roughly 75%, of the total exhumation of these samples to have occurred since the Oligocene. We have few constraints on the exhumation and/or burial paths taken by these samples throughout the Mesozoic, and do not imply that our results require a simple and monotonic exhumation history. However, depending on the geothermal gradient and cooling rate, 6–12 km of exhumation has occurred in the most deeply exposed portions of the central Greater Caucasus since ∼20–30 Ma. Some samples, particularly on the flanks of the range, exhibit significantly less cooling (e.g. sample B1), and may have experienced no more than several kilometers of exhumation in late Cenozoic time. Samples from the northern flank of the range have experienced lesser amounts of exhumation than those to the south, likely reflecting the structural position of the northern samples on the limb of the south-vergent anticlinorial structure that defines the range as a whole.

The rate of cooling of the Greater Caucasus is primarily constrained by thermal modeling of samples for which multiple thermochronometers were analyzed (Ta-

ble 2.1). Four such samples (Fig. 2.4) reveal rapid exhumation at ∼20°C/My in post-Miocene time. The vertical transect at Tsei (Fig. 2.5) reveals cooling ages that are statistically invariant with elevation, consistent with rapid, but unquantifiable cooling rates since 2 Ma. Slower rates of cooling prior to 5 Ma are apparent in two multi-thermochronometer samples (Fig. 2.4, samples A2 and B1), which yield cooling rates of ∼0–4°C/My since 20 Ma. Thermal models for two samples, A1 and T1, do not exclude the possibility of rapid cooling and reburial during Miocene time. However, thermal models for samples A2 and B1 do provide constraints that preclude such a complex thermal history. These modeling constraints are consistent with the geologic record, which contains no significant unconformities in Miocene time. A constrained thermal model, imposing a monotonic cooling path for samples A2 and B1, can therefore be imposed (Fig. 2.7). The constrained models for samples A1 and T1 suggest a change in cooling rate from 4°C/My to 20°C/My at 5 Ma. Zircon (U-Th)/He dates from the vertical transect at Tsei extend pre-Pliocene slow cooling (∼4°C/My) back to ∼30 Ma. Sample B1, from the northern edge of the range, provides a thermal history back to ∼50 Ma that requires a rate of cooling slower than ∼4°C/My prior to ∼30 Ma (Fig. 2.6).

No single sample from this dataset provides a complete Cenozoic thermal history for the central Greater Caucasus, but, taken as a group, such a history can be constructed. The earliest thermal history of the Greater Caucasus is the least well-constrained, but data from sample B1 are consistent with isothermal holding or extremely slow exhumation ($<$ 1°C/My) between 50 and 30 Ma. At 30 Ma an increase in cooling rate to ∼3–4°C/My is observed in this sample. This is consistent with post-30 Ma cooling rates observed in several other samples (this study and Vincent et al., 2011). Rapid cooling at ∼20°C/My begins at ∼5 Ma, and is observed

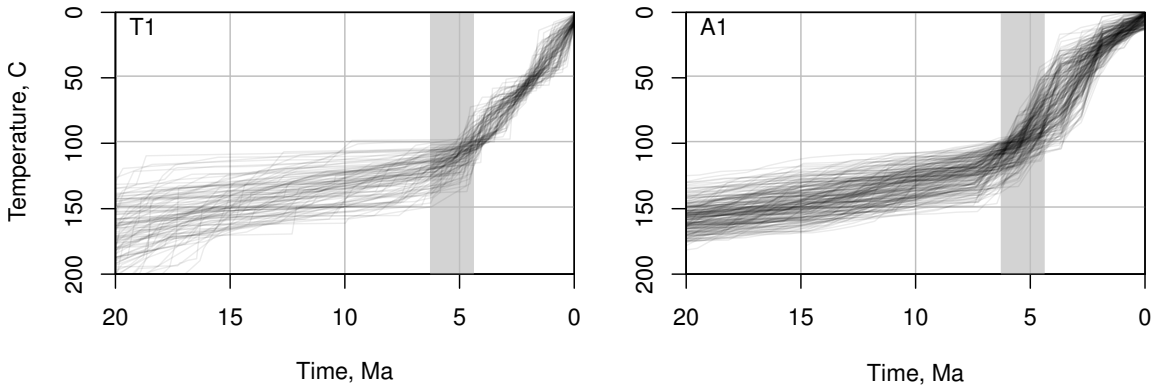

Figure 2.7: Thermal models for samples A1 and T1 subject to monotonic cooling constraints, as implied by adjacent thermochronometric samples and geologic evidence (see Fig. 2.4 and text for additional discussion).

in samples from all three transects. In addition, young (∼2 Ma) apatite (U-Th)/He ages at Tsei imply that rapid cooling in this area has continued to the present at rates exceeding 30°C/My. This may reflect, in part, increased glacial erosion of the range in late Pliocene and Pleistocene time.

2.5.2 Spatial variations in exhumation of the Greater Caucasus

Our complete Cenozoic history of the amount, rates, and timing of exhumation of the central Greater Caucasus differ significantly from studies of the western Greater Caucasus (Vincent et al., 2011). Both studies identify an exhumational event beginning in late Eocene or Oligocene time, and yield similar rates of exhumation, as derived from thermochronometric data, throughout the Oligocene and Miocene. In the western Greater Caucasus, however, the core of the range appears to undergo a reduction in the rate of exhumation in Pliocene and Pleistocene time, limiting the total amount of exhumation to ∼2.5 km (Vincent et al., 2011). Results from the core of the central Greater Caucasus reveal an almost opposite Plio-Pleistocene history, with significant increases in exhumation rates during this time, resulting in substantially greater total amounts of exhumation. Our results, in combination with

the data from the western Greater Caucasus (Vincent et al., 2011), appear to confirm suggestions from earlier work (Kral and Gurbanov, 1996) that the western and central Greater Caucasus have remarkably different exhumational histories. This variability may be a result of differential shortening along the range due to the westward extrusion of the Anatolia, which may accommodate a significant fraction of the Arabia-Eurasia convergence at the longitude of the western Greater Caucasus. The resulting differential convergence north of the Anatolia is then either diffusely consumed in the western Lesser Caucasus or accommodated by the hypothesized Borjomi-Kazbek strike-slip fault (Fig. 4.1; Philip et al., 1989).

2.5.3 Topographic growth of the Greater Caucasus

Deriving rates of topographic growth from rates of exhumation is not straightforward (e.g. England and Molnar, 1990). Nonetheless, rates of exhumation across the Greater Caucasus from 30–5 Ma are low, ∼0.1–0.2 mm/yr (Fig. 2.8), much lower than those typically observed in active orogenic systems (e.g. Burbank, 2002). Cooling rates from thermochronometric sampling in the western Greater Caucasus are of similar magnitude to those reported here (Vincent et al., 2011). These slow rates, combined with the observation that at least the eastern Greater Caucasus region remained below sea-level prior to the late Miocene (Kopp and Shcherba, 1985), suggest that the Greater Caucasus did not form a significant topographic barrier during Oligocene or Miocene time. Rapid exhumation of the central Greater Caucasus, at rates consistent with those observed in active orogens (e.g. Burbank, 2002) began in late Miocene to early Pliocene time (Fig. 2.8). This change is correlative with the onset of deposition of continental conglomerates on the margins of the Greater Caucasus (e.g. Khain, 1994; Saintot et al., 2006) and an increase in sediment derived from the Greater Caucasus (Morton et al., 2003). Together, these data suggest that

the Greater Caucasus became a high-standing orogen no earlier than Pliocene time.

2.5.4 Relationship of Exhumation in the Greater Caucasus to Regional Tectonics of the Arabia-Eurasia Collision

Given the timing and rates of exhumation described above, it seems pertinent to query the relationship between exhumation of the Greater Caucasus and tectonic and climatic events along the Arabia-Eurasia plate boundary. The earliest observed phase of exhumation, at ∼30 Ma, is consistent with stratigraphic and thermochronometric evidence from the western Greater Caucasus suggesting that the range had begun to uplift and was subaerial at this time (Vincent et al., 2007, 2011). This uplift has been interpreted as a result of the Arabia-Eurasia collision, which several estimates place at the end of Eocene (e.g. Saintot and Angelier, 2002; Allen and Armstrong, 2008), largely on the basis of deformation in the Greater Caucasus. However, such an explanation is problematic, as combined plate and palinspastic reconstructions require the removal of ∼500 km of continental lithosphere (presumably via subduction) from the Eurasian margin to accommodate observed plate convergence if collision initiated at this time (McQuarrie et al., 2003).

Alternatively, it seems reasonable to explain the onset of exhumation in the Greater Caucasus in the late Eocene as a response to the initiation of subduction of the Greater Caucasus back arc basin (Zonenshain and Le Pichon, 1986). This basin used to lie between Eurasia and the Lesser Caucasus (Fig. 4.1; Zonenshain and Le Pichon, 1986). No remnants of the basin floor are preserved, but it was likely underlain by oceanic or transitional crust, as are the Black and Caspian seas (e.g. Knapp et al., 2004). The original width of the Greater Caucasus back arc basin is poorly constrained, but may have been as great as 900 km (Zonenshain and Le Pichon, 1986), potentially accounting for the removed lithosphere required in plate recon-

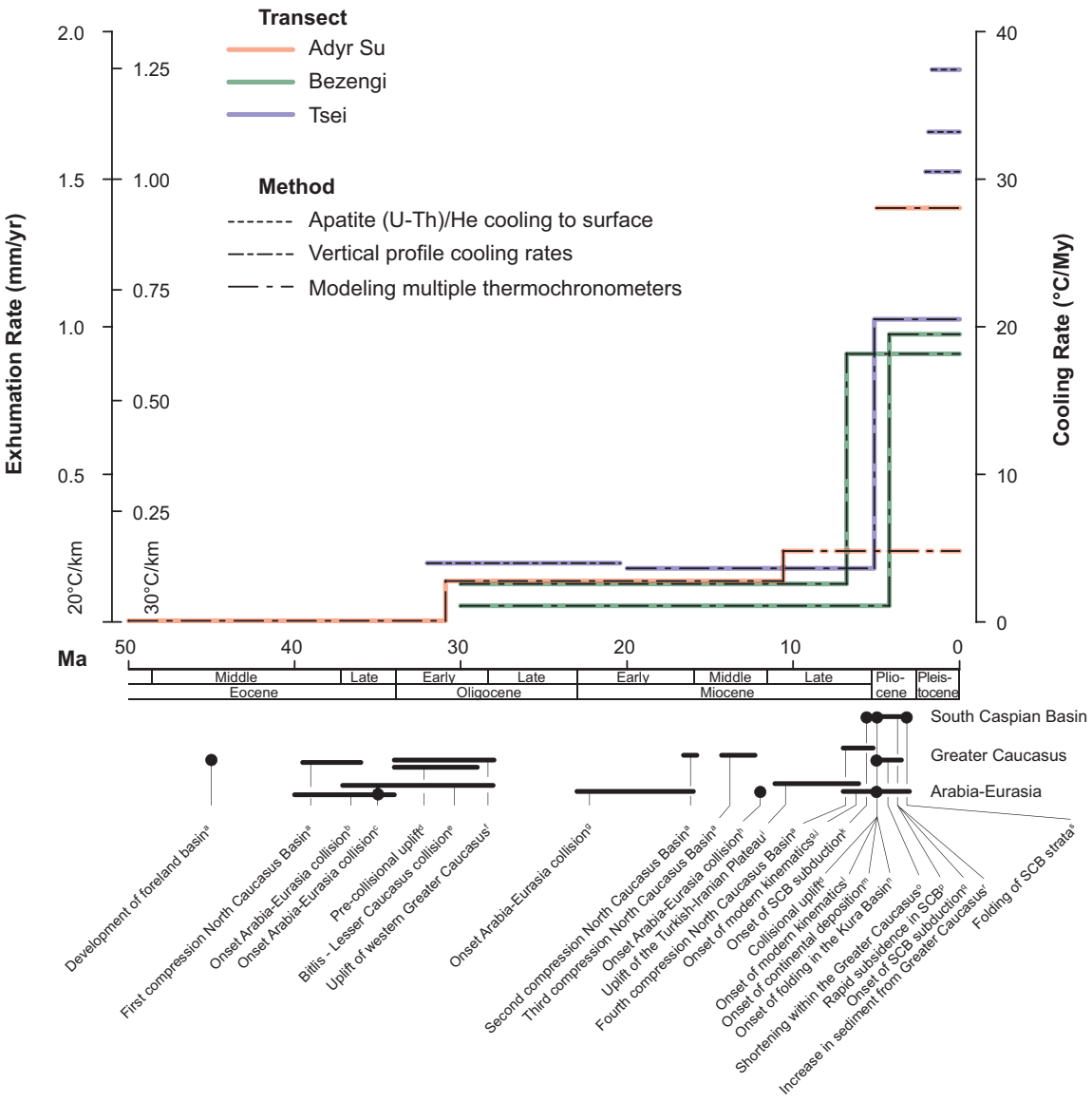

Figure 2.8: Summary of cooling rates from the central Greater Caucasus from a variety of methods (see Figs. 2.4 and 2.5 and text for discussion) and comparison to regional tectonic events. Break points for changes in cooling rates, where observed, were determined from modeled cooling paths using piece-wise linear regression. Cooling rates prior to 30 Ma are poorly constrained but indicate little to no cooling. All three transects exhibit cooling at ∼4°C/My from 30–5 Ma, and cooling at rates greater than ∼20°/My since 5 Ma. Exhumation rates are given for geothermal gradients of 20°/km and 30°/km. Changes in cooling rates observed in the central Greater Caucasus are consistent with a latest Eocene or early Oligocene onset of collision along the Arabia-Eurasia boundary and appear to change in response to a latest Miocene or early Pliocene plate reorganization. Regional tectonic events are from the following sources: [a]Mikhailov et al. (1999), [b]Saintot and Angelier (2002), [c]Allen and Armstrong (2008), [d]Kral and Gurbanov (1996), [e]Şengör et al. (2008), [f]Vincent et al. (2007), [g]Allen et al. (2004), [h]McQuarrie et al. (2003), [i]Şengör et al. (2003), [j]Copley and Jackson (2006), [k]Allen et al. (2002), [l]Westaway (1994), [m]Khain (1994), [n]Forte et al. (2010), [o]Philip et al. (1989), [p]Brunet et al. (2003), [q]Jackson et al. (2002), [r]Morton et al. (2003), [s]Devlin et al. (1999).

structions of this plate boundary (McQuarrie et al., 2003), if these reconstructions are correct (Fakhari et al., 2009).

Subduction of the Greater Caucasus back-arc basin may have initiated after the late Eocene "soft" collision of Arabia and the Pontide-Lesser Caucasus arc, buffered by the East Anatolian accretionary complex, (Şengör et al., 2003, 2008). The absence of Oligocene or Miocene volcanics on the edge of Eurasia or the northern margin of the Lesser Caucasus may indicate slow and/or flat-slab subduction (Pindell et al., 2005; Kay and Coira, 2009), or that the original width of the back arc basin is substantially less than has been proposed by Zonenshain and Le Pichon (1986).

Exhumation rates observed in the Oligocene remain constant across the central Greater Caucasus until Pliocene time, when they increase by a factor of four or more (Fig. 2.8). In many places along the Alpine-Himalayan orogen, Pliocene increases in exhumation rate and sediment supply have been interpreted as resulting from global climate change (Donnelly, 1982; Molnar and England, 1990; Hay et al., 2002; Molnar, 2004; Willett, 2010). Such an explanation appears unlikely in the Greater Caucasus, however, for several reasons. First, the timing of increase in the rate of exhumation in the central Greater Caucasus is not observed elsewhere in the range (Vincent et al., 2011). Second, the end of the Miocene is marked by a switch from marine to non-marine sedimentation in the eastern Greater Caucasus, reflecting topographic uplift (Kopp and Shcherba, 1985), and by a shift in sediment sources supplying the Caspian Sea from the Russian platform to the Greater Caucasus (Morton et al., 2003). Third, the structural evolution of the Greater Caucasus is opposite to that expected from climate-forced exhumation. Climate enhanced erosion acts on existing topographic barriers, removing gravitational loads, and thus localizing shortening on existing faults (e.g. Wobus et al., 2003). The Greater Caucasus, on the other hand, experience

a region-wide propagation of deformation outward into surrounding foreland basins (e.g. Forte et al., 2010), suggesting a tectonic, rather than climatic, force is driving the observed increase in exhumation rate.

Finally, the increase in exhumation rate within the Greater Caucasus is coincident with a major plate boundary reorganization (Fig. 2.8; Westaway, 1994; Allen et al., 2004; Copley and Jackson, 2006). This reorganization has been suggested to result from deformation along the edges of thickened and shortened Turkish-Iranian Plateau and Greater Caucasus crust (Allen et al., 2004). As noted above, it seems improbable that the Greater Caucasus were a high-standing mountain range prior to the time of this reorganization. Thus the uplift of the Turkish-Iranian plateau alone would have to be interpreted as the driving force of the post-Miocene reorganization of the plate boundary, including the uplift in the Greater Caucasus. Alternatively, reorganization of the Arabia-Eurasia orogen could be driven by the final closure of the Greater Caucasus back-arc basin in late Miocene time. Such a closure would result in the cessation of subduction of oceanic or transitional crust across much of the Arabia-Eurasia collision zone, and thus mark the onset of through-going "hard" continent-continent collision, from the Arabian shield to the Scythian platform. Given a relatively steady rate of Arabia-Eurasia convergence (McQuarrie et al., 2003), the disappearance of the last subduction zone would result in increased tectonic stresses throughout the orogen, resulting in plate boundary reorganization, including the initiation of Anatolian extrusion (Allen et al., 2004) and orogenesis in previously slowly deforming regions such as the Alborz (Axen et al., 2001) and Greater Caucasus.

2.6 Conclusions

Exhumation of the central Greater Caucasus occurred in two phases, beginning in Oligocene time. During the first phase, cooling rates increased from negligible values to ∼4°C/My, likely in response to the collision of Arabia with the Pontide-Lesser Caucasus arc. Cooling rates remained constant throughout the late Oligocene and Miocene until ∼5 Ma, when they rapidly increased to 20°C/My or more. This change coincides with a major plate boundary reorganization, as well as the onset of global climatic cooling. A variety of evidence suggests that rapid Pliocene exhumation of the central Greater Caucasus is tectonically driven, and we interpret this exhumation as resulting from either the closure of the Greater Caucasus basin and the onset of continent-continent collision across the Arabia-Eurasia plate boundary, or the migration of deformation away from the uplifted Turkish-Iranian plateau. If the former hypothesis is correct, then the post-Miocene reorganization is likely a result of the onset of "hard" continent-continent collision in this segment of the Arabia-Eurasia orogen.

2.7 Acknowledgements

Ken Farley, Pete Reiners, Chris Hall, Ray Donelick, and Paul O'Sullivan are thanked for assistance with thermochronometric analyses. Discussions with Eric Cowgill, Ibrahim Murtuzayev, and Adam Forte were valuable in improving our understanding of the geology of the Caucasus region. Andrei Khudolei provided assistance in obtaining geological maps of Russia. This work was funded by Civilian Research and Development Fund (AZG1-2840-BA-06) and National Science Foundation (EAR-0810067) grants to NAN and a Rackham International Student Fellowship from the University of Michigan to BA. Charles Verdel and Stephen Vincent provided

comments on an earlier version of the manuscript. Finally, we thank an anonymous reviewer and Gary Axen for their thoughtful reviews.

Bibliography

Alavi, M. Tectonics of the zagros orogenic belt of iran; new data and interpretations. *Tectonophys.*, 229(3-4):211–238, 1994.

Allen, M., Jackson, J. and Walker, R. Late Cenozoic reorganization of the Arabia-Eurasia collision and the comparison of short-term and long-term deformation rates. *Tectonics*, 23(2):TC2008, 2004. doi:10.1029/2003TC001530.

Allen, M. B. and Armstrong, H. A. Arabia-Eurasia collision and the forcing of mid-Cenozoic global cooling. *Palaeogeogr. Palaeoclimatol. Palaeoecol.*, 265(1–2):52–58, 2008. doi:10.1016/j.palaeo.2008.04.021.

Allen, M. B., Jones, S., Ismail-Zadeh, A., Simmons, M. and Anderson, L. Onset of subduction as the cause of rapid pliocene-quaternary subsidence in the south caspian basin. *Geology*, 30(9):775–778, 2002. ISSN 0091-7613.

Arpat, E. and Şaroğlu, F. The East Anatolian fault system; thoughts on its development. *Bulletin of the Mineral Research and Exploration Institute of Turkey*, 78:33–39, 1972.

Axen, G. J., Lam, P. S., Grove, M., Stockli, D. F. and Hassanzadeh, J. Exhumation of the west-central alborz mountains, iran, caspian subsidence, and collision-related tectonics. *Geology*, 29(6):559–562, 2001.

Banks, C. J., Robinson, A. G. and Williams, M. P. Structure and regional tectonics of the Achara-Trialet fold belt and the adjacent Rioni and Kartli foreland

basins, Republic of Georgia; regional and petroleum geology of the Black Sea and surrounding region. *AAPG Memoir*, 68:331–345, 1997.

Blythe, A. E., Burbank, D. W., Carter, A., Schmidt, K. and Putkonen, J. Plio-quaternary exhumation history of the central nepalese himalaya: 1. apatite and zircon fission track and apatite (u-th)/he analyses. *Tectonics*, 26(3):–3002, 2007. ISSN 0278-7407. doi:10.1029/2006TC001990.

Boztŭg, D. and Jonckheere, R. C. Apatite fission track data from central Anatolian granitoids (Turkey); constraints on Neo-Tethyan closure. *Tectonics*, 26:TC3011, 2007.

Braun, J. Pecube: a new finite-element code to solve the 3D heat transport equation including the effects of a time-varying, finite amplitude surface topography. *Comput. Geosci.*, 29:787–794, 2003. ISSN 0098-3004. doi:10.1016/S0098-3004(03)00052-9.

Braun, J. Quantitative constraints on the rate of landform evolution derived from low-temperature thermochronology; low-temperature thermochronology; techniques, interpretations, and applications. In Reiners, P. W. and Ehlers, T. A., editors, *Low-Temperature Thermochronology: Techniques, Interpretations, and Applications*, volume 58 of *Reviews in Mineralogy & Geochemistry*, pages 351–374. Mineralogical Society of America, 2005. ISBN 1529-6466.

Brunet, M.-F., Korotaev, M. V., Ershov, A. V. and Nikishin, A. M. The South Caspian Basin: a review of its evolution from subsidence modelling. *Sediment. Geol.*, 156:119–148, 2003. ISSN 0037-0738.

Burbank, D. W. Rates of erosion and their implications for exhumation. *Mineral. Mag.*, 66:25–52, 2002.

Clark, M. K. and Bilham, R. Miocene rise of the Shillong Plateau and the beginning of the end for the eastern Himalaya. *Earth Planet. Sci. Lett.*, 269:336–350, 2008.

Cloetingh, S., Ziegler, P., Bogaard, P., Andriessen, P., Artemieva, I., Bada, G., van Balen, R., Beekman, F., Ben-Avraham, Z., Brun, J.-P., Bunge, H., Burov, E., Carbonell, R., Facenna, C., Friedrich, A., Gallart, J., Green, A., Heidbach, O., Jones, A., Matenco, L., Mosar, J., Oncken, O., Pascal, C., Peters, G., Sliaupa, S., Soesoo, A., Spakman, W., Stephenson, R., Thybo, H., Torsvik, T., de Vicente, G., Wenzel, F. and Wortel, M. TOPO-EUROPE: The geoscience of coupled deep Earth-surface processes. *Global and Planetary Change*, 58(1-4):1 – 118, 2007. ISSN 0921-8181. doi:DOI: 10.1016/j.gloplacha.2007.02.008.

Copley, A. and Jackson, J. Active tectonics of the Turkish-Iranian plateau. *Tectonics*, 25(6):1–19, 2006.

Dean, R. B. and Dixon, W. J. Simplified statistics for small numbers of observations. *Anal. Chem.*, 23(4):636–638, 1951. ISSN 0003-2700.

Devlin, W. J., Cogswell, J. M., Gaskins, G. M., Isaksen, G. H., Pitcher, D. M., Puls, D. P., Stanley, K. O. and Wall, G. R. T. South Caspian basin: young, cool, and full of promise. *GSA Today*, 9(7):1–9, 1999.

Dewey, J. F., Hempton, M. R., Kidd, W. S. F., Şaroğlu, F. and Şengör, A. M. C. Shortening of continental lithosphere: the neotectonics of eastern Anatolia, a young collision zone. In Coward, M. P. and Ries, A. C., editors, *Processes of collision orogeny*, number 19 in Special Publication, pages 3–36. Geological Society of London, 1986.

Dodson, M. H. Closure temperature in cooling geochronological and petrological systems. *Contrib. Mineral. Petrol.*, 40(3):259–274, 1973.

Donelick, R. A., O'Sullivan, P. B. and Ketcham, R. A. Apatite fission-track analysis. In Reiners, P. W. and Ehlers, T. A., editors, *Low-Temperature Thermochronology: Techniques, Interpretations, and Applications*, volume 58, chapter Reviews in Mineralogy & Geochemistry, pages 49–94. Mineralogical Society of America, 2005.

Donnelly, T. W. Worldwide continental denudation and climatic deterioration during the late tertiary—evidence from deep-sea sediments. *Geology*, 10(9):451–454, 1982. ISSN 0091-7613.

Ehlers, T. A., Chaudhri, T., Kumar, S., Fuller, C. W., Willett, S. D., Ketcham, R. A., Brandon, M. T., Belton, D. X., Kohn, B. P., Gleadow, A. J. W., Dunai, T. J. and Fu, F. Q. Computational tools for low-temperature thermochronometer interpretation. In Reiners, P. W. and Ehlers, T. A., editors, *Low-Temperature Thermochronology: Techniques, Interpretations, and Applications*, volume 58 of *Reviews in Mineralogy & Geochemistry*, pages 589–622. Mineralogical Society of America, 2005.

England, P. and Molnar, P. Surface uplift, uplift of rocks, and exhuamtion of rocks. *Geology*, 18:1173–1177, 1990.

Ershov, A. V., Brunet, M.-F., Nikishin, A. M., Bolotov, S. N., Nazarevich, B. P. and Korotaev, M. V. Northern Caucasus basin: thermal history and synthesis of subsidence models. *Sediment. Geol.*, 156(1-4):95–118, 2003.

Fakhari, M. D., Axen, G. J., Horton, B. K., Hassanzadeh, J. and Amini, A. Revised age of proximal deposits in the Zagros foreland basin and implications for Cenozoic evolution of the High Zagros. *Tectonophysics*, 451:170–185, 2008. doi: 10.1016/j.tecto.2007.11.064.

Fakhari, M. D., Guest, B., Axen, G. and Horton, B. K. Evidence for significant dextral faulting within the High Zagros, Iran. In *Abstracts with Programs*, volume 41 of *Geological Society of America*, page 406. 2009.

Farley, K. A. Helium diffusion from apatite: General behavior as illustrated by Durango fluorapatite. *J. Geophys. Res.*, 105:2903–2914, 2000. doi: 10.1029/1999JB900348.

Farley, K. A. (U-Th)/He dating: Techniques, calibrations, and applications. In Porcelli, D., Ballentine, C. J. and Wieler, R., editors, *Noble Gases in Geochemistry and Cosmochemistry*, volume 47 of *Reviews In Mineralogy & Geochemistry*, pages 819–844. Mineralogical Society of America, 2002. ISBN 0-939950-59-6.

Farley, K. A. and Stockli, D. F. (U-Th)/He dating of phosphates: Apatite, monazite, and xenotime. In Kohn, M., Rakovan, J. and Hughes, J., editors, *Phosphates: Geochemical, Geobiological, and Materials Importance*, volume 48 of *Reviews In Mineralogy & Geochemistry*, pages 559–577. Mineralogical Society of America, 2002. ISBN 0-939950-60-X.

Farley, K. A., Wolf, R. A. and Silver, L. T. The effects of long alpha-stopping distances on (U-Th)/He ages. *Geochim. Cosmochim. Acta*, 60:4223–4229, 1996. ISSN 0016-7037.

Flowers, R. M., Ketcham, R. A., Shuster, D. L. and Farley, K. A. Apatite (U-Th)/He thermochronometry using a radiation damage accumulation and annealing model. *Geochim. Cosmochim. Acta*, 73(8):2347–2365, 2009. ISSN 0016-7037. doi:DOI: 10.1016/j.gca.2009.01.015.

Foland, K. A. Argon diffusion in feldspars. In Parsons, I., editor, *Feldspars and their reactions*, volume 421 of *NATO Advanced Science Institutes Series, Series C,*

Mathematical and Physical Sciences, pages 415–447. 1994. ISBN 0-7923-2722-5. ISSN 0258-2023.

Forte, A., Cowgill, E., Bernardin, T., Kreylos, O. and Hamann, B. Late Cenozoic deformation of the Kura fold-thrust belt, southern Greater Caucasus. *Geol. Soc. Am. Bull*, 122(3/4):465–486, 2010.

Gallagher, K., Stephenson, J., Brown, R., Holmes, C. and Fitzgerald, P. Low temperature thermochronology and modeling strategies for multiple samples 1: Vertical profiles. *Earth Planet. Sci. Lett.*, 237:193–208, 2005. ISSN 0012-821X. doi: 10.1016/j.epsl.2005.06.025.

Gamkrelidze, P. D. and Kakhadze, I. R. Caucasus Series K-38-VII. In *State Geological Map 1:200000*. USSR Geological Research Institute (VSEGEI), 1959. 1:200000.

Gleadow, A. J. W., Duddy, I. R., Lovering, J. F. and Griffith, B. R. Fission track analysis; a new tool for the evaluation of thermal histories and hydrocarbon potential; developing for the future. *The APEA Journal*, 23:93–102, 1983.

Golonka, J. Plate tectonic evolution of the southern margin of eurasia in the mesozoic and cenozoic. *Tectonophys.*, 381:235–273, 2004.

Guest, B., Stockli, D. F., Grove, M., Axen, G. J., Lam, P. S. and Hassanzadeh, J. Thermal histories from the central Alborz mountains, northern Iran: Implications for the spatial and temporal distribution of deformation in northern Iran. *Geol. Soc. Am. Bull*, 118(11-12):1507–1521, 2006. ISSN 0016-7606. doi:10.1130/B25819.1.

Hasebe, N., Barbarand, J., Jarvis, K., Carter, A. and Hurford, A. Apatite fission-track chronometry using laser ablation ICP-MS. *Chem. Geol.*, 207(3–4):135–145, 2004. ISSN 0009-2541. doi:10.1016/j.chemgeo.2004.01.007.

Hay, W. W., Soeding, E., DeConto, R. M. and Wold, C. N. The Late Cenozoic uplift - climate change paradox. *Int. J. Earth Sci.*, 91(5):746–774, 2002. ISSN 1437-3254. doi:10.1007/s00531-002-0263-1.

Hempton, M. Constraints on Arabian plate motion and extensional history of the Red Sea. *Tectonics*, 6(6):687–705, 1987. ISSN 0278-7407.

House, M. A., Farley, K. A. and Stockli, D. Helium chronometry of apatite and titanite using Nd-YAG laser heating. *Earth Planet. Sci. Lett.*, 183:365–368, 2000.

Jackson, J., Priestley, K., Allen, M. and Berberian, M. Active tectonics of the South Caspian basin. *Geophys. J. Int.*, 148(2):214–245, 2002. ISSN 0956-540X.

Jassim, S. Z. and Goff, J. C. *Phanerozoic development of the northern Arabian Plate.* Geology of Iraq. Dolin, Prague and Moravian Museum, Brno, Czech Republic, 2006. ISBN 8070282878.

Kadirov, F., Mammadov, S., Reilinger, R. and McClusky, S. Some new data on modern tectonic deformation and active faulting in Azerbaijan (according to Global Positioning System measurements). *Proceedings, The Sciences of the Earth, Azerbaijan National Academy of Sciences*, 1:82–88, 2008.

Kay, S. M. and Coira, B. L. Shallowing and steepening subduction zones, continental lithospheric loss, magmatism, and crustal flow under the Central Andean Altiplano-Puna Plateau. In Kay, S. M., Ramos, V. A. and Dickinson, W. R., editors, *Backbone of the americas: shallow subduction, plateau uplift, and ridge and terrane collision*, volume 204 of *Geological Society of America Memoir*, pages 229–259. 2009. ISBN 978-0-8137-1204-8. ISSN 0072-1069. doi:10.1130/2009.1204(11).

Ketcham, R. A. Forward and inverse modeling of low-temperature thermochronom-

etry data. *Reviews in Mineralogy and Geochemistry*, 58(1):275, 2005. doi: 10.2138/rmg.2005.58.11.

Ketcham, R. A., Carter, A., Donelick, R. A., Barbarand, J. and Hurford, A. J. Improved measurement of fission-track annealing in apatite using c-axis projection. *Am. Mineral.*, 92(5-6):789–798, 2007. ISSN 0003-004X. doi:10.2138/am.2007.2280.

Ketcham, R. A., Donelick, R. A., Balestrieri, M. L. and Zattin, M. Reproducibility of apatite fission-track length data and thermal history reconstruction. *Earth Planet. Sci. Lett.*, 284(3-4):504–515, 2009. ISSN 0012-821X. doi:DOI: 10.1016/j.epsl.2009.05.015.

Khain, V. *Geology of northern Eurasia*, volume 2. Phanerozoic fold belts and young platforms, chapter Alpine belt of southern Ex-USSR, pages 130–235. Beiträge zur regionalen Geologie der Erde, 1994.

Knapp, C. C., Knapp, J. H. and Connor, J. A. Crustal-scale structure of the South Caspian Basin revealed by deep seismic reflection profiling. *Mar. Pet. Geol.*, 21:1073–1081, 2004.

Kopp, M. L. Late Alpine collision tectonics of the Caucasus. In Leonov, J. G., editor, *The Greater Caucasus during the Alpine epoch*, pages 285–316. Geos, 2007.

Kopp, M. L. and Shcherba, I. G. Late Alpine development of the east Caucasus. *Geotectonics*, 19(6):497–507, 1985.

Kral, J. and Gurbanov, A. Apatite fission track data from the Great Caucasus pre-Alpine basement. *Chem. Erde*, 56:177–192, 1996.

Leonov, M. Tectonic-gravitational mixtites of the central segment of Southern slope

of the Greater Caucasus. In Leonov, J. G., editor, *The Greater Caucasus during the Alpine epoch*, pages 231–250. Geos, 2007.

McAleer, R. J., Spotila, J. A., Enkelmann, E. and Berger, A. L. Exhumation along the Fairweather fault, southeastern Alaska, based on low temperature thermochronometry. *Tectonics*, 28(1):TC1007, 2009.

McDowell, F. W., McIntosh, W. C. and Farley, K. A. A precise $^{40}Ar/^{39}Ar$ reference age for the Durango apatite (U-Th)/He and fission-track dating standard. *Chem. Geol.*, 214:249–263, 2005.

McQuarrie, N., Stock, J. M., Verdel, C. and Wernicke, B. P. Cenozoic evolution of Neotethys and implications for the causes of plate motions. *Geophys. Res. Lett.*, 30(20):2036, 2003. doi:10.1029/2003GL017992.

Mikhailov, V., Panina, L., Polino, R., Koronovsky, N., Kiseleva, E., Klavdieva, N. and Smolyaninova, E. Evolution of the North Caucasus foredeep: constraints based on the analysis of subsidence curves. *Tectonophys.*, 307(3-4):361–379, 1999. ISSN 0040-1951.

Milanovsky, E. E. and Khain, V. E. *Geological Structure of Caucasus*. MGU, Moscow, 1963.

Mitchell, S. G. and Reiners, P. W. Influence of wildfires on apatite and zircon (U-Th)/He ages. *Geology*, 31(12):1025–1028, 2003. doi:10.1130/G19758.1.

Molnar, P. Late cenozoic increase in accumulation rates of terrestrial sediment: How might climate change have affected erosion rates? *Annu. Rev. Earth Planet. Sci.*, 32:67–89, 2004. ISSN 0084-6597. doi:10.1146/annurev.earth.32.091003.143456.

Molnar, P. and England, P. Late Cenozoic uplift of mountain-ranges and global climate change—chicken or egg. *Nature*, 346(6279):29–34, 1990. ISSN 0028-0836.

Morton, A., Allen, M., Simmons, M., Spathopoulos, F., Still, J., Hinds, D., Ismail-Zadeh, A. and Kroonenberg, S. Provenance patterns in a neotectonic basin: Pliocene and Quaternary sediment supply to the South Caspian. *Basin Res.*, 15(3):321–337, 2003. ISSN 0950-091X.

Nalivkin, D. V. *Geological map of the USSR 1:500000*. Russian Geological Research Institute (VSEGEI), 1976.

Nikishin, A. M., Ziegler, P. A., Panov, D. I., Nazarevich, B. P., Brunet, M.-F., Stephenson, R. A., Bolotov, S. N., Korotaev, M. V. and Tikhomirov, P. L. Mesozoic and Cainozoic evolution of the Scythian platform-Black sea-Caucasus domain. In Ziegler, P., Cavazza, W., Robertson, A. and CrasquinSoleau, S., editors, *Peri-Tethys Memoir 6: Peri-Tethyan Rift/Wrench Basins And Passive Margins*, volume 186 of *Memoires du Museum National d Histoire Naturelle*, pages 295–346. 2001. ISBN 2-85653-528-3. ISSN 1243-4442.

Okay, A. I., Zattin, M. and Cavazza, W. Apatite fission-track data for the Miocene Arabia-Eurasia collision. *Geology*, 38(1):35, 2010. doi:10.1130/G30234.1.

Ownby, S., Granados, H. D., Lange, R. A. and Hall, C. M. Volcán Tancítaro, Michoacín, Mexico, $^{40}Ar/^{39}Ar$ constraints on its history of sector collapse. *J. Volcanol. Geotherm. Res.*, 161(1-2):1–14, 2007. ISSN 0377-0273. doi:DOI: 10.1016/j.jvolgeores.2006.10.009.

Philip, H., Cisternas, A., Gvishiani, A. and Gorshkov, A. The Caucasus: an actual example of the initial stages of continental collision. *Tectonophys.*, 161(1-2):1–21, 1989.

Philippot, P., Blichert-Toft, J., Perchuk, A., Costa, S. and Gerasimov, V. Lu-Hf and Ar-Ar chronometry supports extreme rate of subduction zone metamorphism deduced from geospeedometry. *Tectonophys.*, 342(1-2):23–38, 2001. ISSN 0040-1951. doi:DOI: 10.1016/S0040-1951(01)00155-X.

Pindell, J., Kennan, L., Maresch, W. V., Stanek, K.-P., Drapper, G. and Higgs, R. Plate-kinematics and crustal dynamics of circum-Caribbean arc-continent interactions: Tectonic controls on basin development in Proto-Caribbean margins. In *Caribbean-South American plate interactions, Venezuela*, pages 7–52. Geol. Soc. Amer. Special Paper 394, 2005.

Pismennyj, A. N. Caucasus Series K-38-VIII,XIV. In *State Geological Map 1:200000*. Russian Geological Research Institute (VSEGEI), 2 edition, 2002. 1:200000.

Reilinger, R., McClusky, S., Vernant, P., Lawrence, S., Ergintav, S., Cakmak, R., Ozener, H., Kadirov, F., Guliev, I., Stepanyan, R., Nadariya, M., Hahubia, G., Mahmoud, S., Sakr, K., ArRajehi, A., Paradissis, D., Al-Aydrus, A., Prilepin, M., Guseva, T., Evren, E., Dmitrotsa, A., Filikov, S. V., Gomez, F., Al-Ghazzi, R. and Karam, G. GPS constraints on continental deformation in the Africa-Arabia-Eurasia continental collision zone and implications for the dynamics of plate interactions. *J. Geophys. Res.*, 111:B05411, 2006.

Reiners, P. W. and Brandon, M. T. Using thermochronology to understand orogenic erosion. *Annu. Rev. Earth Planet. Sci.*, 34(1):419–466, 2006. doi: 10.1146/annurev.earth.34.031405.125202.

Reiners, P. W., Ehlers, T. A., Mitchell, S. G. and Montgomery, D. R. Coupled spatial variations in precipitation and long-term erosion rates across the Washington Cascades. *Nature*, 426(6967):645–647, 2003.

Reiners, P. W., Farley, K. A. and Hickes, H. J. He diffusion and (U-Th)/He thermochronometry of zircon: initial results from Fish Canyon Tuff and Gold Butte. *Tectonophys.*, 349(1-4):297–308, 2002. ISSN 0040-1951. doi:DOI: 10.1016/S0040-1951(02)00058-6.

Reiners, P. W., Spell, T. L., Nicolescu, S. and Zanetti, K. A. Zircon (U-Th)/He thermochronometry: He diffusion and comparisons with $^{40}Ar/^{39}Ar$ dating. *Geochim. Cosmochim. Acta*, 68(8):1857–1887, 2004. ISSN 0016-7037. doi:DOI: 10.1016/j.gca.2003.10.021.

Robertson, A. H. F. Mesozoic-Tertiary tectonic-sedimentary evolution of a south Tethyan oceanic basin and its margins in southern Turkey; Tectonics and magmatism in Turkey and the surrounding area. *Geol. Soc. Spec. Pub.*, 173:97–138, 2000.

Robinson, A. G., Rudat, J. H., Banks, C. J. and Wiles, R. L. F. Petroleum geology of the Black Sea. *Mar. Pet. Geol.*, 13(2):195–223, 1996.

Saintot, A. and Angelier, J. Tectonic paleostress fields and structural evolution of the NW-Caucasus fold-and-thrust belt from Late Cretaceous to Quaternary. *Tectonophys.*, 357(1-4):1–31, 2002. ISSN 0040-1951. doi:DOI: 10.1016/S0040-1951(02)00360-8.

Saintot, A., Brunet, M.-F., Yakovlev, F., Sébrier, M., Stephenson, R. A., Ershov, A., Chalot-Prat, F. and McCann, T. The Mesozoic-Cenozoic tectonic evolution of the Greater Caucasus. In Gee, D. G. and Stephenson, R. A., editors, *European Lithosphere Dynamics*, volume 32 of *Memoirs*, pages 277–289. Geological Society of London, 2006. ISBN 1862392129; 9781862392120.

Samson, S. D. and Alexander, E. C. Calibration of the interlaboratory ^{40}Ar–^{39}Ar dating standard, MMhb-1. *Chem. Geol.*, 66(1-2):27–34, 1987. ISSN 0168-9622. doi:DOI: 10.1016/0168-9622(87)90025-X.

Şengör, A. M. C. and Kidd, W. S. F. Post-collisional tectonics of the Turkish-Iranian plateau and a comparison with Tibet. *Tectonophys.*, 55(3-4):361–376, 1979. ISSN 0040-1951.

Şengör, A. M. C., Özeren, M. S., Keskin, M., Sakinç, M., Özbakir, A. D. and Kayan, İ. Eastern Turkish high plateau as a small Turkic-type orogen: Implications for post-collisional crust-forming processes in Turkic-type orogens. *Earth-Science Reviews*, 90(1-2):1–48, 2008. ISSN 0012-8252. doi:10.1016/j.earscirev.2008.05.002.

Şengör, A. M. C., Özeren, S., Genç, T. and Zor, E. East anatolian high plateau as a mantle-supported, north-south shortened domal structure. *Geophys. Res. Lett.*, 30(24):8045, 2003.

Shuster, D. L. and Farley, K. A. The influence of artificial radiation damage and thermal annealing on helium diffusion kinetics in apatite. *Geochim. Cosmochim. Acta*, 73(1):183–196, 2009. ISSN 0016-7037. doi:DOI: 10.1016/j.gca.2008.10.013.

Shuster, D. L., Flowers, R. M. and Farley, K. A. The influence of natural radiation damage on helium diffusion kinetics in apatite. *Earth Planet. Sci. Lett.*, 249(3-4):148–161, 2006. ISSN 0012-821X. doi:10.1016/j.epsl.2006.07.028.

Somin, M. L. Alpine deformation of basement complexes and tectonic style of the Greater Caucasus. In Leonov, J. G., editor, *The Greater Caucasus during the Alpine epoch*, pages 111–140. Geos, 2007a.

Somin, M. L. Main features of structure of pre-Alpine basement of the Greater

Caucasus. In Leonov, J. G., editor, *The Greater Caucasus during the Alpine epoch*, pages 15–38. Geos, 2007b.

Stocklin, J. Possible ancient continental margins in Iran. In Burk, C. A. and Drake, C. L., editors, *The Geology of Continental Margins*, pages 873–887. Springer-Verlag, New York, United States (USA), 1974.

Tagami, T., Galbraith, R. F., Yamada, R. and Laslett, G. M. Revised annealing kinetics of fission tracks in zircon and geological implications. In Van den haute, P. and De Corte, F., editors, *Advances in fission-track geochronology*, volume 10 of *Solid Earth Sciences Library*, pages 99–112. 1998. ISBN 0-7923-4904-0. International Workshop on Fission-Track Dating, Ghent, Belgium, 1996.

Vincent, S. J., Carter, A., Lavrishchev, V. A., Price, S. P., Barabadze, T. G. and Hovius, N. The exhumation of the western Greater Caucasus: a thermochronometric study. *Geol. Mag.*, pages 1–21, 2011. doi:10.1017/S0016756810000257.

Vincent, S. J., Morton, A. C., Carter, A., Gibbs, S. and Barabadze, T. G. Oligocene uplift of the Western Greater Caucasus: an effect of initial Arabia-Eurasia collision. *Terra Nova*, 19(2):160–166, 2007. ISSN 0954-4879. doi:10.1111/j.1365-3121.2007.00731.x.

Wagner, G. A. and Reimer, G. M. Fission track tectonics; the tectonic interpretation of fission track apatite ages. *Earth Planet. Sci. Lett.*, 14(2):263–268, 1972.

Wells, A. J. The crush zone of the Iranian Zagros mountains, and its implications. *Geol. Mag.*, 106(5):385–394, 1969.

Westaway, R. Present-day kinematics of the Middle-East and eastern Mediterranean. *J. Geophys. Res.*, 99(B6):12071–12090, 1994. ISSN 0148-0227.

Whipple, K. and Tucker, G. Dynamics of the stream-power river incision model: Implications for height limits of mountain ranges, landscape response timescales, and research needs. *J. Geophys. Res.*, 104(B8):17661–17674, 1999. ISSN 0148-0227.

Willett, S. D. Late Neogene Erosion of the Alps: A Climate Driver? *Annu. Rev. Earth Planet. Sci.*, 38(1):411–437, 2010. doi:10.1146/annurev-earth-040809-152543.

Wobus, C. W., Hodges, K. V. and Whipple, K. X. Has focused denudation sustained active thrusting at the Himalayan topographic front? *Geology*, 31(10):861–864, 2003. doi:10.1130/G19730.1.

Wolf, R., Farley, K. and Silver, L. Helium diffusion and low-temperature thermochronometry of apatite. *Geochim. Cosmochim. Acta*, 60(21):4231–4240, 1996. ISSN 0016-7037.

Yilmaz, Y. New evidence and model on the evolution of the southeast anatolian orogen. *Geol. Soc. Am. Bull*, 105(2):251–271, 1993. ISSN 0016-7606.

Zonenshain, L. P. and Le Pichon, X. Deep basins of the Black Sea and Caspian Sea as remnants of Mesozoic back-arc basins. *Tectonophys.*, 123:181–211, 1986.

CHAPTER III

Collision between the Transcaucasus and Eurasia as a driver of Pliocene reorganization of the Arabia-Eurasia plate boundary

3.1 Abstract

New thermochronometric data from the eastern Greater Caucasus and Talysh mountains in Azerbaijan reveal rapid exhumation from ∼5 Ma to the present. In the northern Greater Caucasus, this rapid exhumation is preceded by slow exhumation initiating at least by early Miocene time, while in the southern Greater Caucasus and Talysh, rapid exhumation is preceded by a sustained period of burial or isothermal holding. The timing of rapid exhumation across the entire extent of the Greater Caucasus orogen coincides with a previously observed tectonic reorganization of the Arabia-Eurasia plate boundary, for which a variety of driving mechanisms have been proposed. Geological observations in eastern Azerbaijan suggest the existence of a marine basin between Eurasia and the Transcaucasus until late Miocene time, deformed remnants of which are now exposed within the Greater Caucasus. We propose that consumption of this basin and resulting collision of the Transcaucasus with Eurasia at ∼5 Ma drove the increase in exhumation rate observed in the Greater Caucasus and Talysh mountains, and marked the onset of "hard" continent-continent collision, one consequence of which was tectonic reorganization of the Arabia-Eurasia

plate boundary.

3.2 Introduction

The southern margin of Eurasia at the longitude of the Greater Caucasus has been subject to numerous accretionary events through Mesozoic and Cenozoic time (e.g. Golonka, 2004), culminating with the collision of the Arabian continent. These accretionary events have created a complex geologic record of upper crustal deformation from which a range of estimates for the timing of the Arabia-Eurasia collision have been inferred (see references in Avdeev and Niemi, 2011). Nonetheless, geologic evidence increasingly points to a late Eocene (∼35 Ma) age for the closure of Neotethys and suturing of Arabia to the southern margin of Eurasia along the Zagros-Bitlis suture (Fig. 3.1; Allen and Armstrong, 2008).

Despite refinements of this timing, outstanding questions regarding the post-collisional dynamics of the Arabia-Eurasia orogen remain. For example, in late Miocene-Pliocene time, the Arabia-Eurasia orogen underwent a major tectonic reorganization as evidenced by the onset of rapid exhumation of the Alborz and Greater Caucasus mountains (Kral and Gurbanov, 1996; Axen et al., 2001; Avdeev and Niemi, 2011), the initiation of presently active faults (Wells, 1969; Westaway, 1994; Jackson et al., 2002; Allen et al., 2004; Copley and Jackson, 2006), changes in provenance of South Caspian sediments (Morton et al., 2003; Allen et al., 2006) and increase in sedimentation and subsidence rate in the South Caspian basin (Allen et al., 2002). Given the wealth of evidence for the pre-Miocene closure of Neotethys (McQuarrie et al., 2003; Allen and Armstrong, 2008; Okay et al., 2010), other driving forces for tectonic reorganization must be considered.

Proposals for the cause of reorganization include the opening of the Red Sea

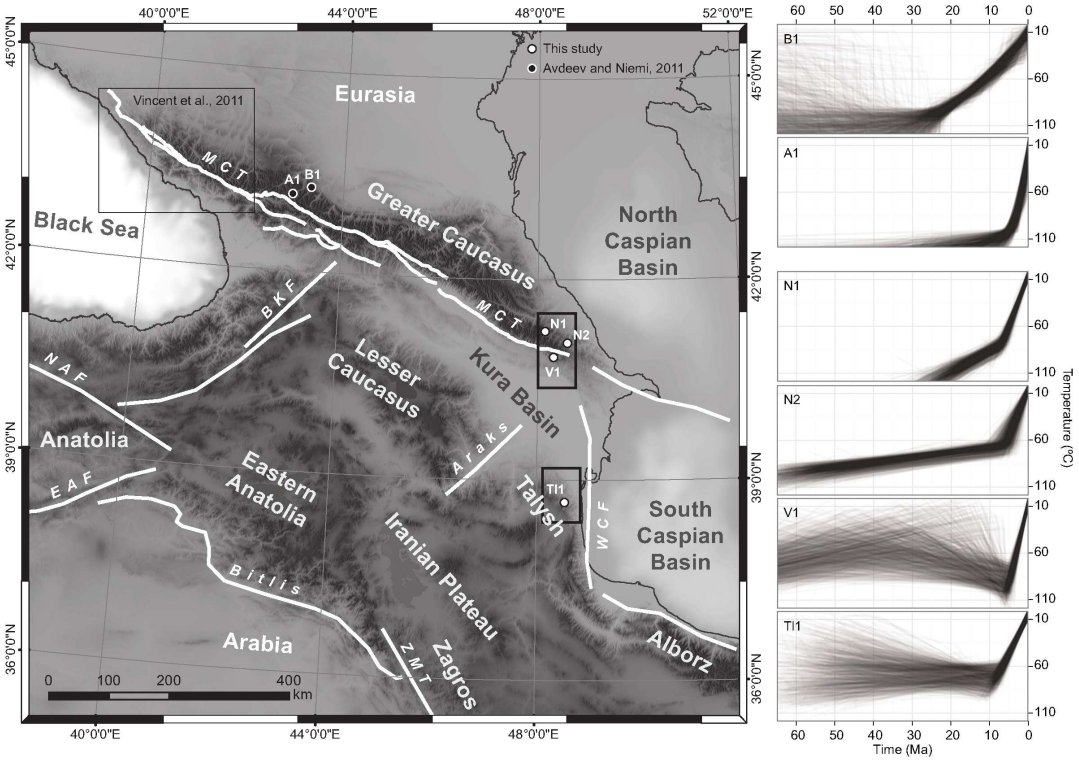

Figure 3.1: Topography of Arabia-Eurasia orogen at the longitude of the Greater Caucasus with locations of detailed maps (Fig. 3.2) and samples for which thermal histories were estimated. **BKF**–Borjomi-Kazbek Fault, **EAF**–East Anatolian Fault, **MCT**–Main Caucasus Thrust, **NAF**–North Anatolian Fault, **WCF**–West Caspian Fault, **ZMT**–Zagros Main Thrust.

(Wells, 1969), over-thickening (or dynamic uplift) of the Iranian Plateau and Greater Caucasus (Allen et al., 2004; Copley and Jackson, 2006) or the closure of ocean basins in Iran (Jackson et al., 2002). Closure of the Greater Caucasus back-arc basin (Zonenshain and Le Pichon, 1986) and collision of the Transcaucasus microplate (the region between the Greater Caucasus and Zagros; Fig. 3.1) with Eurasia remains an alternate mechanism that could explain both rapid exhumation of the Greater Caucasus in Pliocene time (Avdeev and Niemi, 2011) and coincident tectonic reorganization. We explore this mechanism below on the basis of new low-temperature thermochronometric data from the eastern Greater Caucasus and Talysh mountains of Azerbaijan (Fig. 3.1).

3.3 Geological Setting

The Greater Caucasus lie at the northern margin of the Arabia-Eurasia orogen (Fig. 3.1). The main crest of the Greater Caucasus is the elevated edge of the Eurasian platform. Igneous and metamorphic rocks are exposed in the central Greater Caucasus, while at the eastern and western flanks of the range shallow-water marine sedimentary rocks of Jurassic through Late Cretaceous age are preserved. In the eastern Greater Caucasus, these rocks are thrust southward over Oligocene–Miocene deep marine shales (Khain, 2007). The shales are, in turn, thrust over Jurassic to Late Cretaceous volcaniclastic rocks of andesitic composition (Vandam zone, Fig. 3.2; Khain and Shardanov, 1959). Thus, the southern front of the eastern Greater Caucasus presents a marked juxtaposition of Jurassic to Late Cretaceous strata of substantially different origin and lithology (Fig. 3.2).

At its southernmost edge, the Greater Caucasus overthrust the Kura foreland basin (Figs. 1 and 2). The northern margin of the Kura basin is the locus of active

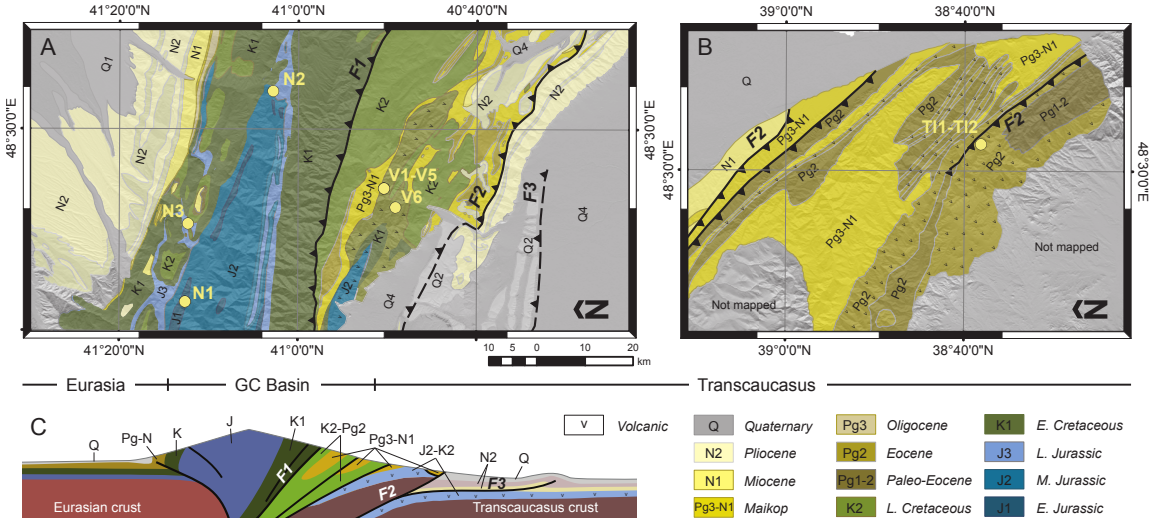

Figure 3.2: Geologic maps of study areas with thermochronometric samples. Locations of progressive deformation fronts (F1–late Eocene, F2–late Miocene, F3–Plio-Pleistocene) shown. Location maps on Figure 3.1. (A) Lagich region, eastern Greater Caucasus. Geology modified after Khain and Shardanov (1959). (B) Talysh Mountains. Geology modified after Mekhtiev and Bairamov (1958). (C) Schematic cross-section through the eastern Greater Caucasus.

deformation within the Greater Caucasus system, and deformation appears to have been focused within the Kura Basin since early Pliocene time (Forte et al., 2010). The oldest rocks in the Kura basin, as constrained by the Saatly well (Shikhalibeylia et al., 1998), are Middle Jurassic andesitic volcanic rocks, similar to those exposed in the Vandam zone and Lesser Caucasus (Kopp and Shcherba, 1985). Overlying these is a thin and incomplete succession of Cretaceous to mid-Miocene marine formations, covered by Pliocene-Quaternary molasse.

The Kura basin is bounded on its southern margin by the Lesser Caucasus west of the Araks fault, and is overthrust by the Talysh mountains to the east of the Araks fault (Figs. 1 and 2). The oldest exposed rocks in the Talysh mountains are Eocene basalts and volcaniclastic rocks, erupted as part of a (failed) intra-arc rift (Adamia et al., 1974; Vincent et al., 2005). The volcanic sequence is overlain by Oligocene–early Miocene marine sedimentary rocks (Vincent et al., 2005).

3.4 Thermochronometric Results

We analyzed three samples from the Greater Caucasus north of the Main Caucasus thrust (labelled "N", Fig. 3.2A), six from the Vandam Zone ("V", Fig. 3.2A), and two from the Talysh mountains ("T"; Fig. 3.2B) using a combination of apatite (U-Th)/He (AHe) and fission-track (AFT), zircon fission-track (ZFT) and feldspar $^{40}Ar/^{39}Ar$ thermochronometry (Table 3.1)[1]. Apatite fission-track data (and (U-Th)/He, where present) were modeled with QTQt (Gallagher et al., 2009) to estimate thermal histories (Fig. 3.1).

Samples N1 and N2 from north of the Main Caucasus thrust (Fig. 3.2A), display similar cooling patterns with slow cooling (2.5 and 0.5°C/My, respectively) prior to 5 Ma and rapid cooling (∼10°C/My) after 5 Ma. Sample N3 (Fig. 3.2A) yields a Cretaceous AHe age. This older age records the thermal signature of mid-Cretaceous erosion, recorded as a regionally extensive unconformity (Khain and Shardanov, 1959). Later stages of exhumation are not recorded by this sample as a consequence of its structural position on the northern periphery of the orogen (Fig. 2A). Thermal modeling of sample V1 from the Vandam zone (Figs. 3.1 and 3.2A) shows either isothermal holding prior to 5 Ma or modest burial beginning at ∼30 Ma. At 5 Ma this sample is exhumed rapidly (∼15°C/My). All Vandam samples show uniformly young AHe ages (Table 3.1) and rapid Plio-Pleistocene cooling (15–35°C/My). Sample T1 from the Talysh (Fig. 3.2B) has a thermal history indicative of isothermal holding prior to 5–10 Ma, followed by fast cooling (8°C/My, Fig. 3.1). All zircon fission-track and $^{40}Ar/^{39}Ar$ ages are interpreted as eruption ages (Table 1).

[1]GSA Data Repository item 2011XXX, Thermochronometric sample localities and analytical data, is available on request from Documents Secretary, GSA, P.O. Box 9140, Boulder, CO 80301, editing@geosociety.org, or at www.geosociety.org/pubs/drpint/htm.

Table 3.1: Summary of the eastern Greater Caucasus low-temperature thermochronometry results

Sample	Longitude (°E)	Latitude (°N)	Elevation (m)	AHe (Ma)[b] (52—73°C)[a]	AFT (Ma)[b] (98—124°C)[a]	ZFT (Ma)[b] (210—350°C)[a]	$^{40}Ar/^{39}Ar$ (Ma)[b] (221—258°C)[a]
V1	48.35381	40.84115	1150	2.8 ± 0.2	88.4 ± 5.7	102.8 ± 4.8	
T2	48.56268	38.63724	1110	2.6 ± 0.4			
T1	48.56385	38.63765	1110	5.9 ± 1.2	50.4 ± 6.7	30.0 ± 1.4	30.1 ± 5.8
N2	48.59255	41.04861	1176		36.1 ± 2.7		
N3	48.26504	41.20685	1550	92.7 ± 11.8			
V2	48.33975	40.838	1101	2.0 ± 0.3			
V3	48.30726	40.81957	1082	4.0 ± 3.0			
V4	48.33487	40.83737	1138	1.7 ± 0.2			
V5	48.34582	40.84113	1098	2.0 ± 0.1			
V6	48.36659	40.84032	1173	1.7 ± 0.2			
N1	48.07184	41.21152	2558	3.3 ± 0.5	14 ± 1.6		

[a] Range of closure temperatures for cooling rates between 1 and 25°C/My.

[b] Standard error of AHe age is calculated from replicate analyses. Standard errors for other methods are estimated analytical errors.

3.5 Comparison with Regional Thermochronometric Data

Thermochronometric results from the "N" suite of samples are similar to published data from structurally comparable positions further west in the Greater Caucasus, and indicate a coherent Cenozoic exhumational history for the Eurasian margin (Fig. 3.1A; Avdeev and Niemi, 2011; Vincent et al., 2011). This history involves slow cooling (<5°C/My) from at least early Miocene until early Pliocene time. Data from the eastern Greater Caucasus do not resolve the initiation of this cooling, but data from the western and central Greater Caucasus (Avdeev and Niemi, 2011; Vincent et al., 2011) indicate that this phase of exhumation began in the late Eocene or early Oligocene, coincident with estimates for the closure of Neotethys (Allen and Armstrong, 2008). Preliminary AFT data from the eastern Greater Caucasus also yield early Miocene ages (Mosar et al., 2010).

Near 5 Ma, most samples in the eastern Greater Caucasus and Talysh mountains record accelerated exhumation at rates of 10–20°C/Ma, consistent with results from the central Greater Caucasus, although samples at the far western end of the range, are already exhumed to depths too shallow to record an increase in exhumation rate at this time (Avdeev and Niemi, 2011).

Thermochronometric data are scarce across the Zagros, Eastern Anatolia, and the Iranian Plateau (Fig. 3.1). However, available studies suggest an early to middle Miocene age for the onset of rapid exhumation just north of the Neotethys suture in the Zagros (Fig. 3.1; Gavillot et al., 2010; Okay et al., 2010), but late Miocene exhumation in the Alborz Mountains (Fig. 3.1; Axen et al., 2001; Guest et al., 2006.

3.6 Implications for Evolution of the Arabia-Eurasia Plate Boundary

Rapid ∼5 Ma exhumation of the Greater Caucasus, Talysh and Alborz coincides with a broader tectonic reorganization of the Arabia-Eurasia orogen (e.g., Copley and Jackson, 2006), but lags exhumation resulting from the closure of Neotethys by at least 10–15 Ma (Gavillot et al., 2010; Okay et al., 2010). Gravitational forces internal to the orogen or post-collisional break-off of the Neotethyan slab have been proposed as drivers of orogenic deformation after the onset of continent-continent collision marked by the closure of Neotethys (Allen et al., 2004; van Hunen and Allen, 2010). Geologic evidence, however, suggests the persistence of a deep marine anoxic basin between Eurasia and the Transcaucasus from Oligocene through middle or late Miocene time (Kopp and Shcherba, 1985; Hudson et al., 2008). Strata deposited in this basin (the Maikop Formation) are now exposed throughout the Greater Caucasus (Fig. 3.2A).

This basin initiated from back-arc rifting between the Transcaucasus and Eurasia in the Mesozoic (Zonenshain and Le Pichon, 1986). The width of this basin is not well constrained, but in the eastern Greater Caucasus, the Maikop Formation records substantial tectonic shortening, and is tectonically juxtaposed against both Eurasian platform strata and volcaniclastic strata of Lesser Caucasus arc affinity (Fig. 3.2A; Khain, 2007).

Evidence for a deep marine basin persisting until perhaps the late Miocene, coupled with our thermochronometric data, suggest that closure of this basin, and thus collision of the Transcaucasus with Eurasia, occurred at ∼5 Ma. Because the Transcaucasus were sutured to Arabia prior to the late Miocene (e.g., Okay et al., 2010), this closure may also mark the final removal of oceanic crust from the

Arabia-Eurasia collision zone at the longitude of the Greater Caucasus, thus initiating "hard" continent-continent collision and driving tectonic reorganization (e.g., Copley and Jackson, 2006).

3.7 Climatic Versus Tectonic Forcing of Greater Caucasus Exhumation

Widespread acceleration of exhumation and erosion throughout the Alpine-Himalaya orogen in Pliocene time has been suggested to be a result of climate change (Molnar, 2004; Willett, 2010). However, such an explanation is unlikely for the Greater Caucasus, where exhumation patterns do not fit predictions of climate-driven exhumation. Samples from the northern Greater Caucasus began exhuming in pre-Pliocene time, in contrast to samples from the southern Greater Caucasus and Talysh (Figs. 3.1 and 3.2) which record isothermal holding until around 5 Ma, when all samples record accelerated cooling. Deformation has encroached further southward into the Kura basin since that time (e.g., Forte et al., 2010), demonstrating southward propagation of thrust fronts (Fig. 3.2A). Such widening of the orogen is unlikely to result from the transition to a more erosive climate, which is expected to cause deformation front retreat and a reduction of orogen size (Willett, 1999). The Pliocene widening and rapid exhumation of the Greater Caucasus instead requires an increase of material influx into the orogenic wedge (Willett, 1999). Such an increase is consistent with the collision of the Transcaucasus continental lithosphere with Eurasia, following the subduction of dense oceanic or transitional crust that underlay the deep marine basin.

3.8 Conclusions

Rapid exhumation of the Greater Caucasus and Talysh mountains coincides with the Pliocene tectonic reorganization of the Arabia-Eurasia collision, but lags ∼10–15

Ma behind exhumation associated with the closure of Neotethys along the Zagros-Bitlis suture. The closure of a deep marine basin at this time, resulting in the collision of the Transcaucasus microplate with Eurasia, explains rapid Pliocene exhumation across the northern margin of the Arabia-Eurasia orogen, and marks the onset of "hard" continent-continent collision within this segment of the plate boundary, thus driving the observed Pliocene tectonic reorganization.

3.9 Acknowledgements

Ken Farley, Chris Hall, Ray Donelick, and Paul O'Sullivan are thanked for assistance with thermochronometric analyses. Ibrahim Murtuzayev provided invaluable assistance with field work in Azerbaijan. This work was funded by Civilian Research and Development Fund (AZG1-2840-BA-06) and National Science Foundation (EAR-0810067) grants to NAN and a Rackham International Student Fellowship from the University of Michigan to BA.

Bibliography

Adamia, S. A., Gamkrelidze, I. P., Zakariadze, G. S. and Lordkipanidze, M. B. Adjara-Trialeti trough and problem of Black Sea origin. *Geotektonika*, 1:74–98, 1974. In Russian.

Allen, M., Jackson, J. and Walker, R. Late Cenozoic reorganization of the Arabia-Eurasia collision and the comparison of short-term and long-term deformation rates. *Tectonics*, 23(2):TC2008, 2004. doi:10.1029/2003TC001530.

Allen, M. B. and Armstrong, H. A. Arabia-Eurasia collision and the forcing of mid-Cenozoic global cooling. *Palaeogeogr. Palaeoclimatol. Palaeoecol.*, 265(1–2):52–58, 2008. doi:10.1016/j.palaeo.2008.04.021.

Allen, M. B., Jones, S., Ismail-Zadeh, A., Simmons, M. and Anderson, L. Onset of subduction as the cause of rapid pliocene-quaternary subsidence in the south caspian basin. *Geology*, 30(9):775–778, 2002. ISSN 0091-7613.

Allen, M. B., Morton, A. C., Fanning, C. M., Ismail-Zadeh, A. J. and Kroonenberg, S. B. Zircon age constraints on sediment provenance in the caspian region. *Journal Of The Geological Society*, 163(Part 4):647–655, 2006. ISSN 0016-7649.

Avdeev, B. and Niemi, N. A. Constraints on the Exhumational History of the Central Greater Caucasus from Low-Temperature Thermochronometry. *Tectonics*, 30:TC2009, 2011. doi:10.1029/2010TC002808.

Axen, G. J., Lam, P. S., Grove, M., Stockli, D. F. and Hassanzadeh, J. Exhumation of the west-central alborz mountains, iran, caspian subsidence, and collision-related tectonics. *Geology*, 29(6):559–562, 2001.

Copley, A. and Jackson, J. Active tectonics of the Turkish-Iranian plateau. *Tectonics*, 25(6):1–19, 2006.

Forte, A., Cowgill, E., Bernardin, T., Kreylos, O. and Hamann, B. Late Cenozoic deformation of the Kura fold-thrust belt, southern Greater Caucasus. *Geol. Soc. Am. Bull*, 122(3/4):465–486, 2010.

Gallagher, K., Charvin, K., Nielsen, S., Sambridge, M. and Stephenson, J. Markov chain Monte Carlo (MCMC) sampling methods to determine optimal models, model resolution and model choice for Earth Science problems. *Mar. Pet. Geol.*, 26:525–535, 2009.

Gavillot, Y., Axen, G. J., Stockli, D. F., Horton, B. K. and Fakhari, M. D. Tim-

ing of thrust activity in the High Zagros fold-thrust belt, Iran, from (U-Th)/He thermochronometry. *Tectonics*, 29:TC4025, 2010.

Golonka, J. Plate tectonic evolution of the southern margin of eurasia in the mesozoic and cenozoic. *Tectonophys.*, 381:235–273, 2004.

Guest, B., Stockli, D. F., Grove, M., Axen, G. J., Lam, P. S. and Hassanzadeh, J. Thermal histories from the central Alborz mountains, northern Iran: Implications for the spatial and temporal distribution of deformation in northern Iran. *Geol. Soc. Am. Bull*, 118(11-12):1507–1521, 2006. ISSN 0016-7606. doi:10.1130/B25819.1.

Hudson, S. M., Johnson, C. L., Efendiyeva, M. A., Rowe, H. D., Feyzullayev, A. A. and Aliyev, C. S. Stratigraphy and geochemical characterization of the Oligocene-Miocene Maikop Series; implications for the paleogeography of eastern Azerbaijan. *Tectonophysics*, 451:40–55, 2008.

Jackson, J., Priestley, K., Allen, M. and Berberian, M. Active tectonics of the South Caspian basin. *Geophys. J. Int.*, 148(2):214–245, 2002. ISSN 0956-540X.

Khain, V. E. Mesozoic-Cenozoic accretionary complexes of the Greater Caucasus. *Doklady Earth Sciences*, 413A(3):376–379, 2007.

Khain, V. E. and Shardanov, A. N. Caucasus Series K-39-XXV. In *State Geological Map 1:200000*. Russian Geological Research Institute (VSEGEI), 1 edition, 1959. 1:200000.

Kopp, M. L. and Shcherba, I. G. Late Alpine development of the east Caucasus. *Geotectonics*, 19(6):497–507, 1985.

Kral, J. and Gurbanov, A. Apatite fission track data from the Great Caucasus pre-Alpine basement. *Chem. Erde*, 56:177–192, 1996.

McQuarrie, N., Stock, J. M., Verdel, C. and Wernicke, B. P. Cenozoic evolution of Neotethys and implications for the causes of plate motions. *Geophys. Res. Lett.*, 30(20):2036, 2003. doi:10.1029/2003GL017992.

Mekhtiev, S. F. and Bairamov, A. S. Caucasus Series J-39-VII. In *State Geological Map 1:200000*. Russian Geological Research Institute (VSEGEI), 1 edition, 1958. 1:200000.

Molnar, P. Late cenozoic increase in accumulation rates of terrestrial sediment: How might climate change have affected erosion rates? *Annu. Rev. Earth Planet. Sci.*, 32:67–89, 2004. ISSN 0084-6597. doi:10.1146/annurev.earth.32.091003.143456.

Morton, A., Allen, M., Simmons, M., Spathopoulos, F., Still, J., Hinds, D., Ismail-Zadeh, A. and Kroonenberg, S. Provenance patterns in a neotectonic basin: Pliocene and Quaternary sediment supply to the South Caspian. *Basin Res.*, 15(3):321–337, 2003. ISSN 0950-091X.

Mosar, J., Kangarli, T., Bochud, M., Glasmacher, U. A., Rast, A., Brunet, M.-F. and Sosson, M. Cenozoic-Recent tectonics and uplift in the Greater Caucasus; a perspective from Azerbaijan. *Geological Society Special Publications*, 340:261–280, 2010.

Okay, A. I., Zattin, M. and Cavazza, W. Apatite fission-track data for the Miocene Arabia-Eurasia collision. *Geology*, 38(1):35, 2010. doi:10.1130/G30234.1.

Shikhalibeylia, E. S., Abdullayev, R. N. and Ali-Zade, A. A. Geological Results from the Saatly superdeep drillhole. *International Geology Review*, 30:1272–1277, 1998.

van Hunen, J. and Allen, M. B. Continental collision and slab break-off: A compari-

son of 3-D numerical models with observations. *Earth Planet. Sci. Lett.*, 302:27–37, 2010.

Vincent, S. J., Allen, M. B., Ismail-Zadeh, A. D., Flecker, R., Foland, K. A. and Simmons, M. D. Insights from the Talysh of Azerbaijan into the Paleogene evolution of the South Caspian region. *Geol. Soc. Am. Bull*, 117(11-12):1513–1533, 2005. ISSN 0016-7606. doi:10.1130/B25690.1.

Vincent, S. J., Carter, A., Lavrishchev, V. A., Price, S. P., Barabadze, T. G. and Hovius, N. The exhumation of the western Greater Caucasus: a thermochronometric study. *Geol. Mag.*, pages 1–21, 2011. doi:10.1017/S0016756810000257.

Wells, A. J. The crush zone of the Iranian Zagros mountains, and its implications. *Geol. Mag.*, 106(5):385–394, 1969.

Westaway, R. Present-day kinematics of the Middle-East and eastern Mediterranean. *J. Geophys. Res.*, 99(B6):12071–12090, 1994. ISSN 0148-0227.

Willett, S. D. Orogeny and orography: The effects of erosion on the structure of mountain belts. *J. Geophys. Res.*, 104(B12):28957–28981, 1999. ISSN 0148-0227.

Willett, S. D. Late Neogene Erosion of the Alps: A Climate Driver? *Annu. Rev. Earth Planet. Sci.*, 38(1):411–437, 2010. doi:10.1146/annurev-earth-040809-152543.

Zonenshain, L. P. and Le Pichon, X. Deep basins of the Black Sea and Caspian Sea as remnants of Mesozoic back-arc basins. *Tectonophys.*, 123:181–211, 1986.

CHAPTER IV

All quiet on the western front? Resolving the paradox of high mountains and low rates of active deformation in the Greater Caucasus

4.1 Abstract

In this paper we address the paradox of low active tectonic rates and high long-term (Ma) exhumation rates in the western Greater Caucasus. We use new and published low-temperature thermochronometric data and a thermokinematic model to estimate rates and kinematics of exhumation in the western Greater Caucasus. Our results show that a single thrust slipping at 4 mm/y active for the last 4 My can explain both the observed thermochronometric data and the modern geodetic convergence rate across the western Greater Caucasus. Thus, high elevations and deep exhumation levels observed in the western Greater Caucasus are the result of focused shortening occurring on a singular Main Caucasus Fault. This differs from the deformation style of the eastern Greater Caucasus, where a larger amount of shortening is distributed across the width of the range with slip occurring on numerous north and south-verging thrusts, resulting in lower uplift rates, lower relief, and lower exhumation. We hypothesize that this difference in tectonic styles is a result of the differences in lithosphere of the eastern and western Transcaucasus. On the west, the Greater Caucasus are juxtaposed against the ancient strong and

buoyant Dzirula microcontinent, while on the east, they are faulted against a Jurassic island arc that is likely to have a thinner, less competent lithosphere.

4.2 Introduction

Comparing long-term exhumation rates and elevations with modern tectonic activity recorded in geodetic displacement fields and the amount of released seismic energy along the Greater Caucasus one might notice a counterintuitive relationship: high elevations and high rates of exhumations in the western Caucasus are associated with low seismicity and low active shortening, while lower elevation and lower exhumation levels of the eastern Caucasus are associated with higher seismicity and higher active shortening (Fig. 4.1 and 4.2).

One possible explanation to this apparent dichotomy is that the convergence in the western Greater Caucasus, driven by Arabia-Eurasia collision, has progressively decelerated over time, and the orogen is currently in a destructive stage. While there is no significant deceleration of the Arabian convergence (McQuarrie et al., 2003), this is a plausible explanation, considering that the onset of rapid exhumation at 5 Ma is attributed to the local collision between the Transcaucasus and Eurasia (Avdeev and Niemi, 2011a,b), and it is reasonable to expect a gradual slow-down of the Transcaucasus convergence following this collision.

Alternatively, the uplift in the Caucasus could be unrelated to Plio-Pleistocene convergence. Ershov et al. (2003) propose a root drop of the the Greater Caucasus lithosphere, which was overthickened during the Oligocene and Miocene, as the cause of post-Miocene exhumation. In this paper we explore these possibilities using a thermokinematic model constrained by previously published and new thermochronometric data, as well as seismic and geodetic observations.

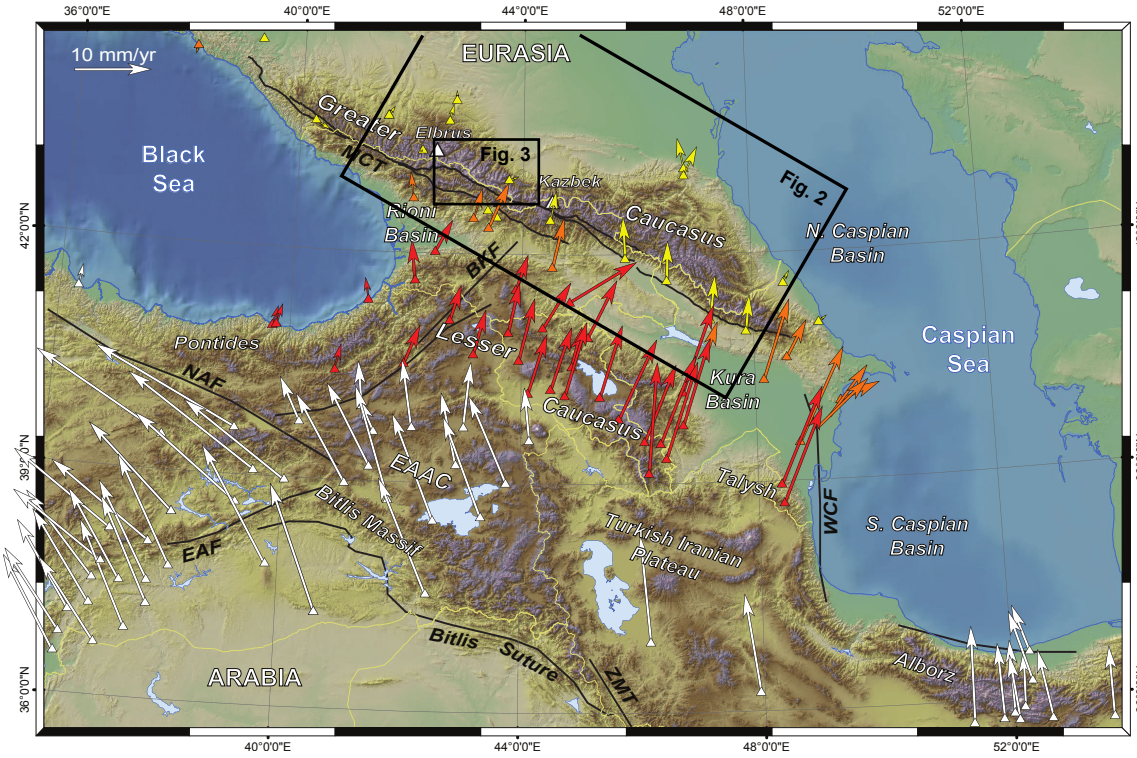

Figure 4.1: Shaded topography of the central Periarabian orogen with the major tectonic elements labeled (after Avdeev and Niemi, 2011a). **NAF**–North Anatolian Fault; **EAF**—East Anatolian Fault; **EAAC**—East Anatolian Accretionary Complex; **BKF**—Borjomi-Kazbek Fault; **MCT**—Main Caucasus Thrust; **ZMT**—Zagros Main Thrust; **WCF**—West Caspian Fault. Vectors show GPS velocities relative to Eurasia (Reilinger et al. (2006); Kadirov et al. (2008)) color-coded by region (yellow–Greater Caucasus; orange–Rioni and Kura basins; red–Lesser Caucasus; white–other regions). Boxes show the swath extent used in Fig. 4.2, and the extent of Fig. 3.

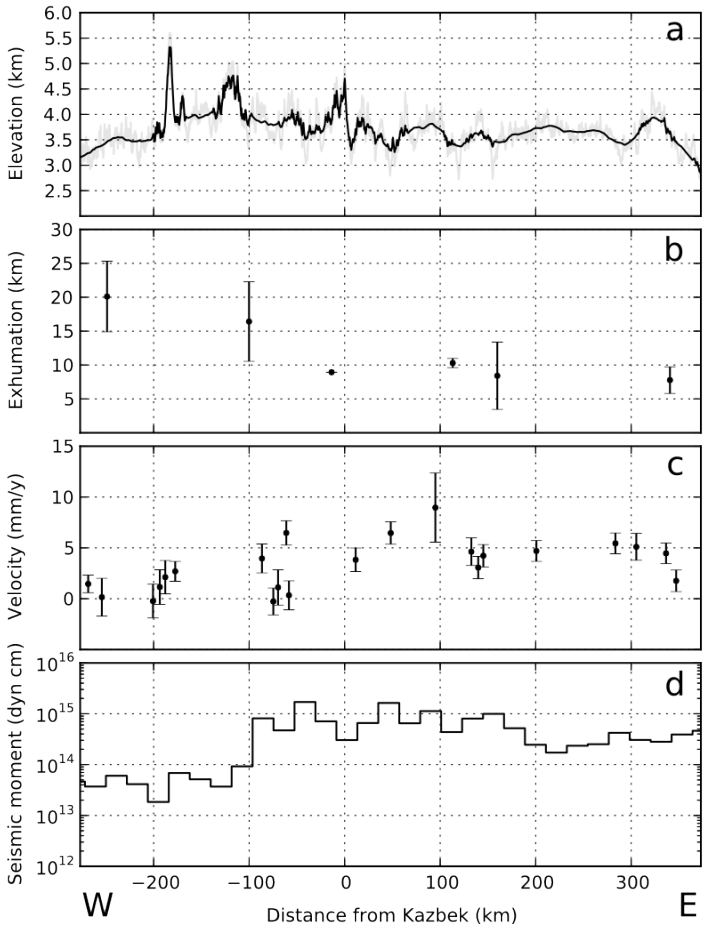

Figure 4.2: Profiles along the Greater Caucasus (120° azimuth) displaying smoothed maximum elevations (a), exhumation level (b), profile-perpendicular GPS velocity (c), and binned estimates of seismic moment release since 1973 (d), data from the NEIC catalog

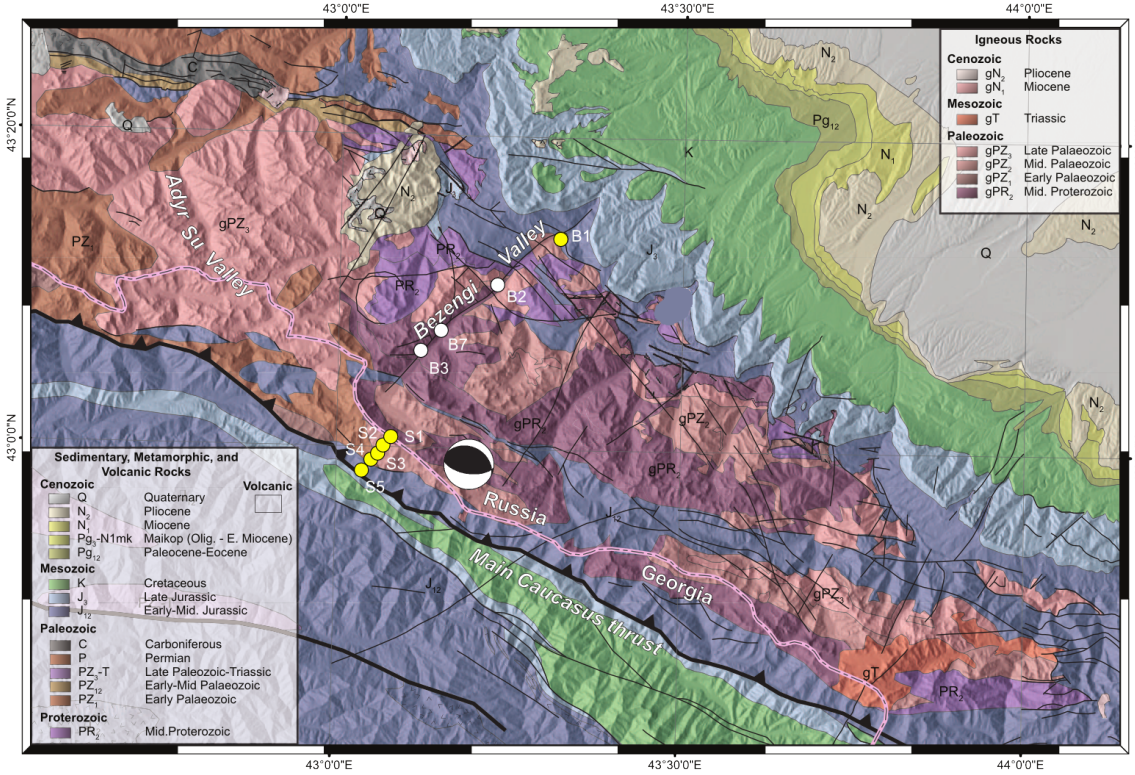

Figure 4.3: Geologic map of the study area with the sample localities (circles). Yellow circles indicate samples used in the thermokinematic model. Beachball shows the location and focal mechanism of the 5.6 (Mw) earthquake (focal depth 8 ± 2 km, Tan and Taymaz, 2006)

4.3 Study area

We focus on a 40 km long SSW-NNE transect across the western Greater Caucasus starting north of the village of Ushguli in Georgia, up Mt. Shkhara, into Russia, through Bezengi valley, to the village of Bezengi (Fig. 4.3). The south end of this transect starts just south of the Main Caucasus thrust (MCT), the major structure separating mostly pre-Mesozoic metamorphic rocks of the European crust from the Mesozoic shales of the Greater Caucasus back-arc basin (e.g. Kopp and Shcherba, 1998).

North of the MCT, the transect climbs up Mt. Shkhara (5200 m) and then descends into the heavily glaciated Bezengi valley. Throughout the northern end, the transect lies within the metamorphic core of the Greater Caucasus—the uplifted edge of Eurasia. The transect ends at the base of the Early to Middle Jurassic continental margin and shelf sediments.

The first order structure along this transect is defined by thrusting of the Transcaucasus underneath Eurasia (e.g. Philip et al., 1989). Timing of this deformation, however, is not well constrained and the local mapped geology only requires that the last deformation happened sometime in the Cenozoic. Published thermochronometric data from the northern part of the transect elucidate the onset of exhumation around 5 Ma (Kral and Gurbanov, 1996; Avdeev and Niemi, 2011a), however this exhumation does not have to be related to the thrusting, and has been interpreted as a result of an isostatic uplift following drop of a dense lithospheric root (Ershov et al., 2003).

One possible hint of neotectonic activity on the MCT is its coincidence with a major physiographic transition from gentle foothills of Svanetia on the south, to the

Table 4.1: Summary of thermochronometric ages along the Bezengi-Shkhara transect

Sample	Age Ma	SE Ma	Method	Altitude m	Longitude °E	Latitude °N
B1	16.81	3.36	AHe	1357	43.320785	43.226316
B1	21.8	1.1	AFT	1357	43.320785	43.226316
B1	188.5	3.87	ZHe	1357	43.320785	43.226316
B1	250	1.2	FAr	1357	43.320785	43.226316
B1	293.4	12.4	ZFT	1357	43.320785	43.226316
B3	7.64	0.52	AFT	2470	43.114502	43.087557
B3	12.16	1.11	AHe	2470	43.114502	43.087557
B7	3.1	0.3	AFT	2536	43.132858	43.097950
B2	3.64	0.35	AFT	1687	43.217135	43.163385
B2	4.06	0.4	AHe	1687	43.217135	43.163385
S5	2.12	0.6	AFT	2609	43.095288	42.967167
S1	7.44	0.65	AFT	5200	43.112273	43.000642
S2	3.35	0.28	AFT	4477	43.105547	42.993354
S3	2.48	0.2	AFT	3760	43.103644	42.988193
S4	1.93	0.26	AFT	3038	43.099585	42.980521

rugged terrain of the Main Caucasus Range on the north (Fig. 4.3). In the Himalaya a similar geomorphic transition is caused by a subsurface ramp (e.g. Avouac, 2007; Herman et al., 2010), but such a configuration is precluded here because of an absence of a frontal thrust south of the MCT. However, this transition can also result from the competence contrast of rocks on opposite sides of the MCT, in which case it may bear little on neotectonic activity.

Other possible evidence for active faulting on the MCT is a recent 5.6 (Mw) earthquake (Tan and Taymaz, 2006). It occurred at a depth of 8 ± 2 km, about 10 km north of the MCT, as a result of slip on a thrust dipping $\sim 30°$ due NNE. Such parameters suggest that this earthquake is likely related to the MCT. Apart from this event, however, no other significant (>4 Mw) earthquakes are recorded within the study area (Fig. 4.2b; Tan and Taymaz, 2006).

4.4 Themochronometric data

In addition to the previously published apatite (U-Th)/He (AHe) and apatite fission-track (AFT) analyses from the Bezengi valley (Avdeev and Niemi, 2011a), we

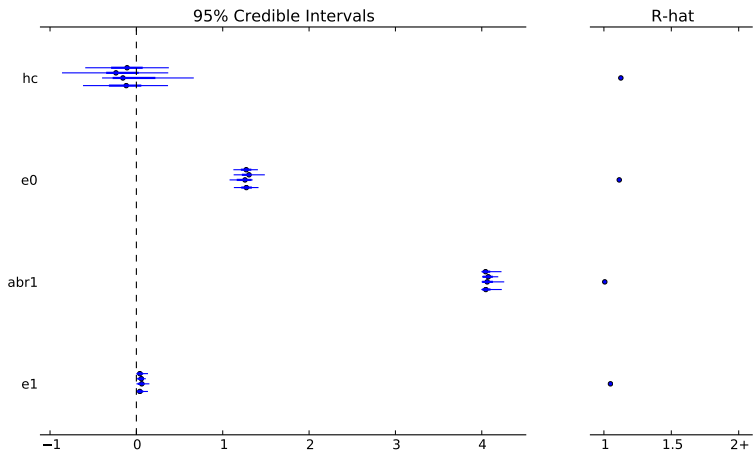

Figure 4.4: Estimates of the parameters of a piece-wise linear age-elevation model (h_c (km) elevation of the closure isotherm, e_0 (km/Ma) recent apparent exhumation rate, a_{br_1} (Ma) age of rate change and e_1 (km/Ma) apparent exhumation rate prior to a_{br_1}) from bedrock and detrital thermochronometric data from the south face of Mt. Shkhara. Results of four independent MCMC runs are plotted to validate convergence of the chains to the same posterior distribution.

collected and analyzed a bedrock AFT transect up the south face of Mt. Shkhara covering ∼3 km of relief, and supplemented it with an AFT detrital sample collected at the toe of the Shkhara glacier. We also analyzed an additional bedrock AFT sample from the Bezengi valley (Fig. 4.3).

A review of the thermochronometric ages (Table 4.1) suggests asymmetric exhumation along our studied transect, with rates of exhumation 1.5–2 times higher on the south, above the MCT, than on the north. Following previously published methodology (Avdeev et al., 2011) we use the Shkhara AFT transect and the detrital sample from the base of Shkhara to estimate an age-elevation relationship, assuming uniform sampling probability and a piece-wise linear parameterization of the age-elevation function with a single break in slope.

Figure 4.4 presents the estimates of the model parameters. Estimate for the break in slope is close to the prior limit of 4 Ma set based on the previous thermochronometric estimates from the northern Caucasus (Avdeev and Niemi, 2011a). Goodness of fit plot (Fig. 4.5), however, does suggest that such prior constraint is in agreement

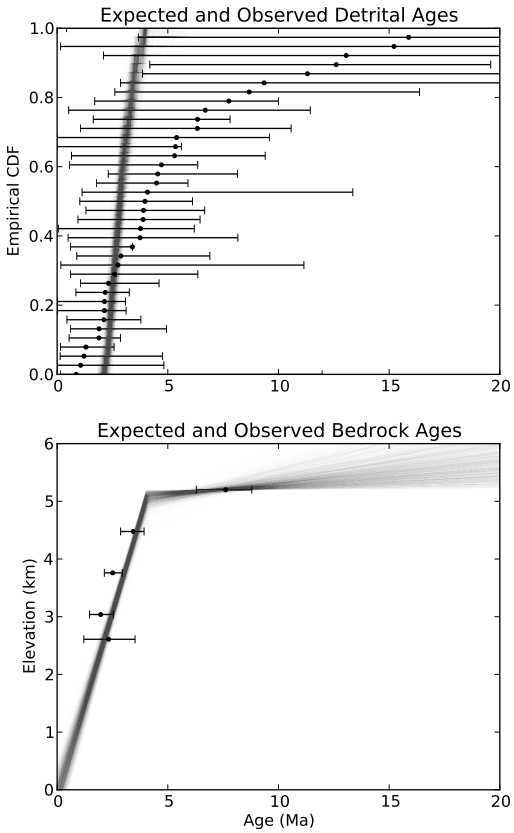

Figure 4.5: Goodness of fit plots for detrital and bedrock data. Circles with error bars show measured ages, while gray lines are the posterior simulations.

with the bedrock data.

Detrital AFT data show poor agreement with the model (Fig. 4.5). There are two possible explanations for this. First, all AFT ages are very young and single grain track counts are very low, making the single grain ages unreliable. Second, as shown by the bedrock data, the age-elevation gradient above 5 km is very high, and the recently eroded rocks that were above our highest sample could easily have ages observed in the detrital sample. Provided that the Shkhara catchment is glaciated and contains numerous moraine deposits, sediment storage is highly probable (e.g. Stock et al., 2006). Given the uncertainty on the single grain AFT ages and the

complication with sediment storage, we exclude the detrital sample from further analysis.

In the Bezengi valley there are three AHe ages and four AFT ages from four samples. One of the samples (BX) has AHe age older than AFT age, which we don't have an explanation for, so it was excluded from the analysis. In addition, we exclude the other two samples from the central part of the valley. This 2–3 km deep valley was incised by a glacier and therefore has likely formed well past the 5 Ma age of collision. In our modeling, however, we have to assume that the shape of topography was preserved throughout the model time. As a result, the model predicted ages will likely be older than the observed ages, since in the model, we cannot currently account for the recent glacial entrenchment and valley-scale exhumation.

4.5 Thermokinematic modeling

While asymmetric distribution of the thermochronometric ages does suggest recent activity on the MCT, it is difficult to directly use the elevation relationship to estimate the exhumation history above a thrust (Stuwë et al., 1994; Mancktelow and Grasemann, 1997). Reasons for this are the effects of non-steady exhumation, bending of isotherms by advection on a dipping fault and evolving topography, unknown kinematics of exhumation. To account for these complexities of the thermal field we use a thermokinematic model Pecube (Braun, 2003) to predict thermal histories for our samples, from which model thermochronometric ages can be computed and compared to the observed ages.

4.5.1 Model setup

We use Pecube-D fork of Pecube (Whipp et al., 2009) that includes an updated AHe age prediction model and allows for a listric fault geometry. We choose this

geometry as it matches the first-order structure of the western Greater Caucasus (Philip et al., 1989) and is parameterized by only two scalars: fault dip at the surface (**di**) and the asymptotic depth (**de**), where the fault becomes horizontal. The shape of the fault is then found by fitting an exponential function to these values.

Overthrusting history on this fault is parameterized by three values: ancient overthrusting rate (**r1**), recent overthrusting rate (**r2**), and the age of the rate change (**ca**), associated with the timing of the Transcaucasus-Eurasia collision.

Pecube does not predict landscape evolution and requires a preassigned topography. The amplitude of the topography can, however, change during the model run. Previous studies suggest that prior to the acceleration of exhumation, the Greater Caucasus were not a significant topographic feature (Avdeev and Niemi, 2011a). Therefore we arbitrarily set the topography to $1/10^{th}$ of the modern topography prior to **ca**, and let it linearly grow reaching the modern elevation some time (**td**) after the collision.

The base of the model is set to 40 km with the temperature at the base **tb**. Thermal conductivity and heat production within the model are parameterized as **cd** and **hp**.

4.5.2 Inverse approach

Altogether, out thermokinematic model for the western Greater Caucasus is parameterized by nine scalars. Varying values of the parameters it is possible to find a maximum likelihood estimate that provides a best fit to the thermochronometric and seismic data. Such an approach, however, does not allow for an easy estimation of the uncertainty of the parameters. Neighborhood algorithm (Sambridge, 1999) has been used with Pecube (e.g. Herman et al., 2010) and allows characterization of uncertainty. In this study we use an Adaptive Metropolis algorithm (Haario et al.,

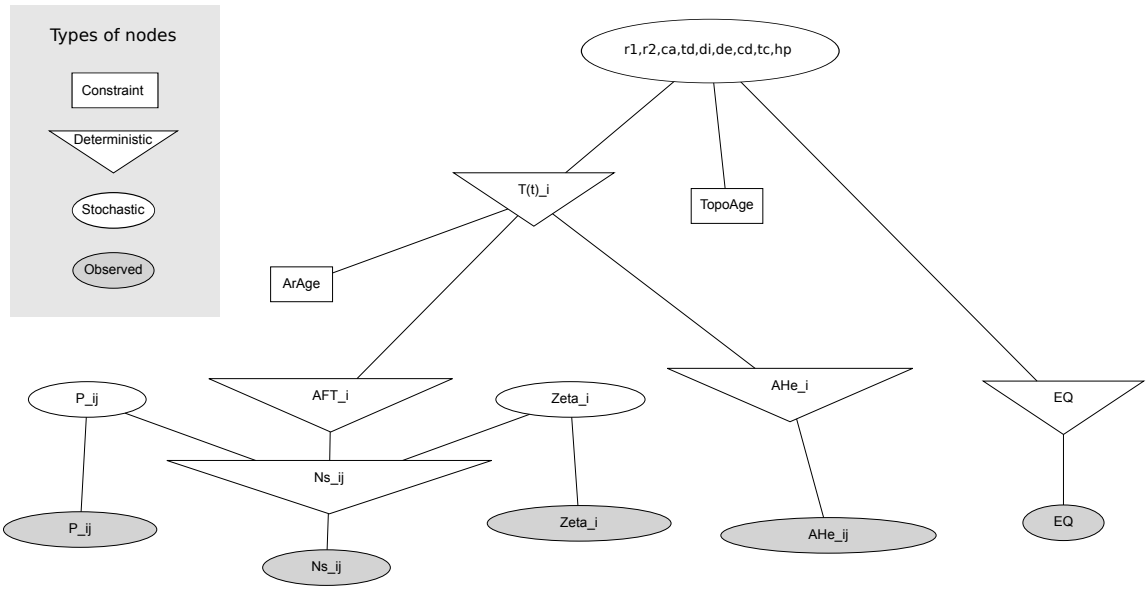

Figure 4.6: Graph of the model and data used in inversion. See text for details.

2001) implemented in PyMC Python package (Patil et al., 2010).

This algorithm is a development of the Metropolis-Hastings algorithm (Hastings, 1970) better suited for sampling from multidimensional distributions with a correlation structure. Unlike the Metropolis-Hastings algorithm, which samples parameters independently, Adaptive Metropolis algorithm updates parameters simultaneously by using a multidimensional proposal distribution. The shape of this proposal is updated in the runtime to match the posterior distribution being estimated. As a result, this algorithm is more efficient than the traditional Metropolis-Hastings algorithm when some of the parameters are correlated.

Figure 4.6 schematically represents the inverse model setup. From the thermokinematic parameters, thermal histories for the sample localities are calculated (subscript i iterates over all samples). Growth rate of the topography is constrained to be not greater than the overthrusting rate **r2** (*TopoAge* constraint). Thermal histories are constrained below 200°C, as there are no known Cenozoic K/Ar or Ar^{40}/Ar^{39} ages

anywhere in the crystalline core of the Gretater Caucasus (Somin, 2007). These thermal histories are used to compute model AHe and AFT ages. Observed AHe ages are modeled using Normal distributions with means equal to the model ages and standard deviation of 15% of the model ages, according to the average spread in replicate AHe analyses from the Greater Caucasus (Avdeev and Niemi, 2011a). From this relationship, likelihood of parameters given the observed AHe ages are computed. From the model AFT ages, given the measured (and uncertain) values of effective uranium concentration P and ζ calibration factor (Donelick et al., 2005), as well as grain sizes, model spontaneous track counts N_s are predicted for each grain in each sample. Observed N_s are modeled using a Poisson distribution (Galbraith, 1981). Finally, model kinematics are used to find the expected depth and focal mechanism of a model earthquake at the location of the recorded 1991 earthquake. The observed earthquake dip and depth are modeled using Normal distributions with the model means and standard deviations estimated by Tan and Taymaz (2006).

4.5.3 Results

The Adaptive Metropolis algorithm was run to produce 50K posterior samples. The non-stationary first half of the chain was discarded and the rest of the posterior sample was thinned to reduce autocorrelation (Gelman et al., 2004). The resultant posterior sample is shown as time series and histograms (Fig. 4.7). Fig. 4.8 shows correlation between all pairs of the parameters, as well as the effect of prior constraints by means of axes limits.

Postcollisional exhumation rate is well resolved, and essentially unaffected by prior constrains. Collision age estimate, however, is clipped by the 4 Ma prior bound, but the acceptable model fit (Fig. 4.9) suggests that the prior constraint, based on previous research (Kral and Gurbanov, 1996; Avdeev and Niemi, 2011a) is in

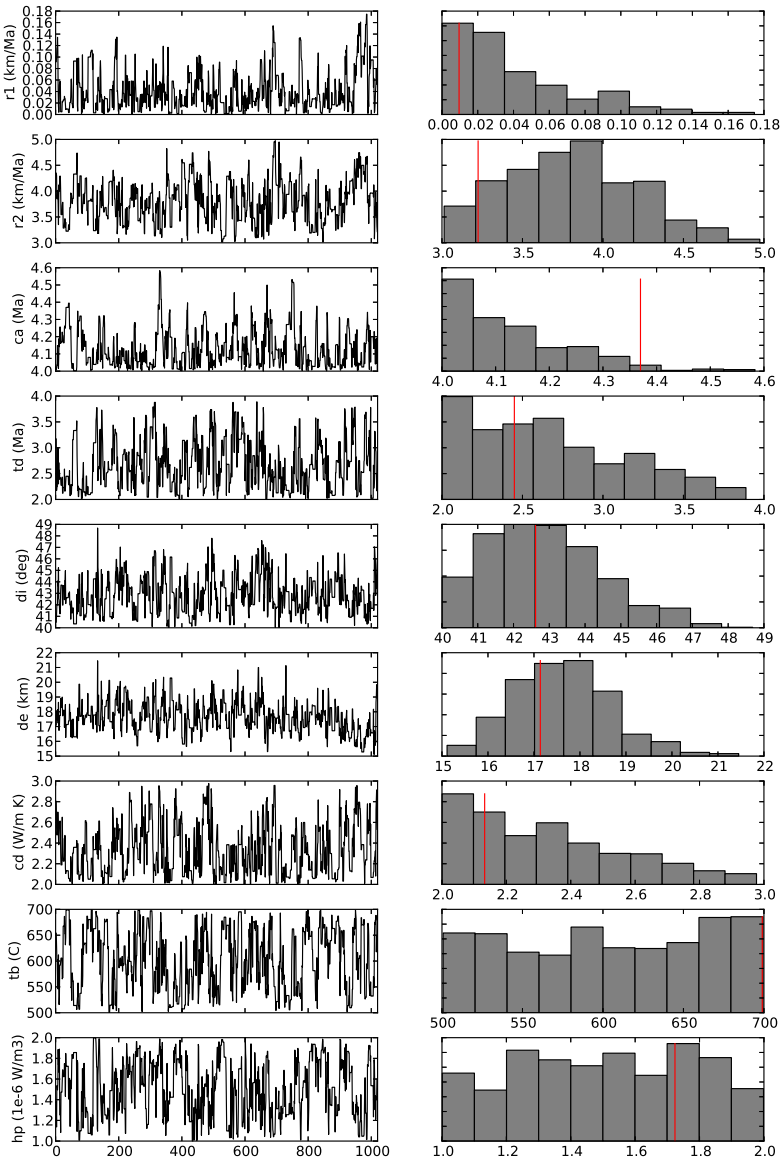

Figure 4.7: Traces (left) and histograms (right) of posterior samples of the thermokinematic parameters. Trace plot has the Markov chain sample number long the x-axis. Red lines show the maximum *a posteriori* estimate.

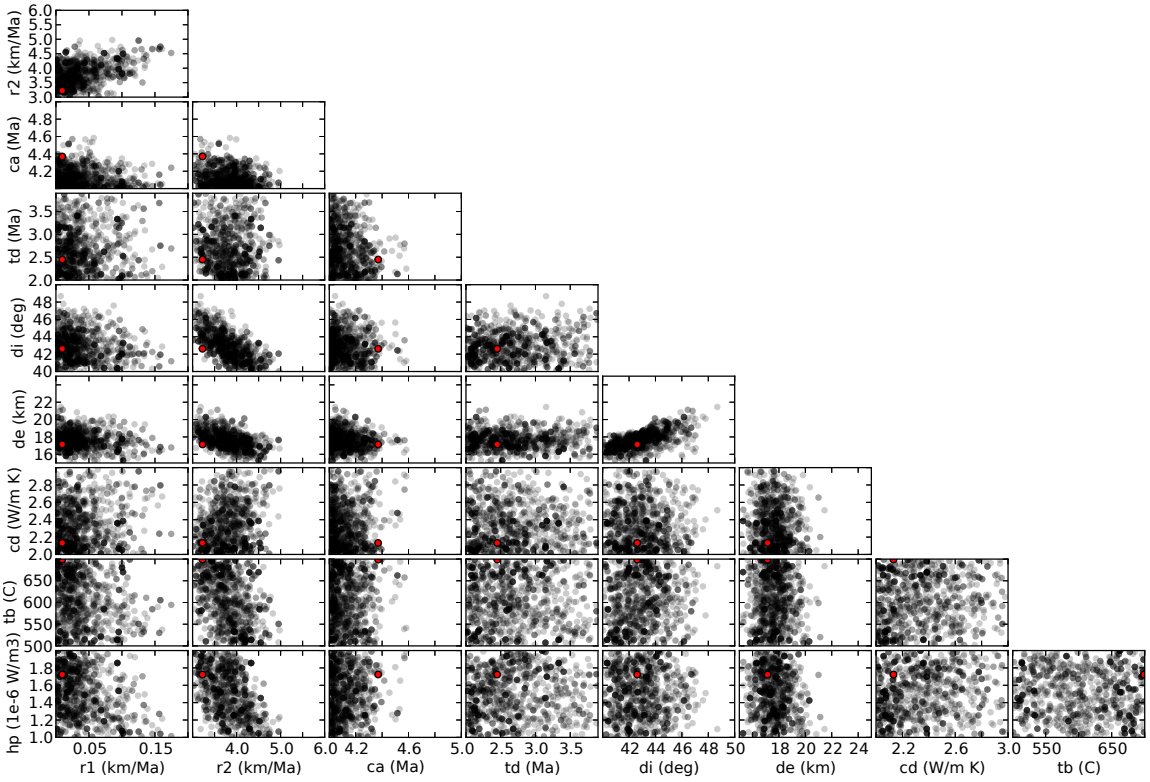

Figure 4.8: Plot of thermokinematic parameter corellations. Limits of the axes are defined by limits of priors of the parameters. Red circles show the maximum *a posteriori* estimate.

agreement with the data used in this paper.

Duration of topographic growth is poorly resolved to "faster, rather than slower". Fault parameters are well resolved and almost unaffected by the priors. Finally, thermal parameters are not well resolved within the priors.

Figure 4.9 shows the posterior estimates of the fault geometry, as well as expected AHe and AFT ages, against the observed earthquake and the observed ages. The model fits well with the data that was used to estimate the model. Some of the omitted thermochronometric ages from the central part of the Bezengi valley are, as expected, younger than the model estimates. Others fit the model estimate. AHe age from the sample B4 is older than expected from the model, however, it is also older than the AFT age, that is difficult to explain, given its relatively low eU concentration (Shuster et al., 2006).

4.6 Discussion

Our estimate for the overthrusting rate of 3.0–4.5 km/Ma over the last 4 Ma is in a good agreement with the geodetic convergence rate of 3–5 mm/a between the western Transcaucasus (sites within the Rioni basin) and Eurasia (Figs. 4.1, 4.2c and 4.10). This suggests that if most of the convergence between the western Transcaucasus and Eurasia is accommodated by overthrusting (i.e. exhumation of the hanging wall), then the observed active rates of convergence are sufficient to explain high elevations and fast long-term exhumation of the western Greater Caucasus.

Further comparing geodetic displacement rates predicted by an elastic half-space model (Okada, 1985) for a 30° north-dipping fault locked at 20 km and slipping at a rate of 4.5 mm/a (upper bound of the thermokinematic estimate) show that there might be some excess of the geodetic convergence that could be accommodated either

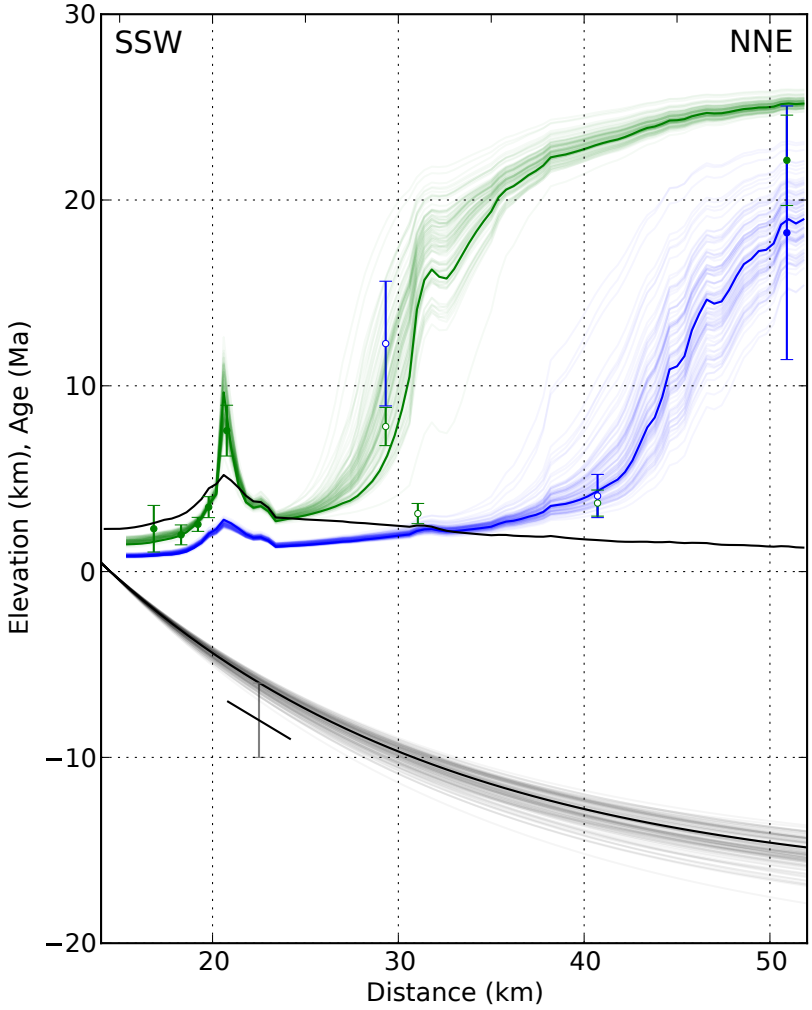

Figure 4.9: Posterior estimate of the fault geometry (black lines) and AFT (green lines) and AHe (blue lines) ages at the surface (black line) predicted from the model and the data used to fit the model: AFT and AHe ages (filled green and blue circles with error bars), and the location and dip of the Shkhara earthquake (black dash with error bars). Hollow green and blue circles with error bars show the AFT and AHe ages excluded from the model. Maximum *a posteriori* estimates are emphasized with bold lines.

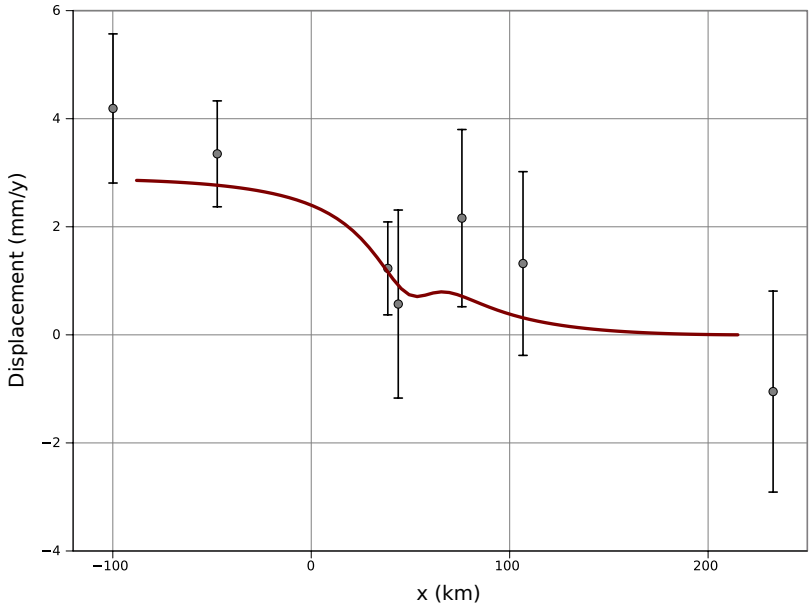

Figure 4.10: North component of the observed GPS displacement rates (Reilinger et al., 2006) for the stations in the vicinity of the Shkhara-Bezengi transect (circles with error bars) and the predicted GPS displacement resulting from a 4 mm/a slip on a fault dipping 30° due south locked at depth of 20 km. X-axis is the distance along the Shkhara-Bezengi transect.

through underthrusting of the Transcaucasus, or by the deformation in the foreland of the MCT (e.g. Triep et al., 1995). Our results do not eliminate the possibility of higher convergence rates in the past that could be accommodated either through underthrusting, or on structures south of the MCT, that may be evidenced by young cooling ages from Lower Svanetia (Vincent et al., 2011).

Our model does not explain some data from the central part of the Bezengi valley. As mentioned above, this misfit might result from the specific landscape evolution of the area that is not accounted for in the model. This part of the transect lies deep in glacial through, that has probably developed later than the Greater Caucasus range, with the onset of Pleistocene glaciation. Alternatively, these anomalously young ages could result from thrusting within the Caucasus core. A better model that could address this misfit would require additional data.

It is unlikely that the estimated fault kinematics can be extrapolated further

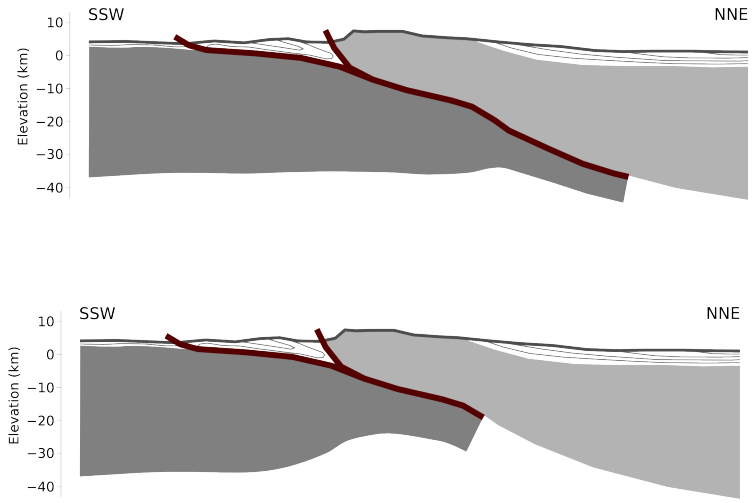

Figure 4.11: Two models for the crustal structure underneath the western Greater Caucasus. (a) Continental crust of the Transcaucasus underthrust Eurasia ∼40 km. (b) The Greater Caucasus are underlain by the lithosphere of the Greater Caucasus basin. This scenario does not require high rates of underthrusting since the collision of Transcaucasus and Eurasia 4 Ma or earthquakes below 20 km. No vertical exaggeration.

north, underneath Eurasia. The estimated basal depth of 15–20 km is probably too low for a lithospheric-scale structure. In addition, attitudes of sedimentary rocks on the north end of the transect are expected to be similar to the attitude of the thrust below them, but in fact dip much more steeply (25–30°) than the estimated thrust surface (10–15°). In addition, assuming MCT is a crustal-scale structure, extrapolation of the predicted thrust geometry further north would imply unreasonably thin Eurasian crust (McKenzie and Priestley, 2008). We hypothesize that the dip of the fault may increase at the northern end of the profile.

One possible explanation is that this ramp appears above the northern edge of the Transcaucasus block, that then must have underthrusted approximately 40 km beneath Eurasia since the 4 Ma collision (Fig. 4.11a). Given that our results suggest almost no active underthrusting, the past underthrusting rate must have been extremely high (greater than 10 km/Ma). In addition, this model implies presence

of the Greater Caucasus basin crust underneath Eurasia at depths below 20 km, but no earthquakes that deep are observed in this region (Tan and Taymaz, 2006). Such structure would not affect the low-temperature thermochronometers from the southern part of the transect that were already above the ramp at the time recorded by their thermochronometric age, but could possibly explain the observed young ages observed in the middle part of the Bezengi valley as recording the recent cooling due to exhumation above the northward propagating ramp.

Alternatively, this ramp can occur above the transitional crust of the subducted Greater Caucasus basin (Fig. 4.11b). In this case, no high rates of recent underthrusting or deep earthquakes are needed. If the basin began subducting 30 Ma (Avdeev and Niemi, 2011a), than the rate of underthrusting would need be about 1 km/Ma. In this case, only the northernmost age from the sample B1 could be affected by this process, as the rest of the ages postdate the underthrusting. Capturing the underthrusting of the Greater Caucasus basin slab through time would require higher temperature thermochronometric analyses from the central and southern parts of the transect.

As was pointed out above, active and long-term tectonics of the eastern and western Greater Caucasus have significant differences. After an apparently isochronous onset of rapid exhumation, western Greater Caucasus experienced higher rates of rock uplift, as evidenced by deeper exhumation levels and higher elevations. At the same time, as suggested by our study, shortening in the western Greater Caucasus (at least the component expressed in the exhumation) was persistently low and largely concentrated on the MCT. In the eastern Caucasus, on the other hand, active shortening and seismicity levels are high, but the uplift rates appear to be generally lower and spread out across a wider area, from the Kura basin (Forte et al., 2010)

to Dagestan (Sobornov, 1994).

We interpret this difference as an effect of variation in lithospheric structure within the Transcaucasus. While in the eastern part the Transcaucasus are represented by Jurassic island arc with no evidence for continental crust underneath, the western Transcaucasus are an old continental massif. This continental crust is likely to be competent and buoyant, resulting in little underthrusting and almost no internal deformation, with most of the convergence accommodated by the exhumation of the overriding Eurasian plate.

4.7 Conclusions

Most of the data fits into a simple listric thrust model. This model estimates the overthrusting rate on the MCT to 3.0–4.5 km/My. This rate is in a good agreement with the active rate of shortening. This implies that the the low modern shortening across the western Greater Caucasus is sufficient to produce the inferred high exhumation and rock uplift. We conclude that high uplift in response to low convergence is the result of deformation focused on a singular structure of the MCT, and such focusing is a result of competence of old and cold lithospheres of Dzirula and Eurasia.

Acknowledgements

We would like to acknowledge Eric Cowgill for numerous discussions, Todd Ehlers for providing the Pecube-D code, Dave Whipp and Frederic Herman for assistance with Pecube, Eric Hetland for granting access to an HPC cluster, and Alison Duvall for movie reviews.

Bibliography

Avdeev, B. and Niemi, N. A. Constraints on the Exhumational History of the Central Greater Caucasus from Low-Temperature Thermochronometry. *Tectonics*, 30:TC2009, 2011a. doi:10.1029/2010TC002808.

Avdeev, B. and Niemi, N. A. Late Miocene closure of the Greater Caucasus basin and its effects on the Arabia-Eurasia orogeny. *Geology*, page In review, 2011b. doi:10.1029/2010TC002808.

Avdeev, B., Niemi, N. A. and Clark, M. K. Doing more with less: Bayesian estimation of erosion models with detrital thermochronometric data. *EPSL*, 2011. doi:10.1016/j.epsl.2011.03.020.

Avouac, J.-P. Dynamic processes in extensional and compressional settings - mountain building: From earthquakes to geological deformation. In Schubert, G., editor, *Treatise on Geophysics*, pages 377 – 439. Elsevier, Amsterdam, 2007. ISBN 978-0-44-452748-6. doi:DOI: 10.1016/B978-044452748-6.00112-7.

Braun, J. Pecube: a new finite-element code to solve the 3D heat transport equation including the effects of a time-varying, finite amplitude surface topography. *Comput. Geosci.*, 29:787–794, 2003. ISSN 0098-3004. doi:10.1016/S0098-3004(03)00052-9.

Donelick, R. A., O'Sullivan, P. B. and Ketcham, R. A. Apatite fission-track analysis. In Reiners, P. W. and Ehlers, T. A., editors, *Low-Temperature Thermochronology: Techniques, Interpretations, and Applications*, volume 58, chapter Reviews in Mineralogy & Geochemistry, pages 49–94. Mineralogical Society of America, 2005.

Ershov, A. V., Brunet, M.-F., Nikishin, A. M., Bolotov, S. N., Nazarevich, B. P.

and Korotaev, M. V. Northern Caucasus basin: thermal history and synthesis of subsidence models. *Sediment. Geol.*, 156(1-4):95–118, 2003.

Forte, A., Cowgill, E., Bernardin, T., Kreylos, O. and Hamann, B. Late Cenozoic deformation of the Kura fold-thrust belt, southern Greater Caucasus. *Geol. Soc. Am. Bull*, 122(3/4):465–486, 2010.

Galbraith, R. On statistical-models for fission-track counts. *Journal of the International Association for Mathematical Geology*, 13(6):471–478, 1981. ISSN 0020-5958.

Gelman, A., Carlin, J. B., Stern, H. S. and Rubin, D. B. *Bayesian data analysis*. Chapman & Hall/CRC, 2nd edition, 2004.

Haario, H., Saksman, E. and Johanna, T. An adaptive Metropolis algorithm. *Bernoulli*, 7(2):223, 2001. ISSN 1350-7265.

Hastings, W. K. Monte Carlo sampling methods using Markov chains and their applications. *Biometrika*, 57:97–109, 1970.

Herman, F., Copeland, P., Avouac, J.-P., Bollinger, L., Maheo, G., Le Fort, P., Rai, S., Foster, D., Pecher, A., Stuwe, K. and Henry, P. Exhumation, crustal deformation, and thermal structure of the nepal himalaya derived from the inversion of thermochronological and thermobarometric data and modeling of the topography. *J. Geophys. Res.*, 115:B06407, 2010. ISSN 0148-0227. doi:10.1029/2008JB006126.

Kadirov, F., Mammadov, S., Reilinger, R. and McClusky, S. Some new data on modern tectonic deformation and active faulting in Azerbaijan (according to Global Positioning System measurements). *Proceedings, The Sciences of the Earth, Azerbaijan National Academy of Sciences*, 1:82–88, 2008.

Kopp, M. and Shcherba, I. Caucasian basin in the Paleogene. *Geotectonics*, 32(2):93–113, 1998.

Kral, J. and Gurbanov, A. Apatite fission track data from the Great Caucasus pre-Alpine basement. *Chem. Erde*, 56:177–192, 1996.

Mancktelow, N. and Grasemann, B. Time-dependent effects of heat advection and topography on cooling histories during erosion. *Tectonophysics*, 270(3-4):167–195, 1997.

McKenzie, D. M. and Priestley, K. The influence of lithospheric thickness variations on continental evolution. *Lithos*, 102:1–11, 2008.

McQuarrie, N., Stock, J. M., Verdel, C. and Wernicke, B. P. Cenozoic evolution of Neotethys and implications for the causes of plate motions. *Geophys. Res. Lett.*, 30(20):2036, 2003. doi:10.1029/2003GL017992.

Okada, Y. Surface deformation due to shear and tensile faults in a half-space. *Bull. Seismol. Soc. Am.*, 75:1135–1154, 1985.

Patil, A., Huard, D. and Fonnesbeck, C. PyMC: Bayesian stochastic modelling in Python. *Journal of Statistical Software*, 35:1–81, 2010.

Philip, H., Cisternas, A., Gvishiani, A. and Gorshkov, A. The Caucasus: an actual example of the initial stages of continental collision. *Tectonophys.*, 161(1-2):1–21, 1989.

Reilinger, R., McClusky, S., Vernant, P., Lawrence, S., Ergintav, S., Cakmak, R., Ozener, H., Kadirov, F., Guliev, I., Stepanyan, R., Nadariya, M., Hahubia, G., Mahmoud, S., Sakr, K., ArRajehi, A., Paradissis, D., Al-Aydrus, A., Prilepin, M., Guseva, T., Evren, E., Dmitrotsa, A., Filikov, S. V., Gomez, F., Al-Ghazzi,

R. and Karam, G. GPS constraints on continental deformation in the Africa-Arabia-Eurasia continental collision zone and implications for the dynamics of plate interactions. *J. Geophys. Res.*, 111:B05411, 2006.

Sambridge, M. Geophysical inversion with a neighbourhood algorithm—II. Appraising the ensemble. *Geophysical Journal International*, 138(3):727–746, 1999. ISSN 1365-246X. doi:10.1046/j.1365-246x.1999.00900.x.

Shuster, D. L., Flowers, R. M. and Farley, K. A. The influence of natural radiation damage on helium diffusion kinetics in apatite. *Earth Planet. Sci. Lett.*, 249(3-4):148–161, 2006. ISSN 0012-821X. doi:10.1016/j.epsl.2006.07.028.

Sobornov, K. O. Structure and petroleum potential of the Dagestan thrust belt, northeastern Caucasus, Russia. 42(3), 1994.

Somin, M. L. Main features of structure of pre-Alpine basement of the Greater Caucasus. In Leonov, J. G., editor, *The Greater Caucasus during the Alpine epoch*, pages 15–38. Geos, 2007.

Stock, G. M., Ehlers, T. A. and Farley, K. A. Where does sediment come from? quantifying catchment erosion with detrital apatite (U-Th)/He thermochronometry. *Geology*, 32:725–728, 2006.

Stuwë, K., White, L. and Brown, R. The influence of eroding topography on steady state isotherms. Applications to fission track analysis. *Earth Planet. Sci. Lett.*, 124:63–74, 1994. doi:10.1016/0012-821X(94)00068-9.

Tan, O. and Taymaz, T. Active tectonics of the Caucasus: Earthquake source mechanisms and rupture histories obtained from inversion of teleseismic body waveforms. In Dilek, Y. and Pavlides, S., editors, *Postcollisional Tectonics and Magmatism in*

the Mediterranean Region and Asia, volume 409 of *Geological Society of America Special Papers*, pages 531–578. 2006. ISSN 0072-1077.

Triep, E. G., Abers, G. A., Lernerlam, A. L., Mishatkin, V., Zakharchenko, N. and Starovoit, O. Active thrust front of the Greater Caucasus - the April 29, 1991, Racha earthquake sequence and its tectonic implications. *J. Geophys. Res.*, 100(B3):4011–4033, 1995. ISSN 0148-0227.

Vincent, S. J., Carter, A., Lavrishchev, V. A., Price, S. P., Barabadze, T. G. and Hovius, N. The exhumation of the western Greater Caucasus: a thermochronometric study. *Geol. Mag.*, pages 1–21, 2011. doi:10.1017/S0016756810000257.

Whipp, D. M., Ehlers, T. A., Braun, J. and Spath, C. D. Effects of exhumation kinematics and topographic evolution on detrital thermochronometer data. *J. Geophys. Res.*, 114:F04021, 2009.

CHAPTER V

Bayesian estimation of erosion models with detrital thermochronometric data

5.1 Abstract

Detrital low temperature thermochronometric data provides spatial and temporal information on catchment erosion, which is relevant to problems in climate, tectonics and geomorphology. However, direct inference of erosion rates from such data is not trivial and only the simplest inverse problems have been addressed previously. In this paper, we present a new approach that relies on the Bayesian interpretation of probability and uses a Markov chain Monte Carlo algorithm for inversion, which affords flexibility in the choice of specific model parametrization and transparent assessment of model uncertainty. We demonstrate how a single detrital sample sourced from a high relief catchment can constrain long-term ($> 10^6$ years) changes in erosion rate that are in good agreement with published bedrock age-elevation profiles. Furthermore, we use detrital data to jointly invert for long-term exhumation history and spatial variability in short-term ($< 10^3$ years) sediment supply, information relevant to many geomorphic studies. Where cooling histories are simple, we show that even small sample sizes (< 20 grains) reliably estimate long-term rates of exhumation.

Citation:
Avdeev, B. et al. (2011), Doing more with less: Bayesian estimation of erosion models with detrital thermochronometric data, *EPSL, 305*, 385–395, 10.1016/j.epsl.2011.03.020

We suggest that the presented approach to modeling detrital low-temperature thermochronometric data is both a powerful and efficient tool for solving tectonic and geomorphic problems.

5.2 Introduction

The distribution of single-grain low-temperature thermochronometric (cooling) ages in fluvial sediment depends on three spatially variable characteristics of the catchment: bedrock cooling ages, short-term sediment supply, and bedrock concentrations of detrital grains of interest. While the distribution of bedrock cooling ages defines the potential age spectrum in a detrital sample, spatial variability in erosion rate and bedrock mineral concentration modulate the detrital age distribution through preferential sampling of the catchment surface. Bedrock cooling ages are controlled by exhumation averaged over a longer time scale ($> 10^6$ years) than the erosional processes that modulate sediment supply ($< 10^3$ years). The connection of detrital low-temperature thermochronometric ages with erosion at two distinct timescales is unique, and can potentially be exploited for integrated studies of climate, tectonics and erosion.

The effects of various tectonic and geomorphic factors on detrital thermochronometric age distributions have been studied theoretically (e.g. Whipp et al., 2009), but only in a few cases have detrital samples been used to test, or measure, these effects in nature. Previous applications of detrital data to tectonics have been limited to steady state problems. Average long-term exhumation rates have been derived from the mean cooling age of a suite of detrital ages and depth to the closure isotherm (Brewer et al., 2003) or the range of detrital ages divided by the elevation range sampled (Ruhl and Hodges, 2005). Steady-state thermo-kinematic models have been

tested by predicting detrital age distributions and comparing these predictions with observations (Brewer and Burbank, 2006). Temporal variability in long-term erosion rates, however, is common in regions of active deformation and high relief, and should be recorded in the distribution of cooling ages in a detrital sample.

Detrital ages have also been used as sediment tracers to assess short-term variations in sediment supply where bedrock age distributions within a catchment are known (e.g. Stock et al., 2006; McPhillips and Brandon, 2010). Spatially non-uniform erosion from a catchment in the eastern Sierra Nevada has been demonstrated through comparison of observed detrital ages to a predicted detrital age distribution based on catchment hypsometry, bedrock age distribution and the assumption of uniform erosion (Stock et al., 2006). Spatial variations in erosion rate over two catchments in the western Sierra Nevada have been both demonstrated and quantified using detrital thermochronometric ages as sediment tracers through comparison of the frequency distribution of thermochronometric ages in a detrital sample to the frequency distribution of bedrock ages in the catchment, where mismatches between these two distributions are interpreted as variations in short-term erosion rate (McPhillips and Brandon, 2010).

We build on previous studies by developing a statistical inversion of detrital low-temperature thermochronometric ages for both variations in short-term sediment supply and long-term exhumation rates as constrained by detrital cooling age distributions and catchment hypsometries. We formulate an inverse method using a Bayesian approach, which greatly simplifies the treatment of uncertainties, and a Markov chain Monte Carlo (MCMC) algorithm that provides a powerful computational tool for estimating Bayesian models. A similar methodology has been successfully applied to various geochronologic problems, including the calibration of

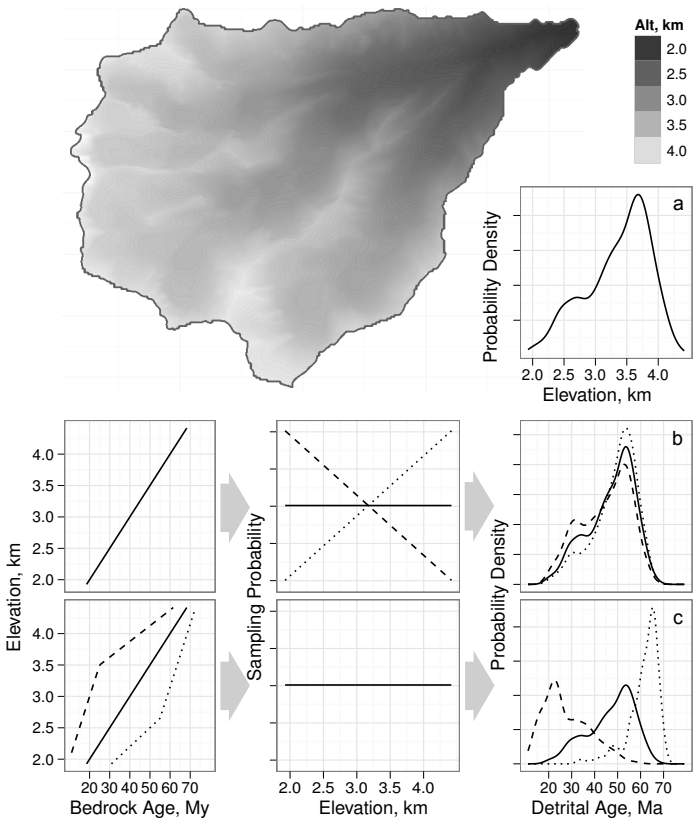

Figure 5.1: Illustration of the effects of (b) nonuniform sampling (p_s in Eq. 5.1) and (c) various age-elevation gradients (described by p_b in Eq. 5.1) on the age distribution in a derital sample derived from a catchment (a).

fission-track annealing models (Stephenson et al., 2006), resolving thermal histories with bedrock cooling ages (Gallagher et al., 2005), and detrital U-Pb age provenance analysis (Jasra et al., 2006), as well as other geological and geophysical problems (e. g. Malinverno, 2002; Sambridge et al., 2006; Leonhardt and Fabian, 2007; Matsu'ura et al., 2007; Hopcroft et al., 2009; Gallagher et al., 2009). We demonstrate the feasibility of this approach through analysis of new and published datasets, and describe its applicability to tectonic and geomorphic studies.

5.3 Detrital thermochronometric age model

Bayesian inversion requires a likelihood function that defines the probability of the observed data given values of the model parameters (B). The probability density

function of observing an age a in a detrital grain, p_d, is an integral of the probability of observing this age in a bedrock sample p_b over a watershed W, weighted by the probability density of sampling a given point of bedrock p_s (i.e., the probability of a detrital grain coming from a point w):

$$p_d(a) = \iint_W p_b(a|w)p_s(w)dw. \tag{5.1}$$

The function p_b represents the long-term exhumation history defining the bedrock cooling ages, while p_s represents the short-term erosion rates and the concentration of the detrital grains in the bedrock, defining the pattern of bedrock sampling. It should be noted that this model differs from the finite mixture model used in detrital U-Pb provenance analysis (e.g. Jasra et al., 2006) in that the number of components p_b in the detrital age distribution p_d in our case is infinite, but these components are constrained by a finite number of exhumation parameters as discussed below.

The probability of observing a thermochronometric age a at the catchment surface (Fig. 5.1) is defined by the bedrock cooling age $\bar{b}$ and the thermochronometric error. If the thermochronometric error is normal, centered at the true age and has standard deviation σ, then

$$p_b(a|w,\theta,\sigma) = \frac{1}{\sqrt{2\pi}\sigma} \exp\left(-\frac{1}{2}\left(\frac{a-\bar{b}(w,\theta)}{\sigma}\right)^2\right). \tag{5.2}$$

The thermochronometric error represents an uncertainty of diffusion and annealing models in measuring bedrock cooling age, as seen in replicate thermochronometric analyses (e. g. House et al., 1997).

The bedrock cooling age, parameterized by θ, depends on the long-term exhumation history of the catchment. In a general case, when the effects of topography and exhumation on the thermal field are non-negligible (e.g. Stuwë et al., 1994), a thermo-kinematic model can be used to compute the surficial distribution of bedrock

cooling ages $\bar{b}(w, \theta)$. Sometimes, however, it is possible to assume a vertical exhumation pathway and a flat closure isotherm. In such a case, the bedrock cooling ages are invariant in the horizontal direction and are only a function of elevation. For example, bedrock ages are commonly described by a linear function of elevation, as in the case of steady-state exhumation. If transient thermal field behavior can be ignored, temporal changes in exhumation rate can be expressed by a piece-wise linear function (i.e. "break in slope" model (Fitzgerald et al., 1995), Fig. 5.1c):

$$\bar{b}(h, \theta^n) = \begin{cases} (h - h_{c_0})/e_0, & \bar{b} < a_{br_1} \\ \vdots & \\ (h - h_{c_n})/e_n, & \bar{b} > a_{br_n} \end{cases}, \tag{5.3}$$

where n is the number of breaks, e_i is the slope (exhumation rate) and h_{c_i} is the intercept of i-th segment. Given that any two segments must intersect at an age of break a_{br_i}, only h_{c_0} (or simply h_c, the modern elevation of the closure isotherm) needs to be defined, the rest are given by

$$h_{c_i} = h_{c_{i-1}} + a_{br_i}(e_{i-1} - e_i). \tag{5.4}$$

In this parameterization, $\theta^n = (h_c, e_0, \ldots, e_n, a_{br_1}, \ldots, a_{br_n})$.

The thermochronometric error σ (Eq. 5.2), as seen in bedrock replicate analyses, is approximately proportional to the thermochronometric age:

$$\sigma = s\bar{b}. \tag{5.5}$$

The parameter s can either be set to a fixed value or estimated with the other model parameters. Alternatively, it can be estimated from bedrock replicate analyses, preferably coming from the same bedrock as that underlying the source catchment of detrital sediment.

While the long-term exhumation history is expressed in p_b, variations in short-term sediment supply and surface concentrations of detrital minerals of interest are included in the sampling pdf, $p_s(w)$ (Fig. 5.1). A uniform p_s, for example, implies uniform erosion and the uniform concentration of detrital grains across the watershed. Models for the dependence of erosion rate on hillslope, lithology, or land cover can be implemented through $p_s(w|\lambda)$, where λ is a set of parameters to the erosion model.

Given two sets of parameters θ and λ to the functions $\bar{b}$ and p_s, respectively, and the parameter s to p_b, the probability for observing an n-grain detrital sample $D = (a_1, \ldots, a_n)$ is

$$p(D|\theta, \lambda, s) = \prod_{i=1}^{n} p_d(a_i|\theta, \lambda, s), \tag{5.6}$$

given that the individual age measurements are independent.

It is easy to include bedrock thermochronometric data into this model. The probability of observing an age a at a point w is defined by Eq. 5.2. The likelihood of the exhumation parameters θ (and thermochronometric error s), given a suite of bedrock samples $B = (a_1, \ldots, a_m)$, is then

$$p(B|\theta, s) = \prod_{i=1}^{m} p_b(a_i|w_i, \theta, s). \tag{5.7}$$

In the Bayesian approach, the probability distribution of the model parameters, given the observed data (called the posterior probability), is a product of the model likelihood function, which quantifies data fit, with the prior distribution of the parameters, which expresses any knowledge about the parameters prior to observing the data (Eq. B.1). The posterior of the erosion model, that includes both bedrock and detrital data, is

$$p(\theta, \lambda, s|D, B) = Cp(D|\theta, \lambda, s)p(B|\theta, s)p(\theta)p(\lambda)p(s), \tag{5.8}$$

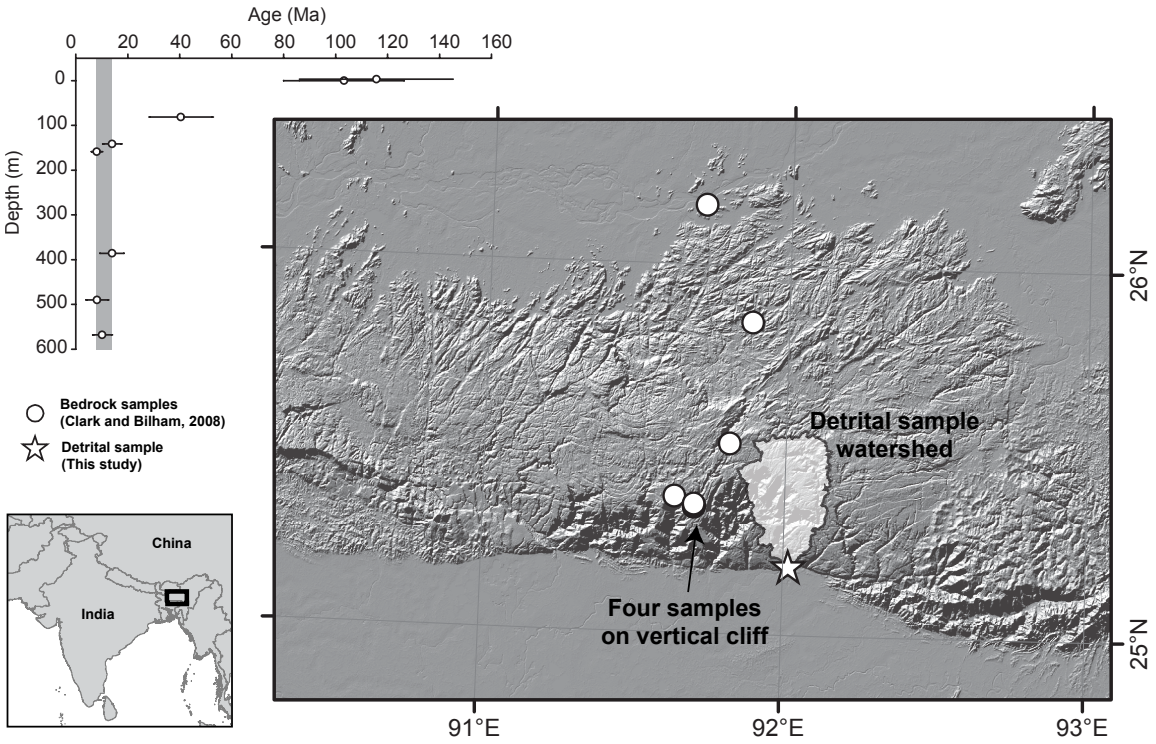

Figure 5.2: Digital elevation map of the Shillong Plateau with locations of bedrock samples (Clark and Bilham, 2008) and a detrital sample (Table C.1). Age-depth below unconformity plot for the bedrock samples shows an increase in exhumation rate around 8–14 Ma (Clark and Bilham, 2008).

where $p(\theta)$, $p(\lambda)$ and $p(s)$ are priors of the model parameters and C is a constant that scales the posterior pdf, so that it integrates to one. This constant is usually estimated numerically (see B).

5.4 Determining erosion history from detrital data: Shillong Plateau example

Changes in tectonic regime or climate often result in changes in rates of exhumation recorded by cooling ages. Bedrock transects have been successfully used to date such events ("break-in-slope" models, e.g. Fitzgerald et al. (1995)). Clark and Bilham (2008) use such a transect, comprising eight bedrock (U-Th)/He samples (54 single grain analyses), to infer mid to late Miocene (8–14 Ma; Fig. 5.2) acceleration of exhumation in the Shillong Plateau, India, indicating the initiation of plateau

uplift. Below we illustrate the usefulness of our approach to estimating the timing of exhumation of the Shillong Plateau from a new 17-grain detrital (U-Th)/He sample (Table C.1, C) collected from the Dawki river at the southern edge of the Shillong Plateau (Fig. 5.2).

We model bedrock ages as a single break-in-slope linear function of elevation, which is parameterized by $\theta^1 = (h_c, e_0, e_1, a_{br})$ according to Eq. 5.3. Assuming spatially uniform erosion ($p_s = 1/W$, where W is the watershed area) leaves θ^1 and s the only free parameters in the model:

$$p(\theta^1, s|D) = Cp(D|\theta^1, s)p(\theta^1)p(s). \tag{5.9}$$

This equation states that the probability of the parameters, given the observed detrital distribution, is proportional to the probability of observing the detrital distribution, given the parameters and any prior information about these parameters. The prior information can be used to refine and constrain the model in a variety of ways. For example, knowledge of the local geothermal gradient or a given mineral phase's diffusion kinetics can be incorporated into the model through the informative prior $p(h_c)$ which provides constraint on the depth of the closure isotherm. Unrealistic parameter values (closure isotherm at elevations higher than the sample, or negative erosion rates) can be excluded by setting their prior probability to zero. In the case of the Shillong Plateau data, we use non-informative priors (i. e. the probability of each parameter is uniformly distributed over a large range of potential values): $p(e_i) = \mathcal{U}(0.001, 1)$, $p(a_{br}) = \mathcal{U}(0, 60)$, $p(h_c) = \mathcal{U}(-1, 4)$ and $p(s) = \mathcal{U}(0.05, 0.5)$.

Now that the model is defined, the MCMC algorithm is used to generate sufficiently long (10^5) chains of plausible parameter values, which after testing for convergence, burning and thinning (Gelman et al., 2004) are taken as the posterior samples.

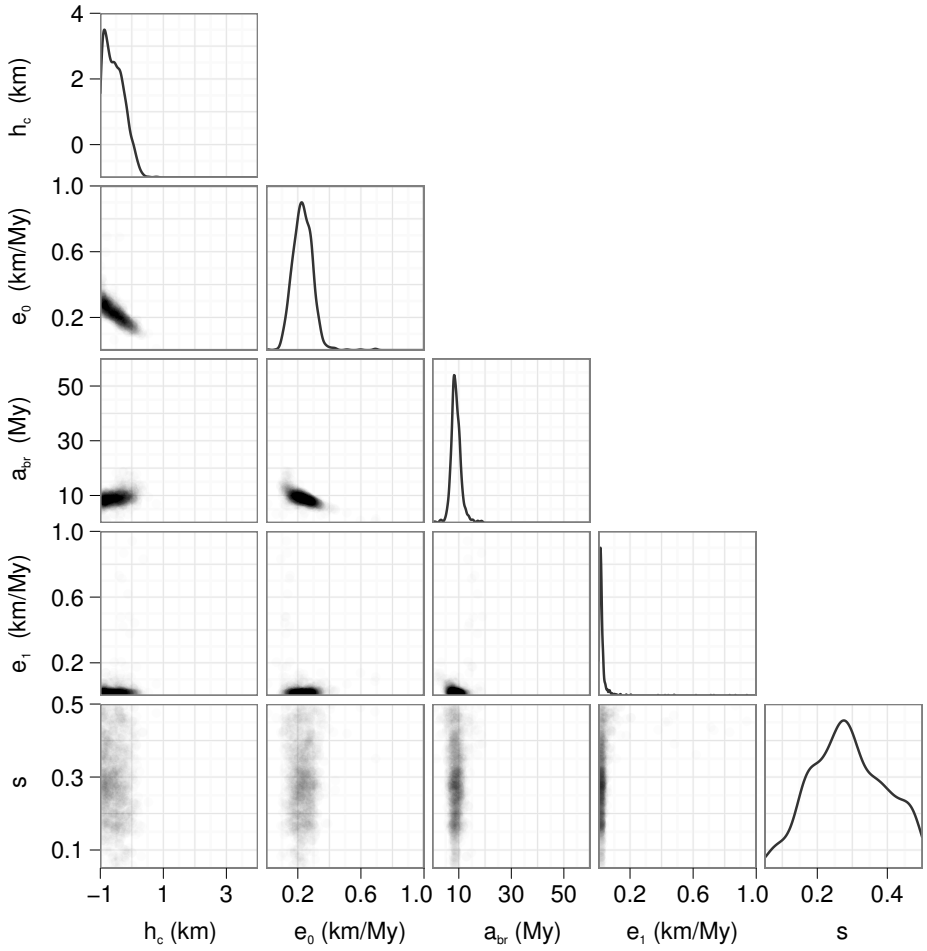

Figure 5.3: Matrix plot summarizing the posterior distribution of the Shillong model. Plots along the diagonal show marginal posterior densities of individual parameters. Scatter-plots off the matrix diagonal show the relationships between the parameter pairs. Axes of the plots are limited by ranges of uniform priors of the parameters.

These samples serve two purposes: first, they are used to approximate the posterior distribution of the parameters (i. e. the estimate of the model parameters in the Bayesian sense) and second, they are used to assess how well the model fits the data.

For the Shillong sample we obtain the following parameter estimates: $h_c = -0.55 \pm 0.52$ km[1], $e_0 = 0.23 \pm 0.13$ km/My, $e_1 = 0.03 \pm 0.14$ km/My, $a_{br} = 9.0 \pm 4.0$ Ma and $s = 0.3 \pm 0.2$. All estimates, except for h_c and e_1, are contained within their prior distributions, indicating that prior information is not affecting the posterior es-

[1]In this paper we summarize posterior distributions by their *mean* $\pm 2 \times$ *standard deviation*. This interval contains approximately 95% of all possible values.

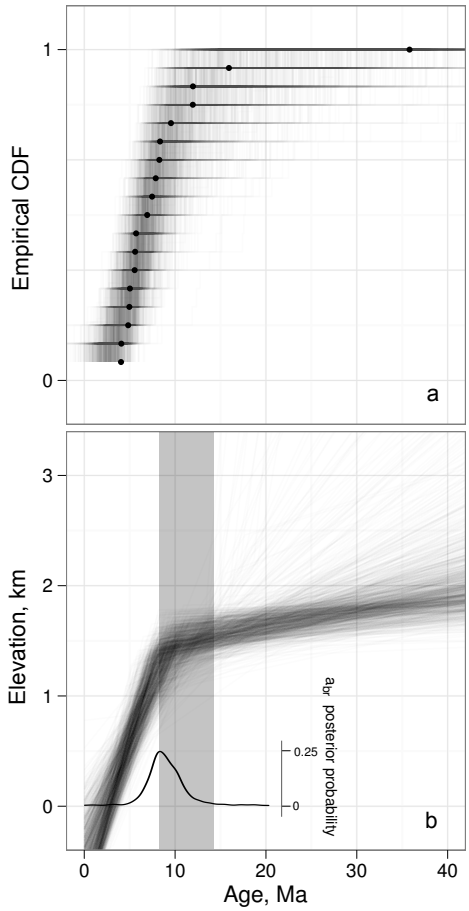

Figure 5.4: Goodness of fit (a) and age-elevation (b) plots for a break-in-slope model based on the Shillong Plateau sample (Table C.1). Gray band (b) marks timing of rapid exhumation onset inferred from a bedrock transect (8–14 Ma, Clark and Bilham, 2008). Black curve (b) is a posterior density of the time of the exhumation rate change a_{br} predicted from the detrital sample.

timate (Fig. 5.3). Both the elevation of the closure isotherm and pre-break-in-slope erosion rate distributions are "clipped" at the lower bounds of their priors (Fig. 5.3), indicating that the priors, and not the data, are constraining the minimum values of these posteriors. A wider prior for e_2 would not affect the posterior, as it is not possible to infer burial histories ($e < 0$) with the age-elevation approach. A wider prior for h_c would result in a part of the posterior distribution yielding h_c below -1 km a.s.l. However, such closure isotherm depths are not expected from from the known geothermal gradient and kinetics of He diffusion in apatite. Since our model assumes the cooling ages depend solely on elevation and are invariant in the horizontal direction, the exhumation parameters can also be visualized with an age-elevation plot (Fig. 5.4b).

To check how well the model fits the data we use the estimated model (posterior samples) to generate a number of synthetic datasets and compare them with the observed dataset. Following Vermeesch (2007), we choose to visually compare cumulative probability density plots of the actual sample and the synthetic samples, generated for each of the parameter values in the posterior sample. Overlap of the synthetic and real samples (Fig. 5.4a), indicates an acceptable model fit.

5.4.1 Discussion of the Shillong Plateau modeling results

Our estimate for the timing of change in erosion rate (9.0 ± 4.0 Ma) overlaps with published estimates based on bedrock transects of 8–14 Ma (Clark and Bilham, 2008) and 8.9–15.2 Ma (Biswas et al., 2007). In addition, our estimate for post-Miocene exhumation rate ($e_0 = 0.23 \pm 0.13$ km/My) is comparable with these previous studies (0.1–0.4 and 0.09–0.55 km/My, respectively). Neither of these studies proposed a pre-Miocene exhumation rate. Our estimated pre-Miocene exhumation rate may be unreliable: a low exhumation rate (Fig. 5.3) implies long residence time of the

samples in the partial retention zone, which results in the closure temperature being strongly dependent on the cooling rate and leads to an over-estimation of the elevation transect-derived exhumation rate (e.g. Fitzgerald et al., 1995). A more accurate estimate of the slow pre-Miocene exhumation rate could be obtained using a thermal diffusion/annealing model. Finally, an estimate for s, derived from bedrock replicates of Clark and Bilham (2008), is 0.4 ± 0.1. This value agrees with the estimate derived from the detrital model (0.3 ± 0.2).

5.5 Quantifying spatially variable erosion: Sierra Nevada example

In the previous example, spatial variations in erosion rate are small enough that the available data does not falsify the assumption of uniform erosion. Using a published dataset from the Sierra Nevada, California, we consider an example where the spatial variability of erosion has a noticeable (given the sample size) effect on the distribution of detrital ages. We analyze an apatite (U-Th)/He dataset that consists of detrital samples collected from two adjacent catchments and an elevation transect of nine bedrock samples collected from the same catchments (House et al., 1997; Stock et al., 2006).

To constrain the thermochronometric error we use a published bedrock apatite (U-Th)/He dataset (Clark et al., 2005) containing 181 replicate analyses of 37 samples from the Sierra Nevada, as well as 14 replicates (3 samples) from Stock et al. (2006). The mean estimate of the error s, using these data, was between 0.11 and 0.13, for all of the following Sierra Nevada models (see supplementary materials).

First, we fit a uniform erosion and constant age-elevation gradient model independently to each of the two detrital samples without using the bedrock data. The joint posterior distribution of model parameters e and h_c can be visualized using a

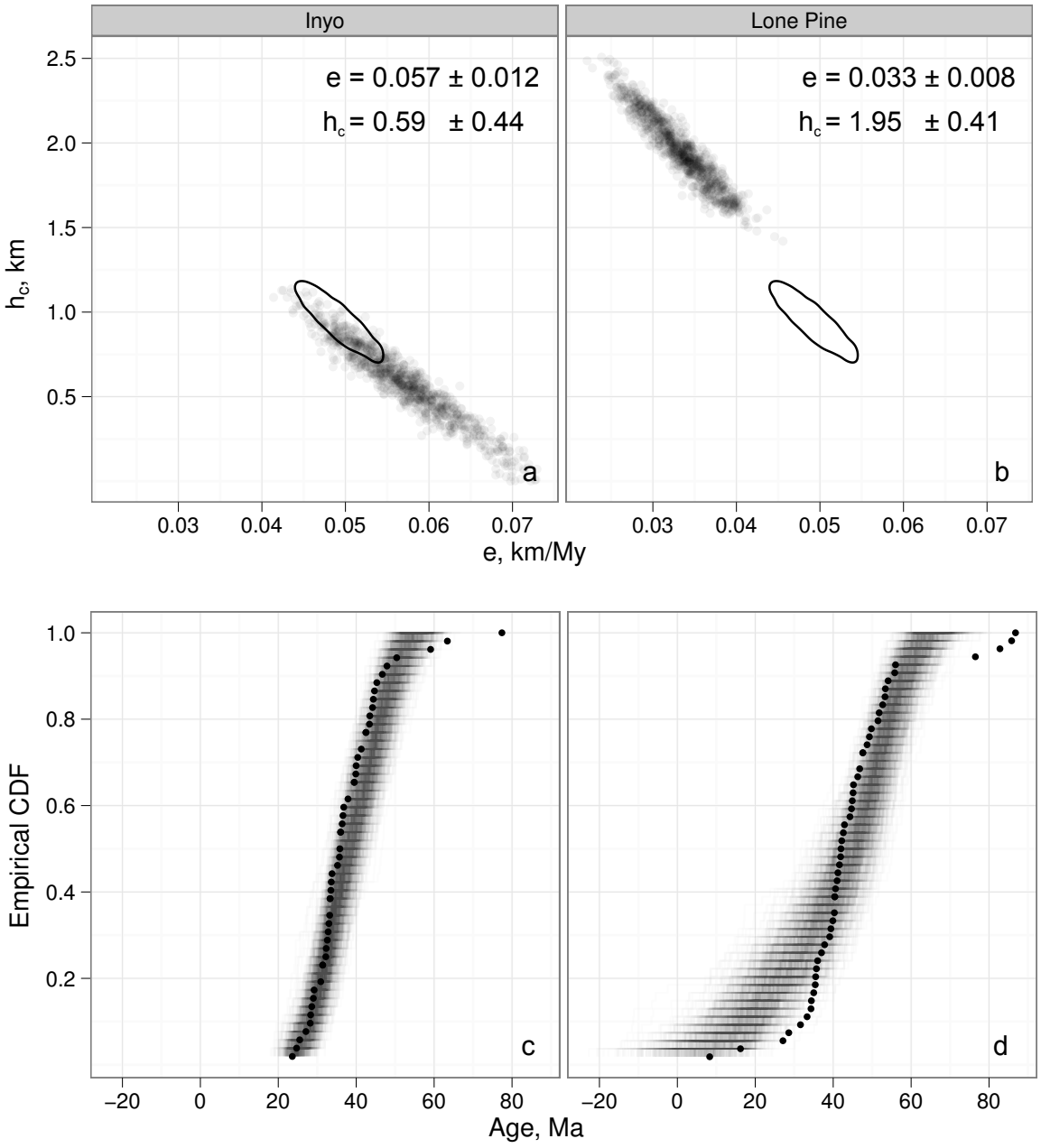

Figure 5.5: Posterior samples $p(\theta^0|D_I)$ (a, grey dots) and $p(\theta^0|D_L)$ (b, grey dots) for the uniform erosion and linear age-elevation relationship model derived from detrital data. Numbers on the plots give mean a posteriori estimates and approximate 95% CIs (2 std. dev.). Ellipses show the approximate 95% credible region derived from the bedrock data (see text). (c, d) Corresponding goodness of fit plots. The discrepancy between the observed detrital ages (black) and the synthetic samples (gray), especially in the Lone Pine Creek case, is an indicator of model misfit to the data.

scatter plot, in which the density of the parameter values (two-dimensional in this case) approximates parameter probability (Fig. 5.5a,b).

Since the bedrock data were not used in this model, we can do cross-validation, by comparing predictions from the detrital model with predictions derived from the bedrock elevation transect. For this we estimate the posterior probability $p(\theta^0, s|B)$ using Eqs. 5.2 and 5.5. This bedrock-derived posterior (shown as a 95% credible region contour, Fig. 5.5a,b) is similar to the posterior of the Inyo Creek uniform erosion, linear age-elevation model. A goodness of fit plot (Fig. 5.5c) also does not indicate any major discrepancies, suggesting that a model of uniform erosion and constant exhumation rate reasonably describes Inyo Creek detrital data, as has previously been demonstrated (Stock et al., 2006).

On the other hand, the uniform erosion, linear age-elevation model poorly describes the Lone Pine Creek detrital data. First, the estimate for the elevation of the closure isotherm h_c is unreasonably high, as the mean elevation of the catchment (3.3 km) would require a $\sim 50°$C/km geothermal gradient. Second, the posterior derived from this model does not overlap with the bedrock transect prediction. Third, it is difficult to explain the difference in the estimated erosion rates and depths to closure isotherm between the adjacent and tectonically similar Inyo and Lone Pine creek catchments. Lastly, inadequacy of the uniform erosion model for the Lone Pine Creek data set is corroborated by the goodness of fit plot (Fig. 5.5d), which shows a substantial mismatch between the observed and simulated data.

Additionally, both models fail to explain several of the oldest ages (>60 Ma) observed in the Inyo and Lone Pine detrital data sets (Fig. 5.5c,d). Below we formulate a model that attempts to addresses the above issues.

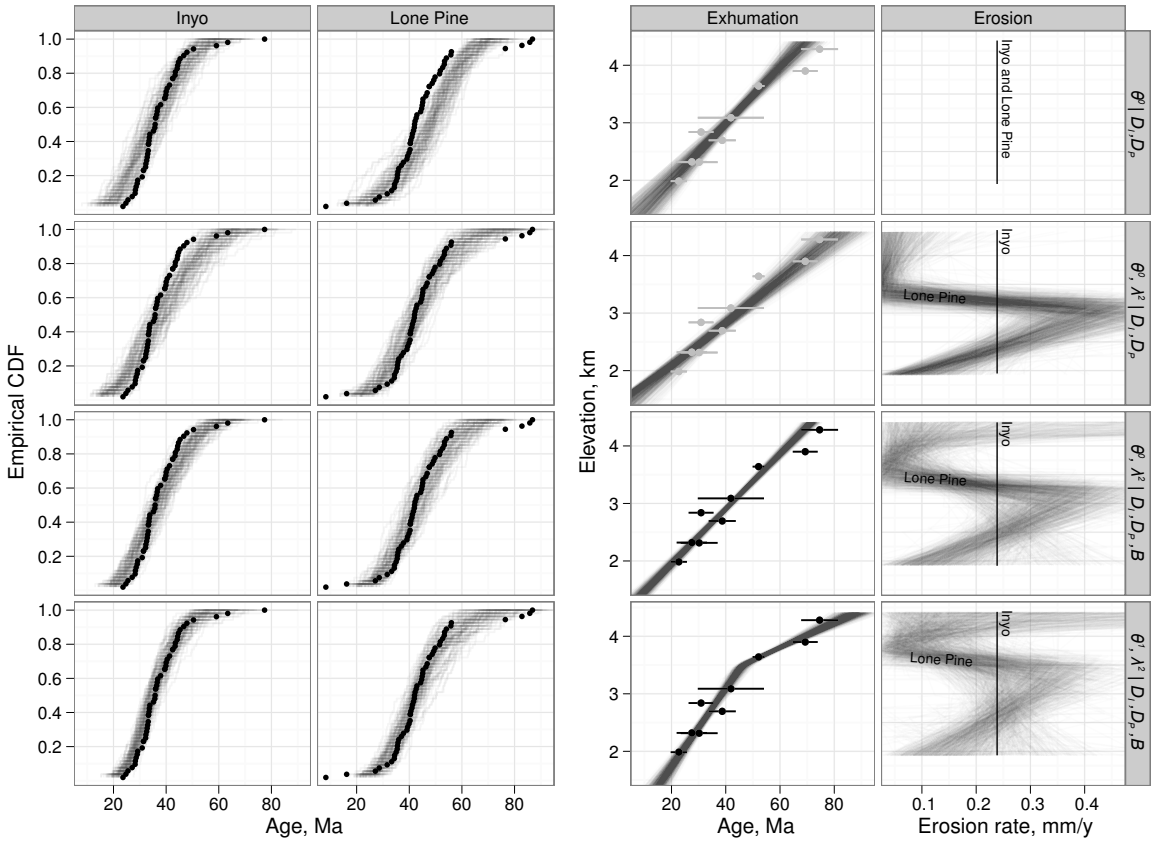

Figure 5.6: Inversion results for constant exhumation, uniform erosion ($p(\theta^0|D_I, D_L)$) and non-uniform erosion ($p(\theta^0, \lambda^2|D_I, D_L)$) models based on detrital data; as well as linear ($p(\theta^0, \lambda^2|D_I, D_L, B)$) and break-in-slope ($p(\theta^1, \lambda^2|D_I, D_L, B)$) exhumation, non-uniform erosion models based on detrital and bedrock data. Left block shows goodness of fit plots for Inyo and Lone Pine Creek detrital samples. On the right are estimated long-term exhumation parameters plotted in age-elevation space (gray lines) together with the observed bedrock ages (dots with 2σ error bars, light gray, when not used in modeling) and the distribution of the predicted sampling probabilities for the Lone Pine creek catchment, converted into the apparent short-term erosion rate based on the catchment-average erosion rate (0.24 ± 0.03 mm/y) derived from a CRN study (Stock et al., 2006).

5.5.1 Simultaneous estimation of spatial and temporal patterns of erosion

Assuming the detrital grains are uniformly distributed in bedrock across the catchments (Stock et al., 2006), and no sediment storage or grain destruction occurs upstream from the detrital sampling sites, the distribution of detrital cooling ages can be used to estimate relative erosion rates across the catchments.

Inyo and Lone Pine creeks are adjacent and lie on the same tectonic block, permitting the assumption of identical exhumation histories. Figure 5.6 ($\theta^0|D_I, D_P$) shows results of a model that uses data from both detrital samples to estimate a common long-term exhumation history, assuming constant and uniform erosion in both Inyo and Lone Pine creeks. The prediction of this detrital-only model is compatible with bedrock data (dots with error bars on the age-elevation plot, Fig. 5.6). The misfit of the Lone Pine Creek detrital ages, however, is still present and we address it below by relaxing the uniform erosion assumption.

In contrast to the common exhumation history experienced by Inyo and Lone Pine creeks, differences in short term erosion patterns between the two catchments may be expected, as Lone Pine Creek experienced Pleistocene glaciation, while Inyo Creek did not (Stock et al., 2006; Dühnforth et al., 2008). The Inyo Creek data are explained by the combination of a linear age-elevation relationship and uniform erosion, while this model substantially misfits the Lone Pine Creek data. Spatially variable erosion in the Lone Pine Creek watershed, prescribed through the probability of sampling p_s as a piecewise linear function of elevation, may account for this misfit.

Models with one to five linear segments were estimated. Predictions of short-term erosion from models with greater than three segments are similar to each other, which suggests that the three-segmented function describes spatial non-uniformity in the Lone Pine Creek sufficiently well (Fig. 5.6, $\theta^0, \lambda^2|D_I, D_P$; supplementary materials).

We do not use DIC (Eq. B.3; supplementary materials) for model selection, as this criterion is valid only for approximately normal posterior distributions.

As previously shown, it is possible to estimate both exhumation and erosion patterns from detrital data. However, some trade off between the effects of these two processes on the detrital age distributions is expected. Joint inversion of bedrock and detrital data produces more accurate estimates of the erosion model. To include bedrock cooling ages in the model, a likelihood of e and h_c as a function of the observed bedrock ages needs to be defined. This likelihood is a product of individual bedrock age probability densities that depend on the modeled bedrock age $\bar{b}$ and their thermochronometric error (Eq. 5.2).

The addition of bedrock data to the constant exhumation and spatially variable Lone Pine Creek erosion model (Fig. 5.6, $\theta^0, \lambda^2 | D_I, D_P, B$) results in a more precise estimate of exhumation. With this greater precision, a misfit to a few older detrital ages in both samples is obvious. A similar misfit of the model is observed with the bedrock data, where the two oldest ages are older than could be expected from the model (Fig. 5.6, $\theta^0, \lambda^2 | D_I, D_P, B$). This misfit can be explained by a non-steady state exhumation model.

A piecewise linear age-elevation model with one break (Fig. 5.6, $\theta^1, \lambda^2 | D_I, D_P, B$) has a better fit to the bedrock data than the constant exhumation rate model and also addresses the presence of anomalously old ages in both catchments. These ages were previously ascribed to sediment recycling (Stock et al., 2006). This hypothesis is viable for Lone Pine Creek, where sediment storage is common, but problematic for Inyo Creek, which has little or no long-term sediment storage.

5.5.2 Discussion of the Sierra Nevada modeling results

Erosion rates in the Lone Pine Creek catchment (Fig. 5.6) were computed from the estimated sampling probabilities (p_s), which yield relative probabilities of detrital grains eroding from a given elevation, scaled by basin-wide erosion rates derived from CRN concentrations (Stock et al., 2006). This scaling yields an estimate of absolute erosion rate. We acknowledge that this CRN-derived erosion rate was obtained from Inyo Creek, and thus that its accuracy in constraining basin-wide erosion rates for Lone Pine Creek may be limited; nonetheless, the relative rates of erosion as a function of elevation are appropriately scaled. Erosion rates at ∼3 km a.s.l. are 3 to 4 times higher than at the catchment outlet (∼2 km a.s.l.). Above ∼3 km, erosion rates drop significantly, with little material apparently derived from above ∼3.5 km.

The observed spatial pattern of short-term erosion rate could result from a number of factors. As previously demonstrated, there is a paucity of apatite grains from higher elevations in the catchment, which may result from sediment storage in glacial cirques (Stock et al., 2006), or may represent true spatial variations in sediment production resulting from glacial polishing of high elevation surfaces above tree line versus biotically driven soil production and transport at lower elevations (e.g. Dixon et al., 2009). Alternatively, the observed spatial pattern of short-term erosion may be the result of sediment input from a spatially limited, large magnitude erosional event such as a rock fall or landslide (e.g. Niemi et al., 2005; Yanites et al., 2009). Deriving the exact geomorphic mechanisms for this pattern is beyond the scope of this study, but accurately quantifying the spatial patterns of short-term erosion is a fundamental step towards understanding processes such as those described above, any of which could effectively be incorporated within our detrital modelling framework in future studies.

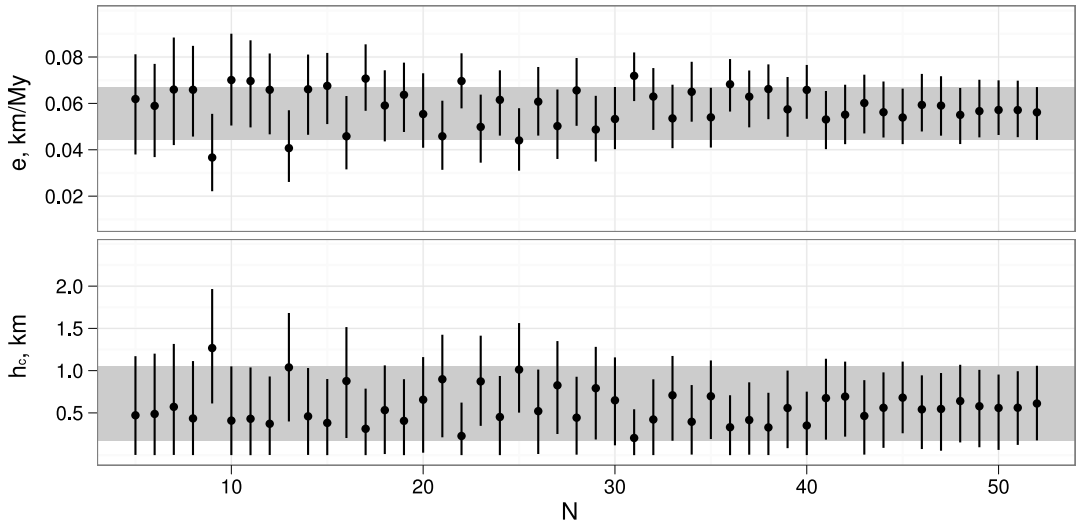

Figure 5.7: Posterior estimates (mean and 95% CI) based on random n-grain sub-samples of the Inyo Creek sample. Grey bands show 95% CI derived from the complete 52-grain sample.

The change in rate of exhumation at 47 Ma represents a three-fold increase in erosion rate, yet the absolute rates remain low and within previous bedrock-based estimates (Clark et al., 2005). While this change does not appear to represent a significant tectonic or exhumational event because the overall rates remain so slow, we speculate that it may reflect a shift in climatic conditions across the Sierra Nevada in Eocene time, or an integration of fluvial systems, from Paleocene and early Eocene rivers with headwaters restricted to the Pacific margin (Hutchison, 1982, 2004; Lechler and Niemi, 2011; Cecil et al., 2010) to late Eocene and Oligocene river systems that traversed the Sierra Nevada and tapped the continental interior (Cassel et al., 2009; Henry and Faulds, 2010). Alternatively, the Sierra may be responding to changes in far-field stress conditions resulting from reorganization of oceanic plates in the Pacific at about this time (Lonsdale, 1988; Atwater, 1989).

5.6 How many grains are needed for an erosional study?

Low-temperature detrital thermochronometric ages can be described by a mixture model that reflects the continuous cooling of rock as it is exhumed towards the surface of the Earth. As a result of this continuous cooling, bedrock ages can be defined as a function of their location within the catchment parametrized by a few unknowns. In this way, low-temperature thermochronometric ages differ from high-temperature ages used in provenance studies that reflect discrete and unknown number of episodes of mineral crystallization (e.g. Vermeesch, 2004; Jasra et al., 2006). The model presented here offers a platform to assess the sample size necessary for low-temperature detrital thermochronometric studies. Given that the detrital sample size requirement is dictated by a specific model, its complexity, hypothesis being tested, precision requirements, data uncertainty, and catchment size, among other things, it is unlikely that a general minimum sample size can be defined. However, sample size can be estimated for any given model. This is done by simulating datasets of various sizes with the model and using these datasets to estimate the model parameters along with their precision. It should be kept in mind that the size of the artificial sample that produces a desired precision will be a minimum estimate of the real sample size, since the plausible model is certainly not encompassing all of the complexity contained within a real sample.

In the case of the Sierra Nevada, the existing dataset can be used to test whether or not the sample size is large enough to estimate the parameters of our proposed erosion model. A sample size of 54 grains is large enough to show (through GOF plot, Fig. 5.5d) that the uniform steady state erosion model is not suitable for Lone Pine Creek, while the 52 grain sample from the Inyo Creek catchment is large enough

to estimate exhumation parameters with a precision, indicated by the posterior distribution (Fig. 5.5a), that does not contradict the prediction made from the bedrock samples. The Inyo Creek sample is also large enough to suggest nonuniform erosion within the catchment; however the small degree of misfit compared to the spread of the simulated samples (Fig. 5.5c) suggest that this non-uniformity does not significantly affect the predictions at the level of precision afforded by the sample size. Combining both detrital and bedrock samples results in enough data to estimate the erosion distribution as a function of elevation with the precision indicated by the spread of models on Figure 5.6.

To further illustrate the effect of the sample size on the precision of parameter estimates, and to show that small samples can provide useful information, we determined exhumation rate and the elevation of the closure isotherm with a uniform erosion, linear age-elevation relationship model from random 5 to 52 grain sub-samples (drawn without replacement) of the Inyo Creek detrital sample (Stock et al., 2006). Even though the accuracy and precision of estimates (Fig. 5.7) increase with sample size (as compared to the estimate derived from the entire 52 grain population), the smallest five-grain sample allows a meaningful prediction. There is occasional bias in the subsampled data to under-predict e and over-predict h_c. This is a result of the model misfit to the three old ages (Fig. 5.5c) present in the sample. These old ages are periodically sub-sampled and bias the parameter estimation with a bias that is larger for smaller samples. The frequency of sampling these old ages increases as the size of the sub-sample increases, but their effect on parameter estimation is smaller with increased sample size. These "errors" in prediction, caused by high-leverage outliers (i. e. data not explained by the simple linear age-elevation model) can be caught using goodness of fit diagnostics.

5.7 Future directions

The age-elevation models above assume a vertical advection path and a flat closure isotherm. In many cases, however, these assumptions bias the interpretation of age-elevation relationships (Valla et al., 2010). Tectonically asymmetric structures and climatic gradients tend to result in non-vertical exhumation paths and low-temperature thermochronometers may be sensitive to topographic (e.g. Stuwë et al., 1994) or hydrologic (e.g. Whipp and Ehlers, 2007) effects on the near-surface thermal field. Both of these aspects can be addressed using our approach, since the model (Eq. 5.1) can be used to describe any age-spatial coordinate relationship. In the case of oblique exhumation paths, a coordinate transformation can be affected in which elevation is substituted by a distance, parallel to the advection vector, that results in a model identical to the vertical exhumation model, but with non-vertical particle paths. Such a model implies that the closure isotherm is perpendicular to the advection direction. A model that treats thermal field distortion due to topography will generally require computing p_b (in Eq. 5.1) with a thermal-kinematic model such as Pecube (Braun, 2003), but such a computation could be performed and implemented in the modelling strategy presented here, if the effect is significant enough to warrant consideration (Valla et al., 2010). Estimating and testing of process-based geomorphic models could also be implemented within our modelling framework through p_s (Eq. 5.1) including spatial variability in sediment supply resulting from hillslope, upstream area, curvature, land cover, or bedrock geology.

The use of a thermochronometer capable of providing a thermal history from a single grain, such as $^{4}He/^{3}He$ (or equally, $^{40}Ar/^{39}Ar$, or apatite fission-track length modeling) would significantly strengthen the technique. With these thermochronometers,

each grain carries some information on its cooling history though a range of temperatures, thus independently constraining exhumation. If this information could be reliably extracted, it would allow better resolution of not only exhumation, but also grain provenance that would lead to more confident short-term erosion mapping. In addition, by constraining both cooling history (from single grains) and exhumation (from age distributions), detrital $^{4}He/^{3}He$ ($^{40}Ar/^{39}Ar$, AFT) thermochronometry could provide information on the geothermal gradient throughout the recorded history of exhumation and cooling.

5.8 Conclusions

We present a new approach to statistical modelling of erosion with detrital low-temperature thermochronometric data. This approach advances current methods by permitting inversion for complex temporally and spatially variable exhumation histories. Rigorous treatment of uncertainty allows the extraction of reliable information even from small datasets (e. g. less than 20 grains for a simple erosion model). We demonstrate that this method replicates exhumational histories derived from bedrock thermochronometric datasets, and does so with substantial improvements in analytical efficiency, requiring $\sim 1/3$ the laboratory analysis of a comparable bedrock study. In addition to estimating exhumation histories, this approach provides an effective means of mapping short-term erosion with detrital data, and, in contrast to previous approaches, does not require bedrock sampling. Although the models presented here are relatively simple, inverting detrital age distributions using complex thermokinematic and geomorphic models is technically identical.

5.9 Acknowledgements

This work was funded by NSF grants EAR-0908711 (MKC and NAN), EAR-0810067 (NAN) and EAR-0607458 and -0549748 (MKC), and by a grant from the Scott Turner Fund from the Department of Geological Sciences at the University of Michigan (BA). We thank R. Bilham, A. Lechler, S. Dasgupta, T. D. Gupta, S. Sengupta, K. Muzumdar, and L. H. Moirangcha for sample collection and field support; L. Staisch for sample preparation; K. Farley and L. Hedges for thermochronometrical analyses at Caltech's Noble Gas Laboratory. A. Duvall and two anonymous reviewers provided constructive criticisms that greatly improved this manuscript.

Bibliography

Atwater, T. M. Plate tectonic history of the northeast Pacific and western North America. In Winterer, E. L., Hussong, D. M. and Decker, R. W., editors, *The geology of North America*, volume N: The northeastern Pacific Ocean and Hawaii, pages 21–72. Geol. Soc. Amer., 1989.

Biswas, S., Coutand, I., Grujic, D., Hager, C., Stckli, D. and Grasemann, B. Exhumation and uplift of the Shillong plateau and its influence on the eastern Himalayas: New constraints from apatite and zircon (U-Th-[Sm])/He and apatite fission track analyses. *Tectonics*, 26:TC6013, 2007. ISSN 0278-7407.

Braun, J. Pecube: a new finite-element code to solve the 3D heat transport equation including the effects of a time-varying, finite amplitude surface topography. *Comput. Geosci.*, 29:787–794, 2003. ISSN 0098-3004. doi:10.1016/S0098-3004(03)00052-9.

Brewer, I. D. and Burbank, D. W. Thermal and kinematic modeling of bedrock and

detrital cooling ages in the central Himalaya. *J. Geophys. Res.*, 111:B09409, 2006. doi:10.1029/2004JB003304.

Brewer, I. D., Burbank, D. W. and Hodges, K. V. Modelling detrital cooling-age populations: insights from two Himalayan catchments. *Basin Res.*, 15:305–320, 2003.

Cassel, E. J., Calvert, A. T. and Graham, S. A. Age, geochemical composition, and distribution of Oligocene ignimbrites in the northern Sierra Nevada, California: implications for landscape morphology, elevation, and drainage divide geography of the Nevadaplano. *International Geology Review*, 51:723–742, 2009. doi:10.1080/00206810902880370.

Cecil, M. R., Ducea, M. N., Reiners, P., Gehrels, G., Mulch, A., Allen, C. and Campbell, I. Provenance of Eocene river sediments from the central northern Sierra Nevada and implications for paleotopography. *Tectonics*, 29:TC6010, 2010. doi:10.1029/2010TC002717.

Clark, M. K. and Bilham, R. Miocene rise of the Shillong Plateau and the beginning of the end for the eastern Himalaya. *Earth Planet. Sci. Lett.*, 269:336–350, 2008.

Clark, M. K., Maheo, G., Saleeby, J. and Farley, K. A. The non-equilibrium landscape of the southern Sierra Nevada, California. *GSA Today*, 15(9):4–10, 2005.

Dixon, J. L., Heimsath, A. M., Kaste, J. and Amundson, R. Climate-driven processes of hillslope weathering. *Geology*, 37:975–978, 2009. doi:10.1130/G30045A.1.

Dühnforth, M., Densmore, A. L., Ivy-Ochs, S. and Allen, P. A. Controls on sediment evacuation from glacially modified and unmodified catchments in the eastern Sierra Nevada, California. *Earth Surf. Proc. Land.*, 33:1602–1613, 2008.

Fitzgerald, P. G., Sorkhabi, R. B., Redfield, T. F. and Stump, E. Uplift and denudation of the central Alaska Range: A case study in the use of apatite fission track thermochronology to determine absolute uplift parameters. *J. Geophys. Res.*, 100:20,175–20,191, 1995. ISSN 0148-0227. doi:10.1029/95JB02150.

Gallagher, K., Charvin, K., Nielsen, S., Sambridge, M. and Stephenson, J. Markov chain Monte Carlo (MCMC) sampling methods to determine optimal models, model resolution and model choice for Earth Science problems. *Mar. Pet. Geol.*, 26:525–535, 2009.

Gallagher, K., Stephenson, J., Brown, R., Holmes, C. and Fitzgerald, P. Low temperature thermochronology and modeling strategies for multiple samples 1: Vertical profiles. *Earth Planet. Sci. Lett.*, 237:193–208, 2005. ISSN 0012-821X. doi: 10.1016/j.epsl.2005.06.025.

Gelman, A., Carlin, J. B., Stern, H. S. and Rubin, D. B. *Bayesian data analysis*. Chapman & Hall/CRC, 2nd edition, 2004.

Henry, C. D. and Faulds, J. E. Ash-flow tuffs in the Nine Hill, Nevada, paleovalley and implications for tectonism and volcanism of the western Great Basin, USA. *Geosphere*, 6:339–369, 2010.

Hopcroft, P. O., Gallagher, K. and Pain, C. C. A Bayesian partition modelling approach to resolve spatial variability in climate records from borehole temperature inversion. *Geophysical Journal International*, 178:651–666, 2009. ISSN 1365-246X.

House, M. A., Wernicke, B. P., Farley, K. A. and Dumitru, T. A. Cenozoic thermal evolution of the central Sierra Nevada, California, from (U-Th)/He thermochronometry. *Earth Planet. Sci. Lett.*, 151:167–179, 1997.

Hutchison, J. H. Turtle, crocodilian, and champsosaur diversity changes in the Cenozoic of the north-central region of western United States. *Palaeogeogr. Palaeoclimatol. Palaeoecol.*, 37:147–164, 1982.

Hutchison, J. H. A new eubaenine, Goleremys mckennai, gen. et sp. n., (Baenidae: Testudines) from the Paleocene of California. *Bulletin of Carnegie Museum of Natural History*, 36:91–96, 2004. doi:doi: 10.2992/0145-9058(2004)36[91:ANEGMG]2.0.CO;2.

Jasra, A., Stephens, D. A., Gallagher, K. and Holmes, C. C. Bayesian mixture modelling in geochronology via Markov chain Monte Carlo. *Math. Geol.*, 38:269–300, 2006. doi:10.1007/s11004-005-9019-3.

Lechler, A. R. and Niemi, N. A. Sedimentologic and isotopic constraints on the Paleogene paleogeography and paleotopography of the southern Sierra Nevada, California. *Geology*, 39:In press, 2011.

Leonhardt, R. and Fabian, K. Paleomagnetic reconstruction of the global geomagnetic field evolution during the Matuyama/Brunhes transition: Iterative Bayesian inversion and independent verification. *Earth Planet. Sci. Lett.*, 253:172–195, 2007. ISSN 0012-821X. doi:DOI: 10.1016/j.epsl.2006.10.025.

Lonsdale, P. Paleogene history of the Kula plate: Offshore evidence and onshore implications. *Geol. Soc. Am. Bull*, 100(5):733–754, 1988.

Malinverno, A. Parsimonious Bayesian Markov chain Monte Carlo inversion in a nonlinear geophysical problem. *Geophysical Journal International*, 151:675–688, 2002. ISSN 1365-246X.

Matsu'ura, M., Noda, A. and Fukahata, Y. Geodetic data inversion based on

Bayesian formulation with direct and indirect prior information. *Geophysical Journal International*, 171:1342–1351, 2007. ISSN 1365-246X. doi:10.1111/j.1365-246X.2007.03578.x.

McPhillips, D. and Brandon, M. T. Using tracer thermochronology to measure modern relief change in the Sierra Nevada, California. *Earth Planet. Sci. Lett.*, 296:373–383, 2010.

Niemi, N. A., Oskin, M., Burbank, D. W., Heimsath, A. M. and Gabet, E. J. Effects of bedrock landslides on cosmogenically determined erosion rates. *Earth Planet. Sci. Lett.*, 237:480–498, 2005.

Ruhl, K. W. and Hodges, K. V. The use of detrital mineral cooling ages to evaluate steady state assumptions in active orogens: An example from the central Nepalese Himalaya. *Tectonics*, 24:TC4015, 2005.

Sambridge, M., Gallagher, K., Jackson, A. and Rickwood, P. Trans-dimensional inverse problems, model comparison and the evidence. *Geophysical Journal International*, 167:528–542, 2006. ISSN 1365-246X. doi:10.1111/j.1365-246X.2006.03155.x.

Stephenson, J., Gallagher, K. and Holmes, C. A Bayesian approach to calibrating apatite fission track annealing models for laboratory and geological timescales. *Geochim. Cosmochim. Acta*, 70:5183–5200, 2006. doi:10.1016/j.gca.2006.07.027.

Stock, G. M., Ehlers, T. A. and Farley, K. A. Where does sediment come from? quantifying catchment erosion with detrital apatite (U-Th)/He thermochronometry. *Geology*, 32:725–728, 2006.

Stuwë, K., White, L. and Brown, R. The influence of eroding topography on steady

state isotherms. Applications to fission track analysis. *Earth Planet. Sci. Lett.*, 124:63–74, 1994. doi:10.1016/0012-821X(94)00068-9.

Valla, P. G., Herman, F., van der Beek, P. A. and Braun, J. Inversion of thermochronological age-elevation profiles to extract independent estimates of denudation and relief history—I: Theory and conceptual model. *Earth Planet. Sci. Lett.*, 295:511–522, 2010.

Vermeesch, P. How many grains are needed for a provenance study? *Earth Planet. Sci. Lett.*, 224:441–451, 2004.

Vermeesch, P. Quantitative geomorphology of the White Mountains (California) using detrital apatite fission track thermochronology. *J. Geophys. Res.*, 112:F03004, 2007. doi:10.1029/2006JF000671.

Whipp, D. M. and Ehlers, T. A. Influence of groundwater flow on thermochronometer-derived exhumation rates in the central Nepalese Himalaya. *Geology*, 35:851–854, 2007. doi:10.1130/G23788A.1.

Whipp, D. M., Ehlers, T. A., Braun, J. and Spath, C. D. Effects of exhumation kinematics and topographic evolution on detrital thermochronometer data. *J. Geophys. Res.*, 114:F04021, 2009.

Yanites, B. J., Tucker, G. E. and Anderson, R. S. Numerical and analytical models of cosmogenic radionuclide dynamics in landslide-dominated drainage basins. *J. Geophys. Res.*, 114:F01007, 2009. ISSN 0148-0227. doi:10.1029/2008JF001088.

CHAPTER VI

Conclusions

6.1 Greater Caucasus

The new thermochronometric dataset presented in this dissertation unequivocally shows the onset of rapid exhumation throughout the Greater Caucasus around 5 Ma. No systematic difference in the age of the onset is observed between the eastern and western Greater Caucasus. The pattern of exhumation in the eastern Greater Caucasus eliminates the possibility of climatically driven rapid exhumation. Thus, this exhumation is almost certainly a result of surface uplift.

The recent structure of the Greater Caucasus is produced by thrusting of Eurasia over the Transcaucasus (e.g. Zonenshain and Le Pichon, 1986; Philip et al., 1989). The asymmetric pattern of exhumation with higher rates on the southern front of the Greater Caucasus agrees with the south-verging structure. It is concluded that the onset of thrusting of Eurasia over the Transcaucasus caused the observed uplift and exhumation and therefore began at approximately 5 Ma.

Observation of mid-Miocene deep-marine sediments between the Transcaucasus and Eurasia requires the existence of a deep basin that must have closed some time after mid-Miocene. Since a significant pre-Pliocene exhumation is precluded by the thermochronometric data, it is concluded that this basin closed around 5 Ma bring-

ing in contact buoyant Transcaucasus and Eurasia crust, which collision led to the observed rapid exhumation. This result implies that the subduction of the Greater Caucasus basin could provide a near-field force that explains the appearance of high mountains on the opposite side of the Neotethys suture.

The apparent paradox of the western Greater Caucasus, where high elevations and deep levels of exhumation are associated with low seismicity and little active shortening is resolved. Estimates for a long-term rate of overthrusting on the Main Caucasus fault derived from a thermokinematic model constrained by thermochronometric data agree with the low active convergence rate derived from geodetic observations. The reason why such slow convergence leads to the significant uplift is that most of the deformation in the western Greater Caucasus is concentrated on a single steeply dipping structure. Such focusing is probably a result of juxtaposition of two old and competent lithospheric blocks of Eurasia and Dzirula.

6.2 Periarabia

6.2.1 Collision age

The new data from the Greater Caucasus has implications for the tectonics of the whole Periarabian orogen. Existence of a deep-marine basin connecting the Black Sea and South Caspian basins challenges pre-Pliocene estimates for the age of the collision. However, a new age for the collision is not proposed as the Greater Caucasus results suggest that such an age might not be a useful metric for the Arabia-Eurasia orogen. The foremost problem with determining the age of the collision between Arabia and Eurasia lies in the complexity of the pre-collisional paleogeography of the Arabian segment of the Neotethys. During late Mesozoic and Cenozoic time several island arcs existed between Arabia and Eurasia that collided at different times during the Cenozoic. Each of these collisions can be (mis)interpreted as the

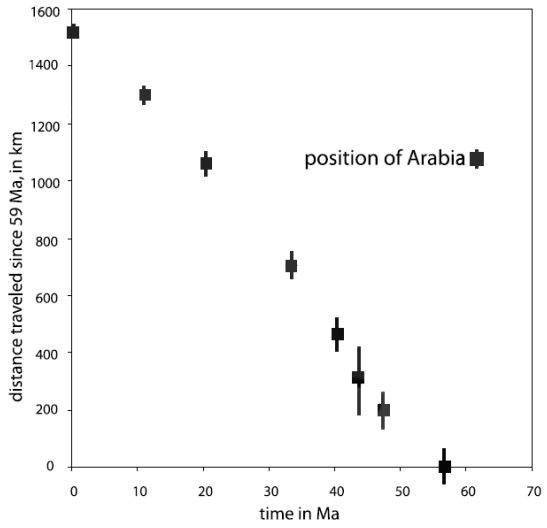

Figure 6.1: Convergence of Arabia (38N, 48E) and Eurasia through the Cenozoic. From McQuarrie et al. (2003).

collision. One might argue that the closure of the last basin marks the "true" or "hard" collision. Paleomagnetic data (Fig. 6.1), however, do not show any significant deceleration in the Arabia-Eurasia convergence suggesting that no "hard" collision has yet happened. Indeed, Arabia is still more than 1000 km away from Eurasia, and the space between the two continents is filled with a few rigid blocks "floating" in the matrix of likely incompetent young island arcs and accretionary complexes.

Another problem with estimating collision age is that, given the complex paleogeography of the Neotethys, elimination of the oceanic basins must have happened diachronously. For example, the Greater Caucasus back-arc basin spans less than half of the width of the Periarabian orogen, and the data presented in this work does not preclude the existence of a land bridge from Arabia to Eurasia (and back) east of the Caspian basin. Moreover, subduction is still ongoing in the South Caspian basin and has not started yet in the Black Sea.

6.2.2 5 Ma reorganization

Late Miocene timing for the closure of the Greater Caucasus basin provides a driving force for 5 Ma tectonic reorganization. With elimination of a subduction zone that could easily accommodate large amounts of shortening, deformation must redistribute into new regions. It is hypothesized that this redistribution led to the onset of Anatolian extrusion and acceleration of exhumation in the Greater Caucasus, Alborz, and Talysh. It is unlikely, however, that the Greater Caucasus collision can be responsible for the tectonic changes in the eastern part of Periarabia (Allen et al., 2011).

6.3 Global impact

Uplift in the Greater Caucasus coincides with climate change and accelerated sediment deposition around the Alps, as well as worldwide (Willett, 2010). It has been hypothesized (Molnar, 2004) that the increased sedimentation rate is caused by Plio-Pleistocene cooling of climate that could provide a more erosive environment worldwide. This hypothesis is based on the assumption of no significant orogenesis beginning at 5 Ma. The new evidence for the post-Miocene closure of the Greater Caucasus basin leading to the uplift of the Greater Caucasus and, potentially, other regions of Periarabia requires reconsideration of such an assumption. While the rapid uplift and accelerated exhumation of the Greater Caucasus is not likely to account for all of the increase of sedimentation rates throughout the world, or all of the carbon sequestration that might have led to global cooling, their contribution to sediment and carbon fluxes should be accounted for in the global and regional climate-erosion-tectonics models.

Bibliography

Allen, M. B., Kheirkhah, M., Emami, M. H. and Jones, S. J. Right-lateral shear across Iran and kinematic change in the Arabia-Eurasia collision zone. *Geophysical Journal International*, 184(2):555–574, 2011. ISSN 1365-246X. doi:10.1111/j.1365-246X.2010.04874.x.

McQuarrie, N., Stock, J. M., Verdel, C. and Wernicke, B. P. Cenozoic evolution of Neotethys and implications for the causes of plate motions. *Geophys. Res. Lett.*, 30(20):2036, 2003. doi:10.1029/2003GL017992.

Molnar, P. Late cenozoic increase in accumulation rates of terrestrial sediment: How might climate change have affected erosion rates? *Annu. Rev. Earth Planet. Sci.*, 32:67–89, 2004. ISSN 0084-6597. doi:10.1146/annurev.earth.32.091003.143456.

Philip, H., Cisternas, A., Gvishiani, A. and Gorshkov, A. The Caucasus: an actual example of the initial stages of continental collision. *Tectonophys.*, 161(1-2):1–21, 1989.

Willett, S. D. Late Neogene Erosion of the Alps: A Climate Driver? *Annu. Rev. Earth Planet. Sci.*, 38(1):411–437, 2010. doi:10.1146/annurev-earth-040809-152543.

Zonenshain, L. P. and Le Pichon, X. Deep basins of the Black Sea and Caspian Sea as remnants of Mesozoic back-arc basins. *Tectonophys.*, 123:181–211, 1986.

APPENDICES

APPENDIX A

Central Greater Caucasus thermochronometry data tables

Following are data tables and a figure containing single grain apatite (Tab. A.1) and zircon (Tab. A.2) (U-Th)/He concentrations, fission track counts (Tab. A.3) and feldspar argon release spectra (Fig. A.1), along with corresponding age estimates.

Bibliography

Dean, R. B. and Dixon, W. J. Simplified statistics for small numbers of observations. *Anal. Chem.*, 23(4):636–638, 1951. ISSN 0003-2700.

Farley, K. A., Wolf, R. A. and Silver, L. T. The effects of long alpha-stopping distances on (U-Th)/He ages. *Geochim. Cosmochim. Acta*, 60:4223–4229, 1996. ISSN 0016-7037.

Table A.1: Central Greater Caucasus single grain apatite (U-Th)/He data

Sample	Age[a] (Ma)	U (ppm)	Th (ppm)	^{4}He (nmol/g)	Mass (μg)	Ft[b]	r[c] (μm)	Sm (ppm)
T4	1.11 ± 0.04	1.44	3.69	0.02	17.05	0.64	40.0	1294.48
T4	2.38 ± 0.09	8.61	25.55	0.13	2.78	0.65	42.5	135.57
T4	1.82 ± 0.06	1.37	4.15	0.02	21.43	0.66	40.0	479.73
T4	1.44 ± 0.05	1.44	3.84	0.02	16.50	0.66	42.5	885.95
T4	1.61 ± 0.06	1.35	3.81	0.02	16.90	0.65	40.0	465.77
T3	3.74 ± 0.12	1.67	4.33	0.04	28.20	0.66	43.0	270.75
T3	1.58 ± 0.06	1.36	3.64	0.02	18.43	0.64	40.5	348.73
T3	1.20 ± 0.04	1.40	4.17	0.01	20.14	0.64	40.0	529.71
T3	0.98 ± 0.04	1.37	3.30	0.01	11.62	0.60	39.0	866.74
T2	2.79 ± 0.10	8.74	25.71	0.15	2.78	0.66	45.0	137.52
T2	0.71 ± 0.03	1.47	3.98	0.01	15.03	0.65	39.0	501.72
T2	1.32 ± 0.05	1.38	3.87	0.01	17.63	0.63	39.0	383.02
T2	1.82 ± 0.05	11.08	29.24	0.18	2.98	0.66	43.0	174.61
T2	3.63 ± 0.12	1.81	3.93	0.05	19.76	0.67	46.5	638.43
T1	2.06 ± 0.07	12.61	35.06	0.15	2.38	0.63	39.5	99.21
T1	3.28 ± 0.11	14.72	43.70	0.29	3.13	0.65	39.5	164.80
T1	2.43 ± 0.09	1.39	3.54	0.03	14.48	0.65	44.5	549.41
T1	4.37 ± 0.14	10.25	29.16	0.28	3.11	0.68	46.5	142.79
T1	1.31 ± 0.04	2.67	4.26	0.02	23.81	0.66	38.5	296.13
T1	1.83 ± 0.07	1.49	3.77	0.02	13.99	0.62	38.0	798.19
B3	14.6 ± 0.15	32.64	29.16	2.61	15.00	0.82	88.0	146.02
B3	9.50 ± 0.13	30.40	5.63	1.33	10.13	0.81	83.5	171.24
B3	13.11 ± 0.20	17.60	3.64	1.08	15.33	0.78	68.0	619.52
B3	11.38 ± 0.19	47.47	4.97	2.29	5.84	0.75	58.5	202.40
B2	3.98 ± 0.02	112.14	3.66	2.19	17.87	0.88	136.0	2008.81
B2	4.28 ± 0.03	77.45	3.46	1.58	12.82	0.84	93.5	1871.55
B2[d]	14.89 ± 0.10	91.69	3.80	6.55	13.31	0.85	105.0	1950.75
B2	4.94 ± 0.04	62.06	1.75	1.38	13.38	0.82	84.0	164.58
B2	3.03 ± 0.03	99.04	3.44	1.33	7.54	0.80	82.0	229.74
B6	8.46 ± 0.51	27.71	14.68	1.20	13.07	0.83	84.5	168.15
B6	20.00 ± 1.20	27.86	39.68	3.09	6.05	0.76	54.0	221.37
B6	13.09 ± 0.79	28.04	72.31	2.43	6.91	0.75	54.5	262.76
B6	12.65 ± 0.76	20.52	23.52	1.36	6.20	0.75	52.5	205.29
B5[d]	53.61 ± 3.22	106.70	1.78	26.74	11.20	0.85	117.5	200.93
B5	14.87 ± 0.89	63.12	2.94	3.73	2.48	0.72	45.0	108.79
B5	21.12 ± 1.27	192.63	11.62	16.59	2.33	0.74	52.0	198.66
B5	21.11 ± 1.27	67.65	1.87	5.90	3.09	0.75	53.0	168.97
B4	16.37 ± 0.98	37.36	20.13	2.77	5.24	0.74	48.0	116.43
B4	8.70 ± 0.52	27.55	16.21	1.07	2.55	0.72	46.5	90.80
B4	9.32 ± 0.56	29.68	22.46	1.31	3.21	0.73	47.5	122.61
B4	12.18 ± 0.73	23.79	22.54	1.39	4.41	0.71	44.5	131.70
B1	10.16 ± 0.61	89.16	39.93	4.11	3.45	0.75	54.0	378.47
B1	22.34 ± 1.34	87.20	39.37	8.78	3.07	0.74	52.0	370.05
B1	11.89 ± 0.71	83.06	42.99	4.89	7.58	0.81	73.0	229.81
B1	22.87 ± 1.37	92.31	33.96	9.89	6.47	0.79	62.5	286.95

[a] 1σ errors propagated from U, Th, and He measurement uncertainties.
[b] Alpha ejection correction of Farley et al. (1996).
[c] Grain radius.
[d] Tested positive as an outlier on the Q-test (Dean and Dixon, 1951) with 95% confidence when compared with other replicates from the same sample.

Table A.2: Central Greater Caucasus single grain zircon (U-Th)/He data

Sample	Age (Ma)	U (ppm)	Th (ppm)	He (nmol/g)	Mass (μg)	Ft	r (μm)
B1	188.50 ± 3.87	714.94	147.81	576.8	4.46	0.75	39.5
A1	24.06 ± 0.49	2095.89	101.64	207.01	4.13	0.75	39.8
A2	88.93 ± 1.81	673.17	68.66	240.11	2.88	0.72	34.8
T3	32.04 ± 0.72	655.24	418.65	95.07	4.9	0.73	33.8
T1	20.40 ± 0.39	679.60	448.29	64.89	4.48	0.75	39.5

Table A.3: Central Greater Caucasus apatite and zircon fission-track data

Sample	Grains (dmnls)	Dpar (μm)	Dper (μm)	N_s (tracks)	Area Analyzed (cm^2) ($\times 10^{-3}$)	$\Sigma(P\Omega) \pm 1\sigma$ (cm^2) ($\times 10^{-4}$)	$\xi_{MS} \pm 1\sigma$	^{43}Ca(ap):^{29}Si(zr) (bkg:sig) ($\times 10^{-2}$) (dmnls)	^{238}U (bkg:sig) ($\times 10^{-2}$) (dmnls)	Q	Pooled Age (Ma)	Mean length (μm)
							Apatite[a]					
A1	25	1.35	0.3	88	1.16	1.42 ± 0.0448	16.61 ± 0.42	3.67	1.23	0.82	5.16 ± 0.59	13.63 ± 1.86
A2	20	1.36	0.27	94	0.754	1.53 ± 0.0362	16.56 ± 0.42	3.37	2.80	0.15	5.09 ± 0.55	12.37 ± 1.67
B1	25	1.31	0.22	702	1.17	2.68 ± 0.0558	16.65 ± 0.42	3.49	6.06	0	21.8 ± 1.1	12.63 ± 2.07
B2	25	1.29	0.28	119	1.18	2.57 ± 0.0456	15.75 ± 0.39	4.79	31.3	0.13	3.64 ± 0.35	13.74 ± 1.64
B3	24	1.33	0.25	278	0.949	2.90 ± 0.0548	15.97 ± 0.39	2.92	0.516	0.07	7.64 ± 0.52	13.82 ± 1.73
T1	24	1.35	0.35	42	0.655	0.545 ± 0.0122	16.19 ± 0.39	6.41	19.7	0.02	6.23 ± 0.98	13.9 ± 1.7
							Zircon[b]					
A1	10			464	0.0301	0.091 ± 0.00044	9.22 ± 0.3	11.3	3.04	0	230 ± 13	
B1	20			1410	0.0890	0.207 ± 0.00072	8.81 ± 0.29	12.2	6.01	0	293 ± 12	

[a] Analyst–Paul O'Sullivan, Apatite to Zircon, Inc.
[b] Analyst–Ray Donelick, Apatite to Zircon, Inc.

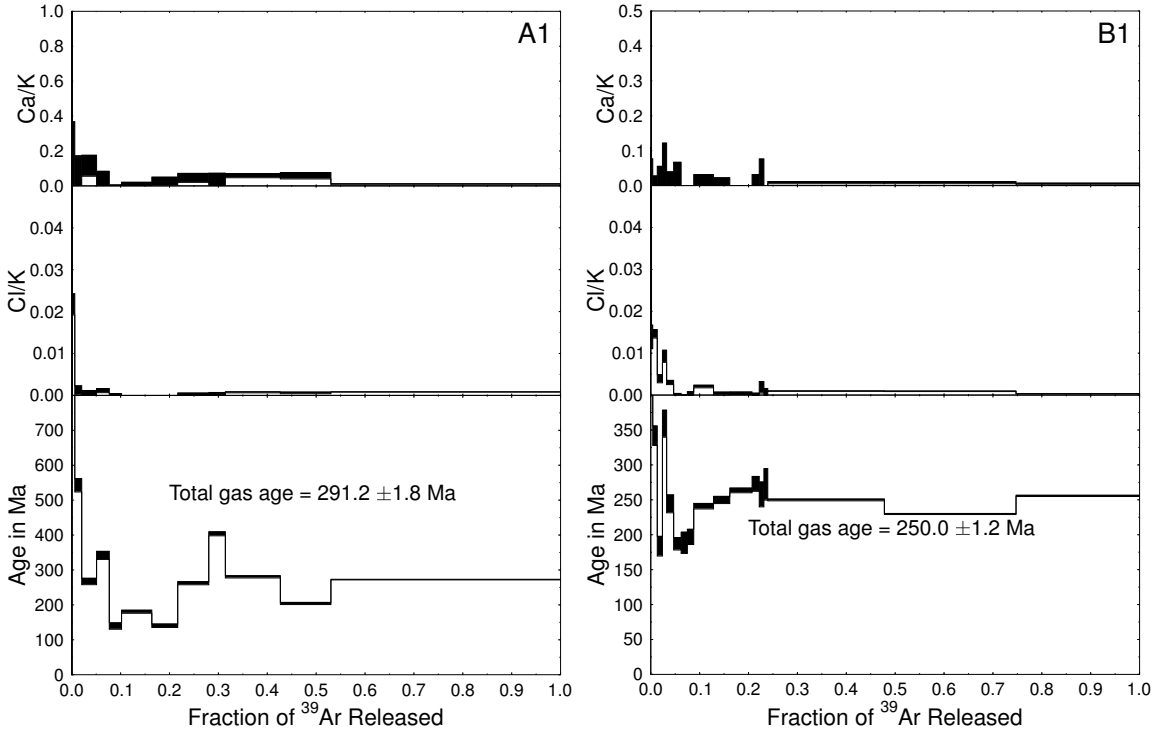

Figure A.1: Feldspar $^{40}Ar/^{39}Ar$ data

APPENDIX B

Bayesian methodology

In the Bayesian approach, the process of estimating a suite of model parameters, β, means finding $p(\beta|A)$, a joint probability density function (pdf) of β, given a set of observations, A, called a *posterior* pdf. The posterior pdf reflects the *likelihood* of the parameters (i.e., the probability of the observations, given the parameters $p(A|\beta)$), as well as any *prior* information about the parameters $p(\beta)$ that exists before observing the data A:

$$p(\beta|A) = Cp(A|\beta)p(\beta), \tag{B.1}$$

where C is a normalizing factor that scales $p(A|\beta)p(\beta)$ so that it integrates to one.

A prior can be used to include inferences based on other datasets, intuitive constraints or qualitative data. Such priors are called informative, as they add information to the posterior estimate. When no prior information exist, or if it is preferred not to include it in the analysis, non-informative (objective) priors are used. Jeffreys priors (Jeffreys, 1946) are theoretically non-informative, but are not always easy to obtain, and so it is often more practical to use uniform priors that, depending on parameterization, may be informative.

Apart from the most simple cases, the normalizing constant C is a multi-dimensional integral that is difficult to compute directly. Instead, the posterior pdf is estimated

numerically using a Markov chain Monte Carlo (MCMC) algorithm, without need to evaluate the constant directly (Hastings, 1970). The MCMC algorithm produces a collection of model parameter values by constructing a Markov chain designed to sample the posterior pdf efficiently over many iterations. This posterior sample can then be used to estimate the posterior probability density of model parameters, or more compact summary statistics such as posterior means and credible intervals (CI; the Bayesian analog of confidence intervals). While implementing an efficient MCMC algorithm is not trivial, there exist a number of general-purpose MCMC samplers that take likelihood and prior functions and return a posterior sample. In this study we use the *PyMC* package for Python (Patil et al., 2010), which provides a generic automatically tuned MCMC sampler based on the Metropolis-Hastings algorithm (Hastings, 1970).

There are a number of approaches to presenting Bayesian estimates. The most complete representation is the multidimensional posterior probability density function. It can be approximated from the MCMC-generated sample using kernel density estimation (e.g. Wand and Jones, 1995). The more compact presentation, however, commonly includes the mean of the sample (mean a posteriori estimate) together with credible intervals (CI) or standard deviation.

Expected deviance, a measure of distance between model and data, is used to compare models. Deviance is defined as

$$D(\beta) = -2 \log p(A|\beta). \tag{B.2}$$

The absolute value of deviance is not important, but differences between deviances of models based on the same datasets provide relative fit of each model. Deviance information criterion (DIC, Spiegelhalter et al., 2002) is a formal model selection tool that measures model fit to the data while penalizing for model complexity. DIC

is defined as

$$DIC = 2\mathbb{E}D(\beta) - D(\mathbb{E}\beta), \tag{B.3}$$

where $\mathbb{E}$ indicates the expected value. It should be mentioned that DIC is only valid for approximately normal posterior distributions.

An alternative approach to model selection is the formulation of nested models. For example, a no-break-in-slope model is a special case of a one-break-in-slope model (with equal erosion rates before and after the age of break). The fact that, in the Whitney example, erosion rates before and after the break do not overlap indicates that there probably is a real break. The same logic can be applied to the uniform erosion model, which is a special case of a non-uniform erosion model.

APPENDIX C

Detrital sample collection and apatite (U-Th)/He analytical procedures

A detrital sample from the Shillong Plateau was collected at 25.1889°N, 92.10174°E, 50 m a.s.l. The sample was taken from a dry, medium-grained sand bar in an active river channel.

Mineral concentrates were made from the fluvial sand using standard magnetic and density techniques. Individual mineral grains of apatite were handpicked from the concentrates, with care taken to avoid grains with inclusions visible under 200× magnification. To avoid sampling bias, grains of varying quality and morphology were analyzed.

Single grain apatite (U-Th)/He analyses were conducted at the Caltech Noble Gas Laboratory (Table C.1) following standard procedures (Farley and Stockli, 2002). Samples were outgassed using a Nd-YAG laser (House et al., 2000) and ^{4}He was measured by ^{3}He spike using a quadrupole mass spectrometer. ^{238}U, ^{235}U, ^{232}Th and ^{147}Sm were measured using isotope dilution ICP mass spectrometry (Farley and Stockli, 2002). Analytical uncertainty of apatite (U-Th)/He ages is based on instrument precision and error in the alpha ejection correction (Farley et al., 1996). The Durango fluorapatite standard ((U-Th)/He age of 31.4 Ma (McDowell et al., 2005)) was analyzed in all sample runs to check age accuracy.

Table C.1: Shillong plateau detrital apatite (U-Th)/He data. 1σ errors propagated from U, Th, and He measurement uncertainties. Alpha ejection correction of Farley et al. (1996).

Age (Ma)	U (ppm)	Th (ppm)	^{4}He (nmol/g)	Mass (g)	Ft	Radius (m)	Sm (ppm)
8.34 ± 0.38	3.22	12.37	0.22	3.90	0.75	61.62	292.94
5.60 ± 0.17	29.96	117.58	1.27	2.91	0.72	56.32	333.33
35.80 ± 1.41	0.70	3.10	0.21	19.49	0.74	60.95	8.77
6.93 ± 0.17	30.69	88.97	1.58	5.95	0.81	87.46	231.81
4.96 ± 0.15	7.83	12.27	0.22	18.41	0.75	53.01	116.32
7.87 ± 0.28	6.47	8.93	0.31	5.50	0.80	81.37	273.40
15.93 ± 0.57	2.27	6.07	0.23	16.40	0.70	51.46	23.03
9.55 ± 0.39	6.47	8.93	0.31	5.50	0.65	41.30	273.40
7.47 ± 0.23	47.87	62.88	1.89	2.10	0.74	62.50	342.97
11.95 ± 0.40	25.22	10.00	1.28	3.22	0.71	43.95	193.17
8.27 ± 0.28	18.67	4.62	0.65	4.54	0.71	43.07	342.83
4.84 ± 0.12	17.17	47.98	0.57	18.23	0.76	59.41	101.54
4.08 ± 0.10	16.43	111.46	0.74	15.19	0.77	72.00	178.46
5.03 ± 0.18	4.86	7.60	0.14	14.43	0.74	54.55	159.36
5.55 ± 0.16	10.54	74.16	0.61	15.77	0.71	49.92	130.66
5.71 ± 0.16	10.69	33.97	0.44	15.08	0.76	56.99	57.87
4.05 ± 0.11	33.61	36.98	0.66	15.81	0.71	49.03	73.31

Bibliography

Farley, K. A. and Stockli, D. F. (U-Th)/He dating of phosphates: Apatite, monazite, and xenotime. In Kohn, M., Rakovan, J. and Hughes, J., editors, *Phosphates: Geochemical, Geobiological, and Materials Importance*, volume 48 of *Reviews In Mineralogy & Geochemistry*, pages 559–577. Mineralogical Society of America, 2002. ISBN 0-939950-60-X.

Farley, K. A., Wolf, R. A. and Silver, L. T. The effects of long alpha-stopping distances on (U-Th)/He ages. *Geochim. Cosmochim. Acta*, 60:4223–4229, 1996. ISSN 0016-7037.

Hastings, W. K. Monte Carlo sampling methods using Markov chains and their applications. *Biometrika*, 57:97–109, 1970.

House, M. A., Farley, K. A. and Stockli, D. Helium chronometry of apatite and titanite using Nd-YAG laser heating. *Earth Planet. Sci. Lett.*, 183:365–368, 2000.

Jeffreys, H. An invariant form for the prior probability in estimation problems. *Proceedings of the Royal Society of London. Series A, Mathematical and Physical Sciences*, 186:453–461, 1946. ISSN 00804630.

McDowell, F. W., McIntosh, W. C. and Farley, K. A. A precise $^{40}Ar/^{39}Ar$ reference age for the Durango apatite (U-Th)/He and fission-track dating standard. *Chem. Geol.*, 214:249–263, 2005.

Patil, A., Huard, D. and Fonnesbeck, C. PyMC: Bayesian stochastic modelling in Python. *Journal of Statistical Software*, 35:1–81, 2010.

Spiegelhalter, D. J., Best, N. G., Carlin, B. P. and van der Linde, A. Bayesian measures of model complexity and fit. *J. Roy. Stat. Soc. B*, 64(4):583–639, 2002. doi:10.1111/1467-9868.00353.

Wand, M. P. and Jones, M. C. *Kernel Smoothing*. Chapman and Hall, London, 1995.